Sebastian von Gehlen

Minimal stochastic models for non-equilibrium effects and atomic-scale friction phenomena

Universität Bielefeld
Fakultät für Physik

Dissertation
zur Erlangung des Doktorgrades

Minimal stochastic models for non-equilibrium effects and atomic-scale friction phenomena

Sebastian von Gehlen

30. Oktober 2009

Gutachter
Prof. Dr. Peter Reimann
Prof. Dr. Jürgen Schnack

Gedruckt auf alterungsbeständigem Papier ∞ ISO 9706

Für Antje und Maximilian

CONTENTS

List of Figures

1 Introduction

Friction is not a material property
but a system response.

Bharat Bhushan

1.1 About this thesis

Nanotribology is the study of friction, lubrication, and wear on the nanoscale. This relatively young field of research has evolved from classical tribology essentially for two reasons: on the one hand, new technologies like micro- and nano-electro-mechanical systems (MEMS, NEMS) or the manipulation of nano-objects with an atomic force microscope (AFM) demand an atomistic theory of friction; on the other hand, the complexity of friction suggests that any substantial progress toward a *Theory of friction* can only be achieved based on a thorough understanding of its atomic-scale mechanisms. What nanotribologists hope for is to explain friction eventually in much the same way that thermodynamics is explained by statistical physics.

Although the phenomenological laws of macroscopic friction are already centuries old, a fundamental and quantitative theoretical description of friction is still missing. Furthermore, atomic-scale friction experiments produced results contrary to expectations from the classical laws: on the atomic scale, friction actually depends on the contact geometry, on rotation angles, on atomic lattices, *etc*. Since macroscopic contacts between two sliding bodies are made of single asperities down to atomic size, the need for theoretical models describing friction phenomena on the nanoscale is self-evident [1].

There are three theoretical approaches toward modeling atomic-scale friction, each of them being suitable under certain premises [2]:

- For systems of many interacting particles there are atomistic molecular dynamics (MD) simulations. They are rigorous and accurate tools, yet expensive in terms of computer time and thus limited to nanometer size systems and nanosecond time scales.

- Phenomenological rate–state models are coarse grained models that keep only a manageable number of (phenomenological) state variables to be fitted to experimental results [3]. They were first introduced by geophysicists to describe the slow time evolution of mechanical contacts (*e.g.*, earthquake models based on a complicated dynamics of aging and rejuvenation of coarse grained contacts).

- The highest reduction of complexity is achieved in minimalist models with as few degrees of freedom as possible. Wether a minimal model is still reliable must be ascertained in each individual case. As far as nonlinear phenomena of molecular friction are concerned (*e.g.*, stick–slip motion), this minimal approach has been applied successfully.

This thesis applies minimalist modeling to nanotribological systems without lubrication and wear. It approaches these systems from a different angle than nanotribological studies usually do. Normally, a minimal dynamical system is deduced to realistically represent the complex dynamics as it can be found in experiment. Since this thesis is focused on possible non-equilibrium effects that may contribute to atomic-scale friction, the minimal systems under study are purposefully designed in such a way that special non-equilibrium effects are not inhibited *a priori*. In other words, models are chosen including a minimum of complexity necessary to reproduce a system behavior beyond the regime of linear response. As a consequence, the connection to reality, *i.e.*, the "mapping" of experimentally accessible parameters onto the system variables of the minimal model, can only be made *a posteriori*. This is a part of the interpretation of the models and their results.

The dynamical systems considered in this thesis comprise relatively small numbers of coupled particles, especially pairs thereof, the so-called *dimers*. Their study is useful with regard to various friction phenomena, *e.g.*, tribological effects arising from ad-atoms in atomic contacts or adsorbed dimers on surfaces. They also serve, in different contexts, as model systems for molecular motors, polymers, ferrofluids, and colloidal systems, to name but a few. There are two reason for this versatile applicability of dimers to so many different physical systems: on the one hand, they are not very complex (two-body problems are analytically tractable, whereas three-body problems cannot be solved in general), on the other hand, a dimer is the simplest system that offers more complexity than a single particle.

This thesis is organized as follows:

- **Chapter 1** presents, within the following sections, some historical notes on friction from a scientific point of view, its exploration, and the development of nanotribology. Important issues of atomic-scale friction experiments are introduced such as the stick–slip motion encountered

in both the micro- as well as the macro-world and the meaning of structural lubricity or superlubricity. It ends with a literature survey on books, reviews, and articles from the field of nanotribology in general and non-equilibrium atomic-scale friction phenomena in particular. A logarithmic force–velocity relation is derived in brief.

- **Chapter 2** gives a shorhand explanation of certain theoretical aspects of Brownian motion. The first section presents important results concerning the dynamics of Brownian particles in tilted periodic potentials. The exact analytical derivation of the velocity and the diffusion coefficient of such particles is redrawn in a condensed form. In the second section, the ratchet effect is highlighted. A minimalist ratchet model and the prototypal on–off ratchet are discussed in order to describe the mechanism generating unidirectional motion without any external bias. An important consequence of this non-equilibrium effect is to facilitate the design of the so-called Brownian motors.

- **Chapter 3** examines the Brownian motion of a one-dimensional chain of coupled particles in a tilted periodic potential. Special attention is payed to the effects caused by variation of the coupling strength and the ratio of the chain and surface lattice constants. Drift and diffusion of the chain are studied analytically and numerically and are shown to exhibit a complex multipeaked structure as functions of the equilibrium interparticle separation. This system can be regarded as a minimalist model of multi-asperity contacts.

- **Chapter 4** treats the ratchet effect of a dimer that finds itself in a symmetric potential. The symmetry of the model is broken through an internal degree of freedom. It is achieved by different coupling strength of the dimer components to the flashing surface potential. An accurate analytical approximation for the dimer's velocity and diffusion coefficient is obtained. The velocity is maximized by adding an optimal amount of noise and by tuning the driving frequency to an optimal value. Furthermore, there exists an optimal coupling strength at which the velocity is the largest.

- **Chapter 5** is concerned with a system nearly identical to chapter 4: a dimer with broken friction symmetry in a symmetric potential. Instead of the coupling to the surface potential, the coupling to the heat bath via the viscous friction coefficients is different for both dimer components, thus breaking the dynamical symmetry of the system. A weak and a strong coupling approximation of the dimer's velocity and diffusion coefficient are derived and compared to extensive numerical simulations of the Langevin equations.

- **Chapter 6** finally concludes the thesis with a summary of the main results and depicting their relevance to atomic-scale friction phenomena. Any attempt to control friction via some system parameters is pursued most efficiently if one can make use of non-linear and/or non-equilibrium effects since these effects can exert the most powerful influence on any dynamical system.

On first sight, the key ingredients of this thesis (*i.e.*, nanotribology, Brownian motion in tilted periodic potentials, and the ratchet effect) are seemingly unrelated. But a simple change of the frame of reference can establish a quasi-direct connection between these different fields of research. On the one hand, if the AFM tip is pulled across a surface, the pulling velocity is the control parameter and the friction force is the observed variable. On the other hand, if a Brownian particle in a tilted periodic potential is concerned, the tilt (force) is the control parameter and the resulting velocity is the observed variable. If we consider a sufficiently weak cantilever both pictures, pulling and tilting, are essentially the same, as pointed out in section 2.1.1. To demonstrate this connection, let us take a closer look onto the experimental situation.

In a typical atomic scale friction experiment, the tip of an atomic force microscope (AFM, *cf.* section 1.3.1) scans along an atomically flat surface, *e.g.*, Cu(111) or Si(111). The tip–surface interaction can be projected onto a one-dimensional potential corresponding to the one-dimensional path of the tip across the surface. The potential can most easily be modeled by a symmetric periodic function, in the simplest case a cosine of the contact coordinate.

The situation becomes quite different if the AFM tip is not in direct contact with the surface but instead is placed on top of an island floating freely above the surface. Such islands (*e.g.*, antimony or gold nanodroplets, *cf.* Fig. 1.12) can form a special interface between tip and surface, where the tip is connected to the island and can move it across the surface. Depending on the exact structure of this interface, it can give rise to dynamical effects that cannot be modeled as usual by a single contact coordinate. For example, if the island consists of two different kinds of atoms, say elements A and B, forming an alternating crystal lattice (...A–B–A–B...), the corresponding one-dimensional minimal contact model naturally is a dimer.

Experimentally, the main control parameter still is the relative velocity between the cantilever and the AFM stage carrying the sample. But for the sliding (or stick–slip) dynamics of the interface, *i.e.*, the nanotribological subsystem to be modeled, the determining parameter is the instantaneous force (or tilt). It is exerted by the cantilever that pushes or pulls the island across the surface. Here is the place where non-equilibrium effects come into play via thermal activation of escape events or purposeful manipulation of other system parameters. Both can give rise to non-linear effects with high impact on the dynamical properties, thereby permitting to control atomic-scale fric-

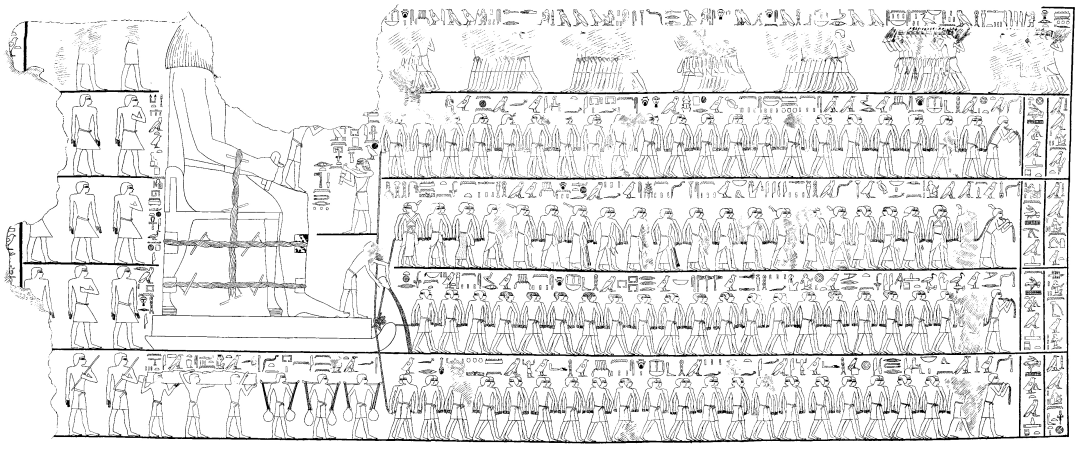

Figure 1.1: An Egyptian colossus is transported on a sledge. A lubricant is poured onto the ground in front of the sledge. Fragment of a painting from the tomb of Tehuti-Hetep, El-Bersheh (∼1880 B.C.), taken from [5].

tion. A prominent example is the ratchet effect that enables unidirectional transport in otherwise symmetric systems.

These effects are of fundamental importance: not only do we live in a non-linear universe but also at non-equilibrium—otherwise, our world would suffer the "heat death", a final state of maximal entropy first recognized by William Thomson (Lord Kelvin) in the 1850s. The non-linearity is responsible for the richness and complexity of our world, and deviations from equilibrium are the prerequisite of all physical processes, motion, and life, powered by the persisting fluctuation and dissipation of energy. Since friction is an almost omnipresent mediator of dissipation, friction research remains an issue of both fundamental and practical importance.

1.2 Macroscopic friction

1.2.1 Historical notes

Friction is one of the oldest technological challenges that was tackled by human ingenuity, dating back to prehistoric times. It is also a "hot spot" of current scientific research. Novel experimental techniques offer ample opportunity for physicists and engineers to gain insight into its basic principles, solving old riddles and, at the same time, creating new ones. The reason for this longevity is that friction, at all times, was a vital issue in many respects.

For the Neanderthals, the tedious procedure of making fire by rubbing wood on wood was of very elemental importance for the preparation of food or the hibernation in northern latitudes. Ancient civilizations like Meso-

potamia and Egypt developed methods to reduce friction and thus were able to build impressive monuments for their religious purposes, see Fig. 1.1. In modern times, friction, mostly in the form of wear, is consuming a great amount of the economic performance. An often cited estimate says that the economic losses due to ignoring friction amount to approximately 6% of the gross national product of the USA [6].

The first systematic exploration of friction is ascribed to Leonardo da Vinci (1452–1519). However, his sketches of various experiments concerning static and sliding friction and different bearings from the *Codex Atlanticus* and the *Codex Arundel* remained unpublished for many years. The first empirical laws of friction were rediscovered by Guillaume Amontons (1663–1705) and Charles Augustin de Coulomb (1736–1806) and named in their honor [7]. Substantial contributions were added by Leonhard Euler (1707–1783) and Osborne Reynolds (1842–1912). The former was the first to discern between static and kinetic friction and has introduced the dimensionless friction coefficient, the latter worked out the role of friction in the field of fluid mechanics.

The empirical laws state the following relations concerning the friction force between two solid bodies:

1. The friction force is independent of the apparent area of contact.
2. The friction force is proportional to the normal force (the load) acting on the area of contact.

Both are known as Amontons' laws of static friction. Coulomb's law of sliding friction says:

3. The friction force is independent of the sliding velocity.

It must be said that these empirical "laws" can only be understood as rough approximations to reality because their validity is restricted to the normal cases of macroscopic contacts, not too clean or lubricated or too smooth or too heavily grafted surfaces, and not exceedingly low or high sliding velocity. Nevertheless, the plain but extensively applicable formula resulting thereof,

$$F = \mu L\,, \tag{1.1}$$

connects the friction force F to the normal load L via a system constant μ, the friction coefficient, and has been successfully in use for centuries.

Surprisingly, the friction coefficients for *dry* contact areas, *i.e.*, without lubrication, are all of order unity. This universal behavior gave rise to a simple geometrical explanation as depicted in Fig. 1.2. If there are no other forces like adhesion acting between both surfaces, the resulting force necessary to move the upper body relative to its lower counterpart is given by

$$F_s = L \tan\alpha\,, \tag{1.2}$$

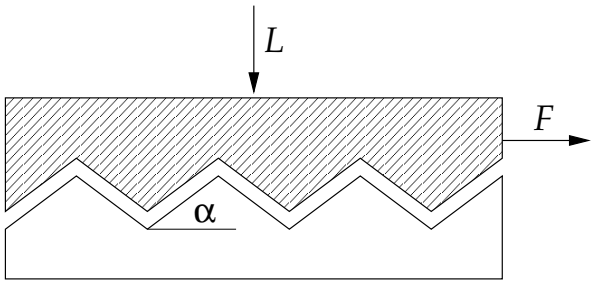

Figure 1.2: Schematic of two surfaces with interlocking asperities. The upper body experiences a normal load L and a pulling force F, while the lower body is fixed. The slope α of the asperities determines the static friction.

where F_s denotes the static friction, α the inclination angle of the surface asperities, and L the normal load, as before. This purely geometrical reasoning dates back to Coulomb and was, for a very long time, the standard explanation for dry friction. But it is an oversimplification: the natural roughness of surfaces is, in most cases, very irregular so that an inclination angle cannot be defined at all. In fact, naturally rough surfaces could tend toward reduced friction because of incommensurability, see the following section. The compliance of real systems to Amontons' laws might rather be due to mobile atoms in the interface that mediate interlocking and commensurability so that a universal coefficient μ can be recovered [8].

More detailed analysis of friction phenomena was acquired not until new experimental probing techniques became available, *e.g.*, the scanning electron microscope, the use of radioactive tracers, mechanical profilometers, the surface force apparatus, *etc*. In 1950, the book of Frank Philip Bowden (1903–1968) and David Tabor (1913–2005), *The Friction and Lubrication of Solids* [9], presented extensive experimental studies and soon became a standard work in the field of tribology. They successfully explained macroscopic friction, not by surface roughness, but with a new concept of adhesive bonding, *i.e.*, the formation and destruction of interfacial contacts.

For realistic interfaces, the shearing and plowing of interfacial asperities can be viewed as the microscopic origin of Coulomb's law of friction. A decisive distinction must be made between the *apparent* and the *actual* area of contact (*cf.* Fig. 1.3). Whereas the former is a purely geometrical property of the sliding body, the latter is indeed load-sensitive. By increasing the normal load, the surfaces are more strongly pressed against one another and new contacts can form, thereby increasing the actual area of contact. Depending on the duration of contact, this also increases the adhesion because the newly formed contacts tend to minimize their binding energy.

Furthermore, the resistance against lateral motion that comes from shearing stress or plastic deformation of all the interlocking asperities naturally is

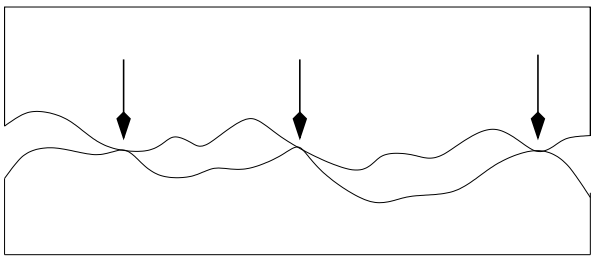

Figure 1.3: Every macroscopically smooth surface has a microscopical roughness consisting of undulating hills and wells. The actual area of contact therefore is formed by single asperities, indicated by arrows, where the largest protrusions are in direct contact. It is considerably smaller than the apparent area of contact, which would consist of the whole surface.

proportional to the actual area of contact. When the upper layer is pulled by a force F, all the single asperity forces add up to the overall macroscopic friction force. In 1966, Greenwood and Williamson extended this Bowden–Tabor theory to explain the mechanical properties of *elastic* contacts between nominally flat surfaces [10]. A serious shortcoming of the Bowden–Tabor theory is that it can explain friction only qualitatively, but still lacks a quantitative theoretical description of the observed macroscopic friction coefficients.

1.2.2 Macroscopic stick–slip motion

A classical friction experiment consists of a cuboid block of a solid material under study with clean and flat surfaces. It is pulled across a table by a rope or wire, see Fig. 1.4. The pulling rope is connected to the block by an elastic spring. If the free end of the rope is pulled forward at constant velocity, the force exerted on the block increases in direct proportion to the elongation of the spring, according to Hooke's law.

The response of the block to the increasing pulling force reveals three different regimes of motion:

1. In the beginning, the force increases until it reaches the value of the static friction between block and table. Immediately thereafter, the block starts moving and the spring relaxes until the elastic force equals to the sliding friction of the block. Continued pulling keeps this force constant and results in a steady sliding motion, see Fig. 1.5 (a).

2. For a low pulling velocity or a weak spring the motion sets in above the threshold of static friction. But, due to inertia, the body moves so far that the restoring force of the spring falls below the sliding friction level. Therefore, the quick jump at each onset of motion always ends abruptly after a characteristic length has been travelled. This kind of

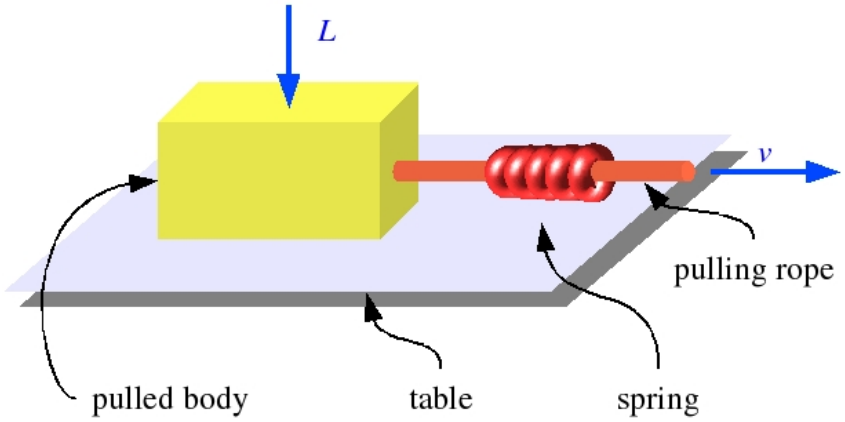

Figure 1.4: A classical friction experiment: A body with normal load L is pulled across a table at constant velocity v. The friction force is directly proportional to the elongation of the elastic spring connecting the pulling rope with the body.

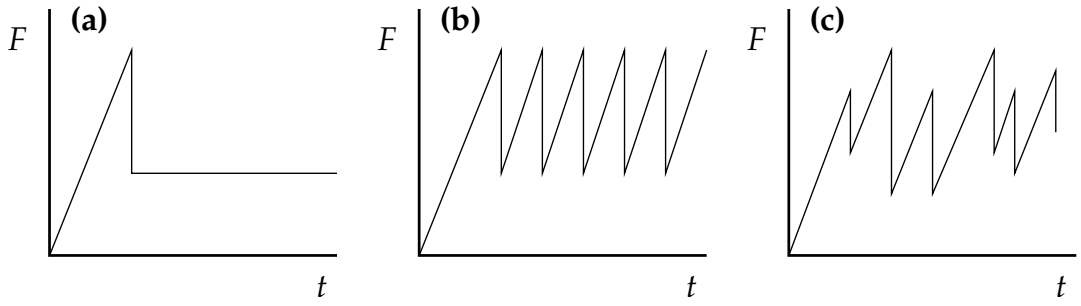

Figure 1.5: Three different regimes of sliding motion as observed in the experiment from Fig. 1.4: (a) steady sliding, (b) periodic stick–slip motion, (c) chaotic motion. Horizontal axis: time t; vertical axis: pulling force F.

intermittent sliding is known as stick–slip motion and is frequently encountered in squeaky door hinges or pieces of chalk being drawn across black boards, *cf.* Fig. 1.5 (b).

3. If the interface is less regularly structured so that nonlinear terms within the equations of motion prevail, the stick–slip motion may turn out random. The force values at which the intermittent jumps start and end will be statistically distributed around some average values of static and sliding friction, see Fig. 1.5 (c).

It is important to distinguish between the *macroscopic* stick–slip phenomenon as described above and *atomic-scale* stick–slip motion which we will present in the following section. Although both phenomena appear to be close relatives on different length scales, they are fundamentally dissimilar.

1.3 Nanotribology

1.3.1 New experimental techniques

The advent of the various local probe methods in the 1980s gave a real boost to research activities, especially with regard to surface science. A concise overview of these new scanning microscopy techniques is given in Ref. [11]. The first representative of these new techniques was the scanning tunneling microscope (STM) built by Gerd Karl Binnig (1947) and Heinrich Rohrer (1933). In 1981, it operated successfully for the first time and delivered topographical images of monatomic steps. Its resolution was continuously refined to atomic length scales of a few ångström so that it became possible to "see" the single atoms of a crystalline surface. For this invention, Binnig and Rohrer have been awarded the Nobel prize in 1986 [12].

In contrast to optical and electronic instruments (*e.g.*, the scanning electron microscope developed in the 1930s), the STM is primarily a *mechanical* tool that, like a "nanofinger", mechanically probes the topography of a sample. It does so by piezo actuators that keep the tunneling current flowing through the gap between tip apex and sample at a constant value. The next idea was to measure the vertical profile of a surface in a more direct fashion, *viz.*, by directly utilizing mechanical properties. This became possible with the atomic force microscope (AFM), developed by Binnig *et al.* in 1985 [13]. While the first AFM was combined with an STM, where the STM measured the vertical displacement of the AFM tip and cantilever, shortly after that the displacement was measured directly via the deflection of a laser beam from the cantilever, see Fig. 1.6.

In direct contact mode, the tip is pressed against the surface with a constant force that is related to a specific elastic bending of tip and cantilever. The

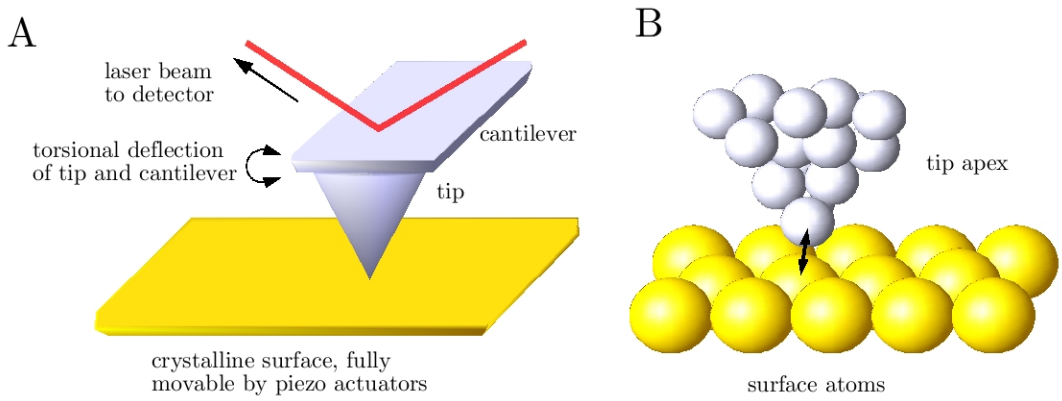

Figure 1.6: Schematic of the probe–sample contact in an FFM. Part A: A cantilever tip in contact with a crystalline surface; the surface is movable in x, y and z direction by piezo actuators. Part B: A closed atomic contact exists between an atom of the tip apex and a surface atom (black arrow); moving the substrate leads to a bending of tip and cantilever that can be detected by a deflected laser beam.

repulsive force between tip and surface is due to the Pauli exclusion of the electron shells involved. In a way, the constant normal force is reminiscent of the load of a sliding body, and drawing the tip across a surface can be seen as a sliding motion with extremely small area of contact, where usually but a few atoms participate [4]. This analogy was fully exploited in the friction force microscope (FFM) that was developed by Mate *et al.* in 1987 [14].

The difference between AFM and FFM is the pulling direction of the tip. While the AFM tip is pulled parallel to the cantilever beam, the FFM tip is pulled sideways, perpendicular to the cantilever. The AFM signal is deduced from the *longitudinal* deflection of the cantilever whereas the FFM in addition detects the *lateral* one. It is caused by the torsional force acting on the tip–cantilever complex whose elastic response is proportional to the coplanar force component of the tip–surface interaction. Because of its sensitivity to lateral forces, *i.e.*, those forces inhibiting motion classified as friction, the FFM can actually measure atomic-scale friction. The first experiments by Mate and co-workers were performed with a tungsten tip on a crystalline graphite surface and displayed periodic patterns with atomic-scale resolution: the stick–slip motion at the nanoscale.

In 1988, Krim *et al.* used a quartz-crystal microbalance (QCM) to measure the momentum of an adsorbate layer and deduced a relation for the film-substrate interfacial viscosity based upon measurements of the acoustic impedance [15]. As a consequence of the high-frequency vibrations, extremely weak inertial forces act on the adsorbate layer. These forces could never move the film by themselves, but their effect is to tilt the surface potential just enough to allow thermally activated transport [6]. Actually, the

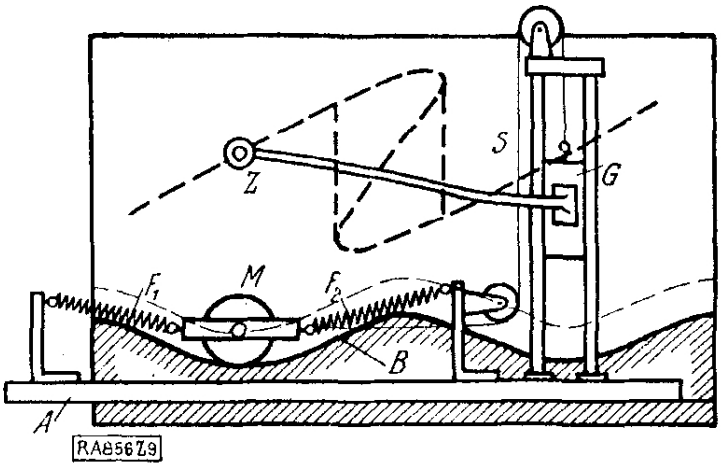

Figure 1.7: Prandtl's mechanical device showing hysteresis of sliding motion in a corrugated potential, taken from [18].

term *nanotribology* first appeared in a 1991 paper by Krim *et al.* on atomic-scale friction of a Kr monolayer [16].

The surface force apparatus (SFA) was devised by Tabor, Winterton, and Israelachvili in the 1970s [17]. It came fairly close to the resolution of the local probe techniques, being able to resolve distances of 0.1nm (measured via laser interferometry) and forces of 10nN (measured by the torsional deformation of a spring). The strength of the SFA lies in its wide range of operating distances, from tenths to over a hundred nanometers. Especially at larger distance, the SFA excels in resolving the surface-to-surface force more precisely than any other method. In combination with measuring shear, the SFA became an important tool for specifying dry and wet friction between two atomically flat surfaces in an ideal contact.

1.3.2 Atomic-scale stick–slip motion

The first theoretical studies concerning atomic-scale dry friction date back to the late 1920s. Ludwig Prandtl (1875–1953) investigated the motion of a mass that experiences a one-dimensional corrugated potential and is externally pulled with constant velocity [18]. The external pulling is coupled to the mass by an elastic spring. This simple model already reveals a theoretical prerequisite for the stick–slip motion observed in an FFM experiment.

The reason is a dynamical hysteresis as obtained from Prandtl's *Gedanken-experiment* shown in Fig. 1.7 that gives rise to a non-adiabatic loss of energy. In case of low pulling velocities and subcritical elasticity, the position of the mass undergoes a transition from stable to unstable equilibrium. The following relaxation into the new stable position excites vibrational modes of the

spring so that large parts of the stored elastic energy are dissipated as heat. In an actual atomic contact, these are the phonons created in the surface, the tip, and the cantilever by the elastic energy released in each slip event.

George Arthur Tomlinson (1885–1944) independently proposed a molecular theory of friction based on a hypothetical mechanism of dissipation induced by intramolecular forces of a Lennard–Jones type [19]. He showed how the closure and succeeding rupture of a molecular bond between a surface (atoms elastically coupled) and a passing atom of a sliding body can set a surface atom into an unstable equilibrium position. Subsequent relaxation into stable equilibrium leads to irreversible dissipation of energy previously supplied by the atom passing by. All molecular contacts between surface and sliding body thus contribute to the total amount of friction.

The so-called Prandtl–Tomlinson model is the simplest way to represent a single atomic contact in a minimal model:

1. The essentially one-dimensional movement of the FFM tip can be comprised within a one-dimensional model because the vertical tip–surface interaction is held at a constant level by appropriate tracking of the sample stage. Of course, this simplification makes quantitative predictions impossible for higher-dimensional systems but can be justified with regard to the qualitative explanations it facilitates.

2. The simplest case of the tip–surface interaction is a periodic function with a spatial period equal to the periodicity of the crystalline surface. Generally it suffices to take into account only the lowest Fourier mode, yielding a potential function

$$U(x) = \frac{\Delta U}{2}\left(1 - \cos\frac{2\pi x}{L}\right), \tag{1.3}$$

   where ΔU is the corrugation depth and L the lattice spacing. The variable x parameterizes the one-dimensional path of the tip with respect to the surface.

3. The lateral deflection of cantilever and tip and the resulting restoring force can be modeled as elastic deformations obeying Hooke's law,

$$V(x,t) = \frac{\kappa}{2}(x - vt)^2. \tag{1.4}$$

   Here, κ is defined as the serial sum of surface, tip, and cantilever elasticities, $\kappa^{-1} := \kappa_{\text{surf}}^{-1} + \kappa_{\text{tip}}^{-1} + \kappa_{\text{cant}}^{-1}$, according to [20]. The external control parameter v is the pulling velocity, and vt the (lateral) position of the cantilever regarding the one-dimensional path $x(t)$.

4. Dissipation enters the model by introducing a heat bath of absolute temperature T. A stochastic force term $\xi(t)$ mimics the thermal fluctuations which naturally arise from the surrounding atoms. These fluctuations are related to dissipation of energy from the moving tip via the *fluctuation–dissipation theorem* of the second kind giving rise to a viscosity η and a damping term $-\eta\dot{x}$. The random force is conveniently realized as a white noise with zero mean and delta correlation,

$$\langle \xi(t) \rangle = 0\,, \quad \langle \xi(t)\,\xi(s) \rangle = 2\eta k_\mathrm{B} T\,\delta\,(t-s)\,, \tag{1.5}$$

   where k_B is the Boltzmann constant.

5. According to Newton's second law, the tip–cantilever complex owns an effective mass m that connects the sum of all forces F_i acting on it to the resulting acceleration,

$$m\ddot{x} = \sum_i F_i\,. \tag{1.6}$$

Taking all parts together, we obtain a dynamical model of a single atomic contact whose formal description is given by a Langevin equation,

$$m\ddot{x}(t) = -\frac{\partial}{\partial x} U\big(x(t)\big) - \frac{\partial}{\partial x} V\big(x(t),t\big) - \eta\dot{x}(t) + \xi(t)\,. \tag{1.7}$$

It is important to notice that this kind of stochastic partial differential equation is only valid on time scales well above the mean time of ballistic motion between two collisions of the mass m with any atom within its surroundings.

An equivalent formulation is given by a Fokker–Planck equation (FPE), alternatively called Kramers equation,

$$\frac{\partial}{\partial t} P\,(x,v,t) = \left[\frac{\partial}{\partial v}\left(\frac{U'(x) + V'(x,t) + \eta v}{m} + \frac{\eta k_\mathrm{B} T}{m^2}\,\frac{\partial}{\partial v}\right) - v\frac{\partial}{\partial x}\right] P\,(x,v,t)\,, \tag{1.8}$$

where $P\,(x,v,t)$ is the probability density to find a particle at time t at position x with velocity v. The distribution P therefore no longer describes a single particle trajectory but an ensemble of such trajectories. The advantage of the FPE is that it offers an analytical approach to statistical evaluation of the system dynamics.

The resulting friction force F_fric, *i.e.*, the mean force necessary to pull the cantilever with constant velocity, is given by the time average

$$F_\mathrm{fric} = -\lim_{\tau\to\infty}\frac{1}{\tau}\int_0^\tau dt\,\frac{\partial}{\partial x}\,V\big(x(t),t\big) = \lim_{\tau\to\infty}\frac{\kappa}{\tau}\int_0^\tau dt\,[vt - x(t)] \tag{1.9}$$

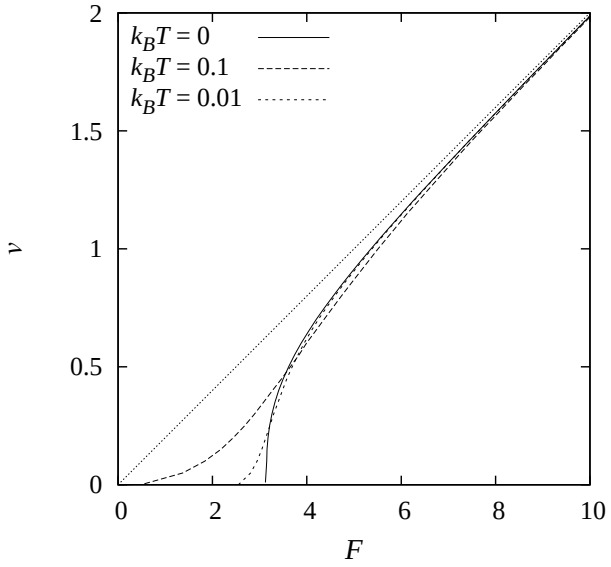

Figure 1.8: Force–velocity relation obtained from numerical simulation of Eq. (1.7), where $F = F_{\text{fric}}$, according to Eq. (1.9). Solid line: $k_BT = 0$; long dashed line: $k_BT = 0.1$; short dashed line: $k_BT = 0.01$; dotted line: $v = F/\eta$. Other parameter values: $m = L = \Delta U = 1$, $\eta = 5$, $\kappa = 0.1$. For $v \to 0$ at $k_BT = 0$, the force is close to the critical tilt at $F_c = \pi$.

of the elastic force, in analogy to the elongation of the spring from the classical friction experiment in Fig. 1.4. The force–velocity diagram of Eq. (1.7) for different values of the temperature is shown in Fig. 1.8. The role of thermally activated escape becomes clear in the $v \to 0$ limit at different temperatures: At $k_BT = 0$, the force takes on a nearly constant positive value at low velocities. With increasing temperature, the $v \to 0$-limit ensues $F \to 0$ with gradually decreasing steepness.

In the Prandtl–Tomlinson model, one observes either the stick–slip motion as explained in Fig. 1.9 or steady sliding motion due to inertia at higher velocities, see [21]. In the case of atomic-scale stick–slip motion, the force as a function of time exhibits the familiar sawtooth pattern of a linearly increasing force that abruptly drops back to a lower value whenever a slip to the next potential minimum occurs, see Fig. 1.9 (c). With a static tilt instead of an increasing force, this model for Brownian motion in tilted periodic potentials has been rigorously treated and results can be found summed up in [22].

Interestingly, at $T = 0$ and for weak κ,

$$\kappa < U''(0) = \frac{2\pi^2 \Delta U}{L^2}, \tag{1.10}$$

the Prandtl–Tomlinson model features two distinct force levels for static and

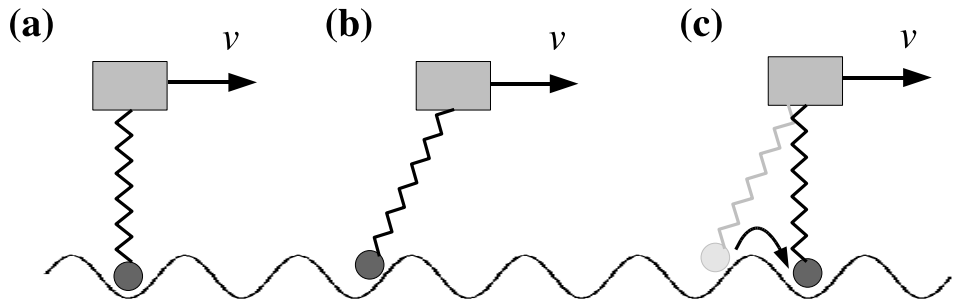

Figure 1.9: The Prandtl–Tomlinson model of a mass point in a one-dimensional corrugated potential. The mass is connected to a carrier with an elastic spring, and the carrier moves with constant velocity v. (a) Mass and carrier are aligned at the potential minimum. (b) The carrier moves to the right, but the mass cannot yet surmount the potential barrier (stick-phase). (c) When the restoring force of the spring exceeds the critical tilt of the potential, the mass instantaneously jumps to the next minimum (slip-phase). The elastic energy is largely dissipated as heat.

kinetic friction in the underdamped regime [23], where

$$\tilde{\eta} < \eta_c := \frac{\pi^2}{2L}\sqrt{\frac{\Delta U}{2m}}\,. \tag{1.11}$$

We start with a mass m at rest. If the pulling force exceeds the critical tilt of the surface potential $U(x)$,

$$F > F_c := \frac{\pi \Delta U}{L}\,, \tag{1.12}$$

the system will make a transition from the locked state to the running state. The critical tilt F_c thus is a synonym for static friction. If the pulling force is reduced, the system will stay in the running regime due to inertia until

$$F < F_k := \frac{2\eta}{\pi}\sqrt{2m\Delta U}\,, \tag{1.13}$$

when the backward transition to the locked solution takes place. This threshold force F_k corresponds to the kinetic friction. Therefore, stick–slip motion can only occur whenever the inequality $F_k < F_c$ holds.

A direct application of these findings to macroscopic systems is not possible without taking into account the contact stiffness [24] and the contact geometry [25]. For a single contact, the interplay of inertia and elasticity produces a non-trivial system behavior including locked, running, and intermittent states. For many such contacts, the whole situation increasingly depends on the exact geometry.

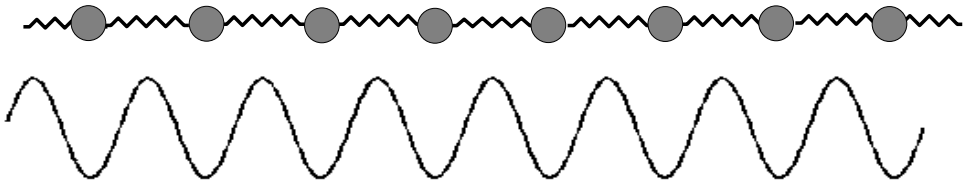

Figure 1.10: The Frenkel–Kontorova model of a harmonically coupled (infinite) chain of masses experiencing a one-dimensional sinusoidal potential.

1.3.3 Superlubricity

In the late 1930s, the Russian physicists Yakov Ilitch Frenkel (1894–1952) and Tatyana Abramovna Kontorova (1911–1976) achieved an important theoretical result in the field of plastic deformations and twinning of solids [26]. The Frenkel–Kontorova model consists of an infinite linear chain of harmonically coupled masses finding themselves in a one-dimensional sinusoidal potential, see Fig. 1.10. Under the influence of an external pulling force F being applied to the whole chain, the corresponding system of Langevin equations reads

$$m\ddot{x}_i(t) = -\frac{\partial}{\partial x_i} U\left(\{x_n(t)\}\right) - \frac{\partial}{\partial x_i} V\left(\{x_n(t)\}\right) - \eta\dot{x}_i + F + \xi_i(t)\,, \tag{1.14}$$

where the indices i and n denote the i-th and n-th particle, respectively. The function

$$U\left(\{x_n\}\right) = \sum_n \frac{\Delta U}{2}\left(1 - \cos\frac{2\pi x_n}{L}\right) \tag{1.15}$$

is the periodic surface potential with corrugation depth ΔU and corrugation length L, and

$$V\left(\{x_n\}\right) = \sum_n \frac{\kappa}{2}\left(x_{n+1} - x_n - a\right)^2 \tag{1.16}$$

is the pair interaction of the chain with equilibrium interparticle distance a. The noise terms are assumed to be Gaussian, thus obeying

$$\langle \xi_i(t) \rangle = 0\,, \quad \langle \xi_i(t)\,\xi_j(s) \rangle = 2\eta k_\mathrm{B} T\,\delta_{ij}\,\delta\left(t - s\right). \tag{1.17}$$

Because of its simplicity, this model was successfully applied to various problems besides those it was originally designed for, *e.g.*, adsorbed monolayers of atoms or molecules in surface physics, glassy systems, charge density waves or coupled Josephson junctions, to name but a few.

The ratio of the number of masses in the chain to the number of surface potential minima on a given length implies a substantial property of this model. There are commensurate *vs.* incommensurate lattices, the first meaning that a/L is a rational number, the latter that it is an irrational number. In the

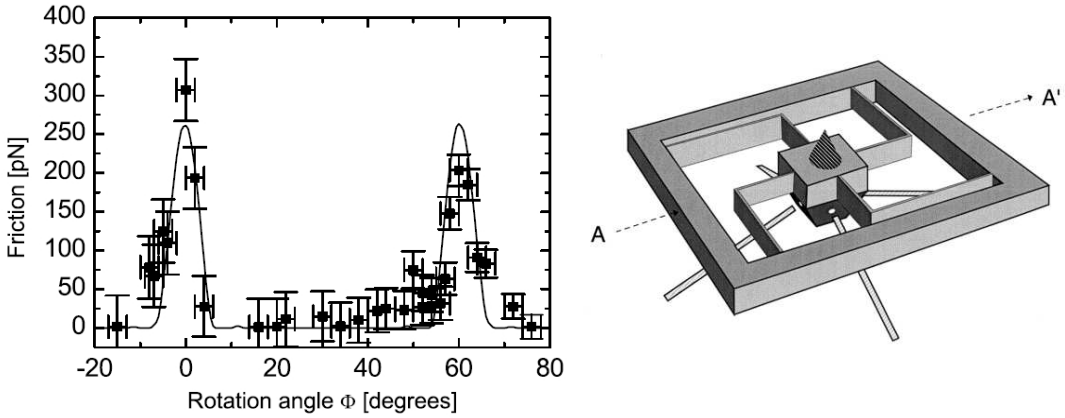

Figure 1.11: Left: Average friction force versus rotation angle of the graphite sample around an axis normal to the sample surface, taken from [31]. Two narrow peaks of high friction were observed at 0 and 61, respectively. Between these peaks a wide angular range with ultralow friction close to the detection limit of the instrument was found. Right: Schematic of the "Tribolever", taken from [32]: Lateral or frictional forces acting on the scanning tip (tungsten) are measured via the displacement of the central pyramid (silicon). Motion is detected by four laser interferometers reflecting from the pyramid facets on the rear side.

incommensurate case, a transition takes place at $\kappa = \kappa_{\text{Aubry}}$ [27], where, for larger values of κ, any non-vanishing external force F leads to steady motion, meaning that the static frictional force is zero. Of course, this only holds for *infinite* chains since *finite* Frenkel–Kontorova chains are always pinned [23]. For such a "frictionless" state the term *superlubricity* or *structural lubricity* was coined. Please note that *super*lubricity should not be confused with quantum effects like superconductivity or superfluidity where the relevant system parameter (*e.g.*, electric resistance, viscosity) vanishes completely.

Zero friction has first been proposed in the late 1980s by McClelland [28] and later, in combination with multi-dimensional Frenkel–Kontorova models of sliding surfaces, by Hirano and Shinjo [29,30]. Experimental realization waited until 2004 when Dienwiebel *et al.* measured a distinct dependence on the angle at which a graphite flake was pulled across a highly oriented pyrolytic graphite (HOPG) plate [31]. They used a novel FFM with a special friction force sensor, the so-called Tribolever [32], see Fig. 1.11, that allows measurement of forces acting on the tip in three directions, down to 15 pN. The friction force displayed peaks every 60° of the rotation angle coplanar to the surface, where only the distinct directions of commensurate (hexagonal) lattices showed noticeable friction. The incommensurate directions, which form wide angular ranges in between, showed ultra-low friction.

So far, all friction measurements that hint toward superlubricity were performed in ultra high vacuum (UHV) since exposing the samples to ambient

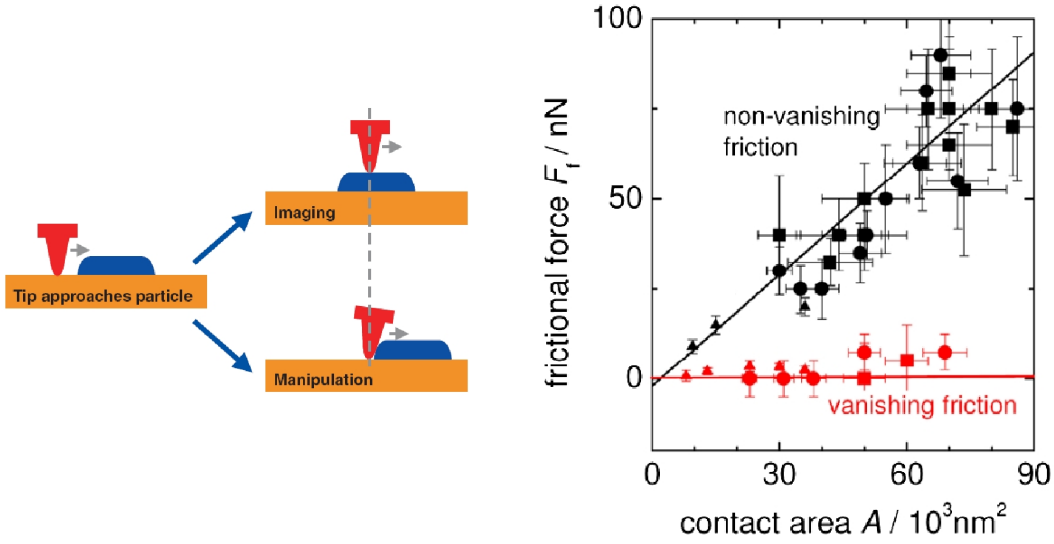

Figure 1.12: Scheme of nanoparticle manipulation experiment and data obtained under UHV conditions, uncovering two distinct frictional regimes for particle or sample contact areas up to 90 000 nm^2, taken from [33]. Regime 1 (black symbols) comprises particles with substantial friction whereas particles that exhibit virtually no measurable friction (red symbols) are assigned to regime 2.

conditions immediately produces a contamination with "dirt" particles (*e. g.*, water or hydrocarbon molecules) or oxidation of the freshly cleaved surfaces. These contaminations effectively destroy the incommensurability necessary for structural lubricity by a hypothetical interlocking mechanism [8]. Nevertheless, Dietzel *et al.* performed sliding friction measurements in air and UHV with antimony nanoparticles on HOPG that has been cleaved in UHV, and they encountered an astonishing frictional duality [33]. Some nanoparticles showed frictionless sliding due to lattice mismatch while others behaved according to an atomistic Amontons' law where the friction force is proportional to size/area/load of the antimony islands, see Fig. 1.12. The ratio of vanishing friction to non-vanishing friction particles depends on the "dirtyness" of the samples, *i.e.*, the time of exposure to air or even to imperfect vacuum. Increasing dirt contamination diminishes the proportion of superlubric sliding. Following Müser, the *interfacial mobile molecule* hypothesis is a first candidate that could explain the observed duality, but it cannot explain why, under UHV conditions, superlubricity breaks down for some particles and does not for others. Surprisingly, even on the dirtiest samples, Dietzel *et al.* found two islands with vanishing friction, albeit for a sliding distance of less than 100nm. Therefore, the hope remains that superlubricity may be adopted to macroscopic engineering in some way or other.

Müser proclaims a rigid-body hypothesis based on the (length-scale dependent) ratio of interaction stiffness to bulk stiffness which must remain

smaller than unity in order to gain structural lubricity [34]. He stresses that ultralow macroscopic friction can only occur if the microscopic dynamics remain correlated on macroscopic length scales. In other words, the decisive incommensurability can get lost for too large and/or too flexible particles if their structure does not guarantee for a rigid-body like behavior. Promising model systems could be nanotubes or three-dimensional incommensurate crystals with atomically flat surfaces. The question of how nanotribological results concerning superlubricity may be adopted to explain (or better: explore) friction phenomena on the macroscopic level thus remains open.

The Prandtl–Tomlinson model from the last preceding subsection already comprises a mechanism leading to vanishingly small friction. If the elasticity κ exceeds the second derivative of the surface potential at its maximal value, $\kappa > U''(0)$, see Eq. (1.10), only a single mechanically stable position remains for the dynamical variable $x(t)$ at each time [35]. Then, the aforementioned hysteresis cannot occur and adiabatic motion will take place. In other words, stick–slip motion gives way to smooth sliding. Consequently, if the mechanism leading to energy dissipation is inhibited, only a vanishingly small amount of energy will be dissipated through the damping term. This scenario was already suggested by Prandtl [18]. If no other sources of friction are present (*e.g.*, surface contaminants, lattice defects, *etc.*), such a regime of ultra-low friction may also be termed superlubricity [7].

Experimentally, this kind of ultra-low friction that does not depend on incommensurate lattices was realized by Socoliuc *et al.* [36]. The experiment was performed with a silicon tip on a NaCl single crystal and in UHV at room temperature. They tuned the ratio of the surface potential to the stiffness of the contact by varying the normal load and could thus observe nearly vanishing (lateral) friction at small loads meaning small corrugation depth. Their results were acceptable as compared to a one-dimensional Prandtl–Tomlinson model, taking into account the two-dimensional averaging in case of the experiment. Remarkably, the state of ultra-low friction coincided with the disappearance of the stick–slip instabilities that otherwise contributed the most to the dissipation observed in FFM measurements.

More realistic two-dimensional simulations of superlubricity are recently performed by Steiner *et al.* delivering reasonably good agreement of numerical and experimental data [37]. They differentiate between three regimes of superlubricity: static superlubricity, dynamic superlubricity, and thermolubricity, see [38]. The first regime is the same as described above. The second one is achieved by externally applied actuation of the contact perpendicular to the sample surface, thereby facilitating load oscillations equivalent to an oscillating corrugation depth. If these oscillations correspond to a resonance frequency of the contact, the lateral friction decreases below the resolution of the FFM. The third regime refers to the suppression of the stick–slip phenomenon due to thermally activated transitions between potential minima.

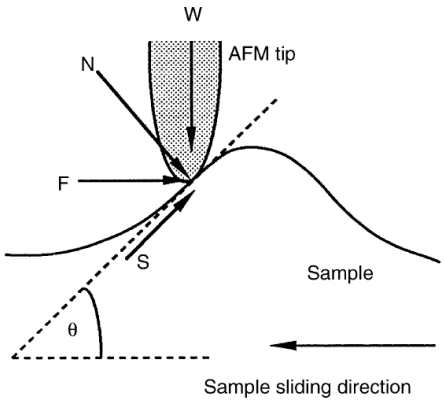

Figure 1.13: Schematic of the ratchet mechanism of a surface asperity. The AFM tip moves over an asperity that makes an angle θ with the horizontal plane. W and F are the normal and friction forces, respectively, and S and N are the force components along and perpendicular to the local surface of the sample at the contact point, respectively. Taken from [40].

1.3.4 Bhushan's "ratchet mechanism"

Experimental studies on homogeneous but rough materials showed a dependence of the lateral friction force rather on the slope of the surface asperities than on their height [39]. In contrast to the AFM tip that has a diameter of about 10 to 15nm, the surface asperities of this microscopically rough material are a few hundred nm in size. This obviously affords a geometrical explanation similar to the early explanation of friction leading to Eq. (1.2).

The situation is shown in Fig. 1.13. When the tip moves "uphill", the lateral deflection increases by an amount proportional to the load multiplied by $\tan\theta$, when it moves "downhill", the indicated friction force is reduced by the same amount since θ changes its sign. This effect generates two artificial peaks of the friction force, a positive one when the tip climbs up and a negative one when the tip comes down again. Bhushan calls this geometrical effect a *ratchet mechanism* [40], sometimes even a *ratchet effect* [41]. This somewhat unfortunate terminology should not be confused with the thermal ratchet effect which will be described in section 2.2.

1.4 Literature review

1.4.1 Books and reviews

The total number of publications concerning nanotribology, stick–slip motion, superlubricity, and thermal effects in atomic-scale sliding friction is well above 1 000 and still growing. Of course, the aim of this section can-

not possibly be a concise review of all current and/or past research activities in this field. Instead, this literature review focuses on a small number of (a) more general but essential publications and (b) more specific but thematically selected publications with relevance to this thesis. Therefore, the selection made herein does not claim to be complete.

Books

Starting with more general descriptions, a number of books should not go unmentioned. Those by Persson (*Sliding friction: Physical Principles and Applications* [6]) and Mate (*Tribology on the Small Scale: A Bottom Up Approach to Friction, Lubrication and Wear* [7]) have already been introduced earlier in this chapter. They combine descriptions and results of the various techniques in use for probing atomic-scale friction. Gnecco and Meyer have edited experimental and theoretical studies on *Fundamentals of Friction and Wear on the Nanoscale* [42]. Their main focus is on AFM experiments and their theoretical framework. Various contributions comprise contact mechanics, dissipation mechanisms, wear and fracture, nanoparticles, and organic materials.

Bhushan, besides editing a series of handbooks on applied scanning probe methods, has edited and partly written three books: an *Introduction to Tribology* [43] which contains a chapter on nanotribology besides a general survey of friction, wear, and lubrication; *Nanotribology and Nanomechanics: An Introduction* [44] offers more than 1 500 pages of divers experimental techniques, mainly AFM exploring different probes under various environmental conditions; together with Nosonovsky as a co-author, *Multiscale Dissipative Mechanisms and Hierarchical Surfaces: Friction, Superhydrophobicity, and Biomimetics* [45] presents a linkage between nanotribology and biological systems, with many examples of nanotechnology "made by nature", *e.g.*, the hierarchical structure of the adhesive hair bundles of gecko feet or the "lotus effect" of a nano-structured surface that largely diminishes adhesion, *etc*.

Reviews

Topical reviews and reports are less general than books but still summing up recent trends and open questions of nanotribology. One of the earliest reviews dates back to 1994, *Friction and energy dissipation at the atomic scale*, by Singer [46]. It focuses on wearless sliding as the most simple mechanism of atomic-scale friction dynamics. Both, minimal models and MD simulations, are discussed. The concept of frictionless sliding is investigated theoretically, including a reference to Hirano's and Shinjo's results [29].

In 2000, Robbins and Müser reported on *Computer Simulations of Friction, Lubrication and Wear* [47]. Various simulation techniques and their application to tribological problems are highlighted. The presented models range from simple one-dimensional crystalline surfaces to complex MD simulations including realistic hydrocarbon boundary lubricants. One section ad-

dresses the stick–slip phenomenon and microscopic models for its origins.

Gnecco *et al.* reviewed *Friction experiments on the nanometre scale* [48]. Their scope is on experimental result for variations of diverse parameters including load, velocity, anisotropy, *etc.* The importance of the Prandtl–Tomlinson model regarding atomic-scale dynamics is stressed. A logarithmic velocity dependence at low velocities is reported.

Müser *et al.* collected approaches to the molecular origins of friction based on statistical mechanics under the title *Statistical mechanics of static and low-velocity kinetic friction* [35]. In the case of dry elastic friction, they go much into details of the Prandtl–Tomlinson and the Frenkel–Kontorova model.

In *Nanotribology: Microscopic mechanisms of friction* [23], Braun and Naumovets describe the current state of research on friction from the point of view of surface science physicists. They mainly accentuate MD results and their connection to experiments.

The latest review, dating from 2008, *Recent advances in single-asperity nanotribology* [49] by Szlufarska *et al.*, reflects recent advances in the experimental, theoretical, and computational studies of nanotribology. In particular, it focuses on the latest developments in atomic force microscopy and MD simulations and their application to the study of single-asperity contacts.

1.4.2 Velocity dependence of atomic-scale friction

Classical friction of macroscopic bodies does not depend on the sliding velocity, an empirical fact known as Coulomb's law for a long time. This relation is only valid within specific boundaries (*e.g.*, low velocities, normal ambient conditions, no viscous flow/very low Reynolds number). Outside of these boundaries, friction is known to exhibit different kinds of velocity dependence: in viscous fluids, swimming bodies experience Stokes friction which is proportional to the velocity, and bodies moving in air are decelerated by the air drag which, at intermediate to high velocities, is proportional to the velocity being squared or even cubed.

Most likely, atomic-scale friction will depend on velocity in one way or another—save the special case of unmeasurable low friction (superlubricity). Many different relations have been proposed by numerous researchers, some of them even in obvious contradiction to others. There is a simple reason for this confusing situation: the scanning velocities of the AFM are limited to very low values, typically ranging from nm/s to a few µm/s. This might be enough to exclude those hypotheses which are the farthest from reality, but it is not enough to corroborate any of the remaining theories beyond doubt.

A reasonable approach to the velocity dependence of atomic scale friction is to assume thermal activation to be a key ingredient that causes the stick–slip phenomenon of the tip's Brownian motion. In this case, Kramers rate

theory of thermally activated escape can be applied to the dynamics of the tip. The interstitial stick–slip motion proceeds in jumps of unit cell length with respect to the periodic surface potential: after overcoming a potential barrier, the tip relaxes to the next local minimum and the escape process starts anew. The force-dependent rate of escape, $\omega(F)$, is equivalent to the inverse of the average waiting time, provided that thermalization within the new minimum is fast as compared to this waiting time (Markov process). The pulling velocity v then can be deduced from the unit cell length a times the rate $\omega(F)$,

$$v = a\omega(F)\,. \tag{1.18}$$

The rate is an exponential of the energy barrier hight and (in a first approximation, as long as variations of the pulling force are small, *e.g.*, for a weak cantilever) depends linearly on the force. This immediately implies a logarithmic dependence of the average friction force on the pulling velocity,

$$F \propto \ln \frac{v}{v_0}\,. \tag{1.19}$$

The intrinsic velocity v_0 is mainly comprised of the unit cell length a and the Arrhenius factor ("attempt frequency") of the Kramers rate.

Deviations from this purely logarithmic dependence are to be expected in the more general case of larger force fluctuations and higher pulling velocities. A master equation links the instantaneous Kramers rate $\omega(t)$ to the probability $p(t)$ that the tip has not yet escaped from a potential minimum, *i.e.*, the slip has not yet occurred,

$$\dot{p}(t) = -\omega(t)p(t)\,. \tag{1.20}$$

As usual, the overdot symbols differentiation with respect to the time. Since backward jumps are highly improbable, they are not taken into account. The quantity $\dot{p}(t)$ thus can be understood as the rate of depletion of the system state corresponding to that local minimum being occupied at time $t = 0$.

The force–time diagram of the stick–slip motion resembles a saw-tooth pattern, where the instantaneous force grows linearly in the time between two jumps and in direct proportion to the deflection of the tip,

$$f(t) = f_0 + \kappa v t\,. \tag{1.21}$$

Here, f_0 is the restoring force of the bent cantilever at time $t = 0$ right after a jump into the local minimum has occurred.

Substituting this force–time relation into the master equation (1.20) yields

$$\frac{dp(f)}{df} = -\frac{1}{\kappa v}\,\omega(f)p(f)\,. \tag{1.22}$$

A first order approximation for the average force is given by the force f^* that maximizes the probability current. It can be found by solving $d^2p(f)/df^2 = 0$ for $f = f^*$. This leads to $d\omega(f)/df|_{f=f^*} = [\omega(f^*)]^2/\kappa v$, finally yielding the proportionality relation

$$v \propto f^* \omega(f^*)\,, \tag{1.23}$$

where $\omega(f)$ still is assumed to depend exponentially on f^*. The inverse of this relation does not exist in closed form, but depending on further system parameters, this relation gives rise to modifications of the plainly logarithmic force–velocity relation, Eq. (1.19).

Following this line of reasoning, thermally activated Brownian motion was studied by Evstigneev and Reimann within theoretical models for a paradigmatic force–velocity relation. Their first attempt resorted to overdamped motion in tilted periodic potentials [50], using analytical results first obtained by Stratonovitch. They predict a velocity maximum which can be approximately described by a universal scaling law. The following papers [51–53] developed a description of stick–slip motion in terms of forced Brownian motion in a multi-stable potential landscape, where the transition rates between potential minima can be determined by the Kramers reaction rate theory.

In Ref. [20], it has proven necessary to introduce an *effective* spring constant that is weakly velocity dependent, thereby improving the agreement of the rate deduced force–velocity relation with numerical simulations of the corresponding Fokker-Planck equation. In cooperation with the experimental group of Schirmeisen in Münster, Evstigneev, Schirmeisen *et al.* analyzed AFM data with regard to force-dependent transition rates [54]. They found a good accordance only for high velocities and suggest that a formation of multiple bonds could be responsible for the substantially lower rates at low velocities, an effect termed "contact aging".

In 2008, together with Schirmeisen *et al.*, the investigation of low velocities due to *Contact ageing in atomic friction* [55] was continued. Within a simplified model of the contact ageing process, their theoretical predictions and the experimental results were in reasonable agreement with each other. This implies the importance of time-dependent changes in the properties of single asperity contacts, namely time dependent transitions to stronger bound states during stick-phases.

Only a small selection from the multitude of experimental results and further theoretical findings shall be presented here. First experimental findings in favor of the thermal activation scenario date back to the 1990s. A logarithmic velocity dependence of atomic-scale friction was found by Bouhacina *et al.* when exploring the *Tribological behavior of a polymer grafted on silanized silica probed with a nanotip* [56]. They explained this behavior with the Eyring model that expands the thermal activation of reaction rate theory with an external stress term representing the pulling force in terms of an external bias.

Dudko *et al.* promote the use of a thermally activated Prandtl–Tomlinson model to describe results obtained by dynamical force spectroscopy [21]. This offers a new possibility to extract detailed information of the surface potential and the dissipation mechanisms from the measured force–velocity relations.

A distinction between "ramped" and "linear creep" was introduced by Sang *et al.* [58]. Linear creep describes the sliding friction of an extended contact region (*e.g.*, two plates in slow relative motion, *constant* bias) and implies a logarithmic velocity dependence of friction, as before. But in case of atomic-scale stick–slip motion, the force is modulated quasi-periodically, with a linearly increasing force interrupted by downward jumps, which they call ramped creep. By incorporating this sawtooth pattern into their dynamical model, Sang *et al.* found a logarithmic power law, $F \propto \text{const} - T^{2/3}\,|\ln(v/T)|^{2/3}$, in dimensionless units, that displayed a convincing collapse of experimental data recorded at different temperatures.

In *A comparative study of the one- and two-dimensional Tomlinson model*, Fusco and Fasolino inquired athermal and thermal contributions to the expected velocity dependence of atomic-scale friction [59]. They found out that the interplay of several system parameters (*e.g.*, corrugation depth, cantilever stiffness, and a phenomenological damping term) crucially influences the resulting velocity.

But there also have been measurements in contradiction to a logarithmic velocity dependence of friction. While Bouhacina *et al.* studied velocities at nm/s, Zwörner *et al.* chose much higher velocities, namely µm/s [60]. They found friction to take on values that were independent of the pulling velocity. This is in agreement with an athermal Prandtl–Tomlinson model, where the intrinsic noise is sufficiently negligible. At higher velocities, viscous damping sets in leading to a linear dependence of the friction force on the velocity.

Gnecco *et al.* again measured (at nm/s) a logarithmic force–velocity relation of an FFM tip on NaCl(100) and explained this via a thermally activated Prandtl–Tomlinson model [61]. Measurements over five orders of magnitude in pulling velocity were performed by Riedo, Gnecco *et al.* [62]. They combined a logarithmic increase at low velocities with a saturation at the µm/s level and found a *plateau* beyond some critical velocity.

1.4.3 Controlling atomic-scale friction

Changing parameter values between different regimes of friction (*i.e.*, between stick–slip and smooth sliding, into or out of the thermo- or superlubric regime) offers the opportunity to control friction actively on the atomic scale.

In 2005, Krylov *et al.* discussed a *Thermally induced suppression of friction at the atomic scale* [63], where they introduced a distinction between *thermol-*

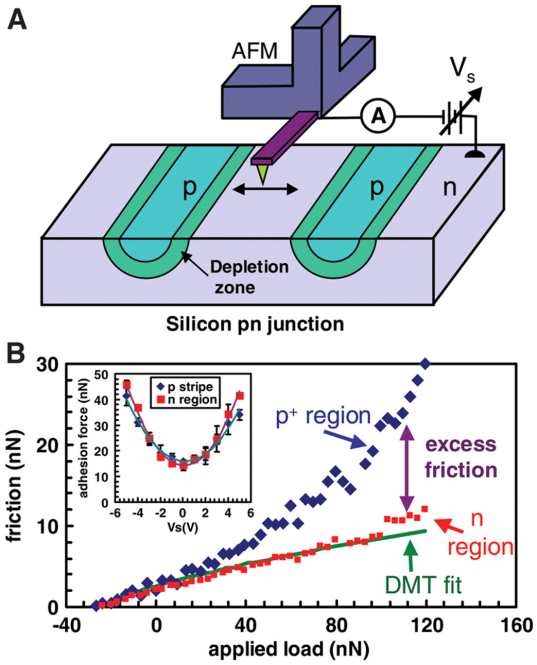

Figure 1.14: (A) Schematic of AFM measurements on a silicon p–n junction device. (B) Plot of friction force as a function of applied load at +4V sample bias. The scanning speed was 5 µm/s. (Inset) The pull-off force as a function of sample bias. The error scales represent the standard deviation from five independent measurements. Taken from Park *et al.* [66].

ubricity and *thermal drift*. The former is applied to a reduction in friction by thermal activation, the latter to a suppresion of dissipation by quasi-adiabatic sliding comparable to superlubricity. There is a reasonable agreement between their theoretical findings and known experiments [31, 36].

A different approach is tuning friction by mechanical excitations. Tshiprut *et al.* demonstrated how lateral vibrations of a substrate can increase surface mobility and diffusivity, thereby reducing friction at the atomic scale [64]. A complete elimination of the lateral force fluctuations cannot be achieved in this way—and probably this is not desirable because of the important role the fluctuations play for thermal activation.

Normal vibrations can also effect friction in an atomic force microscope, as was shown by Jeon *et al.* [65]. They observed a reduction of the friction coefficient by a few orders of magnitude when periodic out-of-plane surface vibrations were stimulated. They compared their experimental findings to computer simulations of a one-dimensional Frenkel–Kontorova chain representing the tip–sample contact.

Control of friction by normal vibration as well as electronic control in sil-

icon p–n junctions were outlined by a series of articles in the Science Magazine [66]. Therein, Socoliuc *et al.* reported how they excited the mechanical resonances of the tip–cantilever system perpendicular to the contact plane and reduced friction below 10pN. Park *et al.* observed a dependence of friction on the predominant charge carrier concentration, see Fig. 1.14. Although the p regions of a doped Si-surface lead to an increasing dissipation with increasing load of the TiN tip, the sliding was perfectly wearless.

An important examination of the "fine structure" behind the stick–slip dynamics was performed by Maier *et al.* in 2005 [67]. Results were compared with simulations based on an extended Prandtl–Tomlinson model including thermal fluctuations. They observed that the slip process can happen on very different time scales (from below 15 µs up to some 10 ms). They apply a two-spring model with different elasticities for tip–contact and cantilever, and suggest that multiple asperities in contact may be responsible for the observed variety of slip durations.

Krylov *et al.* go one step further and do not only propose a two-spring model but a two-mass–two-spring model [68], where the tip apex is included as a highly flexible and extremely small mass. In consequence, the tip apex performs rapid thermal fluctuations (some GHz) which lead to a delocalization of the contact. Nevertheless, stick–slip motion of the cantilever is preserved since the surface corrugation is still superimposed to the average elastic force of the apex.

In 2008, Tshiprut *et al.* also have examined the two-mass–two-spring model and could successfully explain the "fine structure" of slip events [69]. Furthermore, they have found a range of parameter values for which the well-known single-spring Prandtl–Tomlinson model is applicable.

2 Theoretical aspects of Brownian motion

Une intelligence qui, à un instant donné,
connaîtrait toutes les forces dont la nature est animée
et la situation respective des êtres qui la composent,
si d'ailleurs elle était assez vaste pour soumettre ces données à l'analyse,
embrasserait dans la même formule les mouvements des plus grands corps
de l'univers et ceux du plus léger atome:
Rien ne serait incertain pour elle,
et l'avenir, comme le passé, serait présent à ses yeux.

Pierre Simon de Laplace

2.1 Brownian motion in tilted periodic potentials

2.1.1 Connection to nanotribology

As mentioned in the previous chapter, full-fledged MD simulations of a 2D sliding contact region containing hundreds of atoms in multiple layers of probe and sample (plus some extra layers of a lubricant if the contact is not dry) are expensive in terms of computer time. This is mostly due to the fact that every single channel of dissipation (predominantly the creation of phonons in substrate and cantilever) must be taken into account. Therefore, the resources necessary to resolve a significant time span of the motion of a macroscopic body will be beyond reach until some distant future—a silicon-based *Laplacian demon* is not in sight yet. Furthermore, simulation results reveal that our current understanding of dissipation in sliding contacts must be either incomplete or, in some parts, wrong. The reason is the discrepancy in the values of the force–velocity relation, especially the velocity at which smooth sliding sets in. Simulation results for "realistic" sliding con-

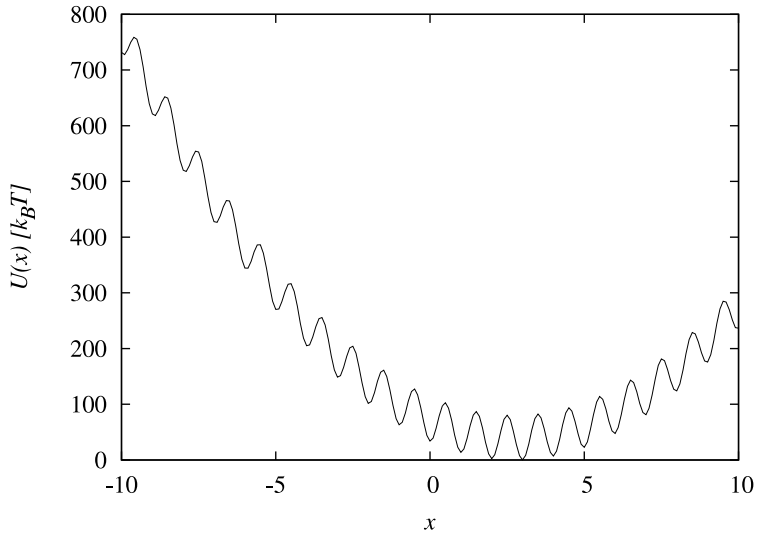

Figure 2.1: Superposition of a sinusoidal and a parabolic potential, where x denotes the lattice site in arbitrary units. For a weak spring, the constantly pulled tip mostly resides at one of the tilted flanks where the total potential locally is very similar to a tilted periodic potential.

tacts yield a critical velocity that exceeds the experimentally observed value by more than six orders of magnitude [23].

It does not come as a surprise that recent success has been achieved by leaving the basis of pure MD and applying an earthquakelike model to sliding friction where the formation and rupture of mesoscopic bonds is statistically described via a master equation approach [70]. This approach systematically separates the calculation of the friction force from the studies of the properties of the contacts and thus can reduce the error in the critical velocity by two orders. In this context, the method we have chosen for our own research on atomic-scale friction phenomena seems not to be utterly unjustified, namely, to resort to minimalist models that are well suited for characteristic situations frequently encountered in experimental nanotribology (*e.g.*, the sliding of a few point contacts).

In subsection 1.3.2, a general setup already was described in Eqs. (1.3)–(1.9): the Brownian motion of a single atomic contact under the influence of a lateral pulling with constant velocity,

$$m\ddot{x}(t) = -U'\big(x(t)\big) + \kappa\big(x(t) - vt\big) - \eta\dot{x}(t) + \xi(t)\,. \tag{2.1}$$

The sum of a sinusoidal surface potential and a parabolic spring potential can be seen in Fig. 2.1. If κ is sufficiently small, the dynamics of the tip will be such that $x(t)$ resides in a local minimum until the pulling has moved it "up" one of the tilted branches of the potential. There, the effective barrier height is substantially reduced and thermally activated transitions to lower

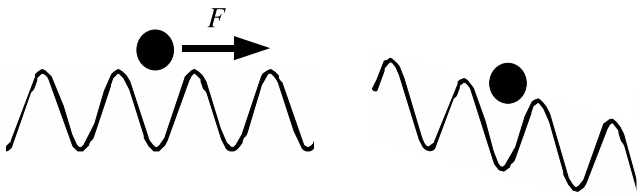

Figure 2.2: For a particle in a periodic potential there is no difference wether it is pulled with a constant force or the potential is tilted with a constant bias. Arithmetically, both descriptions are equivalent.

minima can take place. On average, $x(t)$ cycles up (by pulling) and down (by hopping) around a small region of the potential that can locally be described by a tilted periodic potential.

Furthermore, this minimalist model of atomic-scale sliding friction can easily be dealt with in the framework of *overdamped* Brownian motion in tilted periodic potentials. Since the effective mass of the tip is extremely small ($m \leq 3 \times 10^{-12}$ kg, as it is conservatively estimated in Ref. [53]), it is possible to neglect inertia completely. Taking into account some realistic values for the corrugation depth of the sinusoidal potential (say, $100\,k_{\mathrm{B}}T$, which is about 4×10^{-19} J at room temperature), of the cantilever and tip elasticity (about 1 N/m, where the tip is much more flexible than the torsional mode of the cantilever with 75 N/m, respectively), and a lattice spacing of 0.5 nm, the tip must be bent across a few lattice sites before the restoring force is strong enough to overcome the energy barrier of the surface potential.

The resulting overdamped equation of motion reads

$$\eta\dot{x}(t) = -U'\big(x(t)\big) + F(t) + \xi(t)\,, \tag{2.2}$$

where $F(t) = \kappa\big(x(t) - vt\big)$. Provided that κ is small, only the hopping transitions to neighboring lattice sites make a substantial contribution to $F(t)$ whereas the thermal fluctuations *within* the same minimum can be neglected. From this, we exactly recover the overdamped Brownian motion in a tilted periodic potential as it is discussed in numerous publications, see Ref. [22]. It is arithmetically irrelevant whether the (slowly varying) force term appears on its own or as an additional term of the potential, $U^{\mathrm{tot}} = \big(U(x) - F(t)x\big)$, which is known as a *tilted* periodic potential, see Fig. 2.2—the equation of motion stays the same.

The concept of a Brownian walker in a tilted periodic potential is a quite general one with many known results. Following the connection to atomic friction as explained above, results obtained from Brownian motion in tilted periodic potentials can be transfered more or less directly into the framework of nanotribology.

2.1.2 Analytical results for velocity and diffusion coefficient

Under the influence of a constant force, *i.e.*, a tilted potential without any periodic modulation, the velocity and diffusion coefficient of a Brownian particle are easily found:

$$v = F/\eta \quad \text{and} \quad D = k_\mathrm{B}T/\eta, \tag{2.3}$$

where η and T refer to this test particle's viscosity and temperature, respectively. The latter is the well-known Einstein relation, dating back to Einstein's *annus mirabilis* 1905 [71].

A mathematically rigorous way to treat Brownian motion was introduced by Norbert Wiener (1894–1964). In the case of an unmodulated tilted potential, the particle's dynamics is a biased Wiener process. It is known that for the Wiener process (and for the more general case of a modulated potential as well) the dynamics of the particle can be derived from the moments of the first passage time. These are the statistical averages of the times $t(x \to b)$ to reach an arbitrary but fixed boundary b, starting from an initial point x,

$$T_n(x \to b) := \langle t^n(x \to b) \rangle \,, \tag{2.4}$$

where the subscript n denotes the n-th moment. In the overdamped regime, a well-known analytical recursion exists in closed form [72], starting with the constant term $T_0(x \to x') \equiv 1$, with arbitrary x'. For all moments with positive integer n, the recursion reads:

$$T_n(x \to b) = n \frac{\eta}{k_\mathrm{B}T} \int_x^b dy\, e^{V(y)/k_\mathrm{B}T} \int_{-\infty}^y dz\, e^{-V(z)/k_\mathrm{B}T}\, T_{n-1}(x \to z) \,. \tag{2.5}$$

For an arbitrary amount Δx of the test particle's displacement, the velocity is given by

$$v = \Delta x / T_1(x \to x + \Delta x) \,. \tag{2.6}$$

Similarly, the diffusion coefficient is related to the first and second moment of the first passage time via

$$D = \frac{\Delta x^2}{2} \, \frac{\Delta T_2(x \to x + \Delta x)}{T_1^3(x \to x + \Delta x)} \,, \tag{2.7}$$

where $\Delta T_2(x \to b) := \langle t^2(x \to b) \rangle - \langle t(x \to b) \rangle^2 = T_2(x \to b) - T_1^2(x \to b)$ is the so-called first passage time dispersion. These expressions may also serve as definitions in the case of a modulated potential, provided that Δx is sufficiently large.

For a Brownian particle in a tilted potential with periodic modulation, the question is not as simple. Both v and D will instantaneously as well as on

average depend on the particle's position x because the force acting on the particle will vary with x as $F(x) = -V'(x)$. The problem becomes irrelevant on a large length scale, where the small-scale fluctuations of the particle's position will be negligible in comparison to the total displacement of the particle. Instead of the true viscosity η and temperature T in a modulated potential, we compare the particle's motion to a test particle without periodic potential modulation and find an effective viscosity η' and temperature T' that will generate the same effective velocity and diffusion. The question is, how to link the simple model of a test particle in a tilted potential and the more general case of a modulated potential?

Since the diffusion process under consideration has no memory, the first passage times are distributed independently and thus are additive quantities, $T_1(x \to b) = T_1(x \to a) + T_1(a \to b)$ and $\Delta T_2(x \to b) = \Delta T_2(x \to a) + \Delta T_2(a \to b)$, for an arbitrary inner point a, *i.e.*, $x \leq a \leq b$. Therefore, in the case of a periodic potential with period L, we can subdivide Δx into $N = \lfloor \Delta x/L \rfloor$ full periods plus a remaining distance $\delta x = \Delta x - NL$, so that

$$T_1(x \to x + \Delta x) = NT_1(x \to x + L) + T_1(x \to x + \delta x) \tag{2.8}$$

and

$$\Delta T_2(x \to x + \Delta x) = N\Delta T_2(x \to x + L) + \Delta T_2(x \to x + \delta x)\,. \tag{2.9}$$

Clearly, in the limit of large N, the δx-dependent remainders become negligibly small as compared to those summands scaling with N. Thus, the diffusion coefficient in a (tilted) periodic potential is fully determined by the first and second moment of the first passage time for a single lattice spacing L,

$$D = \frac{L^2}{2}\,\frac{\Delta T_2(x \to x + L)}{T_1^3(x \to x + L)}\,, \tag{2.10}$$

as can be seen by substituting Eqs. (2.8) and (2.9) into (2.7).

After some manipulation (the details of which can be found in Refs. [73, 74]), the velocity and the diffusion coefficient of a Brownian particle in a tilted periodic potential are given by the exact analytical expressions

$$v = \frac{1 - e^{-LF/k_\mathrm{B}T}}{\displaystyle\int_{x_0}^{x_0+L} \frac{dx}{L}\, I_\pm(x)} \tag{2.11}$$

and

$$D = \frac{k_\mathrm{B}T}{\eta}\,\frac{\displaystyle\int_{x_0}^{x_0+L} \frac{dx}{L}\, I_\pm(x)\, I_+(x)\, I_-(x)}{\displaystyle\left(\int_{x_0}^{x_0+L} \frac{dx}{L}\, I_\pm(x)\right)^3}\,, \tag{2.12}$$

where the integrals

$$I_{\pm}(x) := \frac{\eta}{k_{\mathrm{B}}T} \int_0^L dz \, \exp\left(\pm \frac{V(x) - V(x \mp z)}{k_{\mathrm{B}}T} \right) \tag{2.13}$$

are introduced for convenience.

These results facilitate the calculation of the test particle's effective velocity and diffusion coefficient from the modulated potential. But the physical meaning of the diffusion coefficient is merely limited to the very short relaxation time of a model point contact within the multi-stable potential landscape that is enclosed by the confining spring potential of the cantilever. After relaxation is complete, the local distribution of the tip's position keeps its finite width depending mainly on the spring constant and the temperature—in case of an unmodulated potential this is known as the Ornstein–Uhlenbeck process which we will refer to later. Since this is due to the contact sensing the parabolic part of the total potential, the diffusion coefficient as obtained from a tilted periodic potential has no longer any physical meaning, not to mention that it cannot be measured at all.

There is a different dynamical quantity with a comparable statistical meaning. Regarding atomic-scale stick–slip motion, the waiting times and their moments are perfectly accessible to measuremet. From Eq. (2.10) we infer

$$\Delta T_2 = 2DT_1^3/L^2 = 2DL\,(T_1/L)^3 = 2DL/v^3, \tag{2.14}$$

which enables us to deduce the waiting time dispersion of the tip's dynamics from its pulling velocity and the diffusion constant for a corresponding test particle. For a linearly increasing pulling force, $F(t) = \kappa\big(x(t) - vt\big)$, the waiting time dispersion is linked to the distribution width of the instantaneous forces at which the transition of the tip to the neighboring minimum occurs.

While the result for the particle's average velocity, Eq. (2.11), has been obtained by Ruslan Leont'evich Stratonovitch (1930–1997) half a century ago [73], the extension to the diffusion coefficient, Eq. (2.12), was established at the beginning of the new millennium by Reimann *et al.* [74]. The most important consequence of this extension is the precise prediction of an enormous diffusion peak that can arise at close to critical tilt, see Fig. 2.3. The main reason for this *giant acceleration of free diffusion* is a pronounced maximum of the first passage time dispersion due to the extended flat regions of the potential. In case of a sinusoidal potential, there is a saddle-node bifurcation at the critical tilt where relative minima and maxima converge with the inflection point so that both gradient and curvature of the potential vanish simultaneously. Due to the "dynamical bottlenecks" that arise within each period of the potential, the distribution of first passage times out of these flat regions increases dramatically: particles may with nearly equal probability

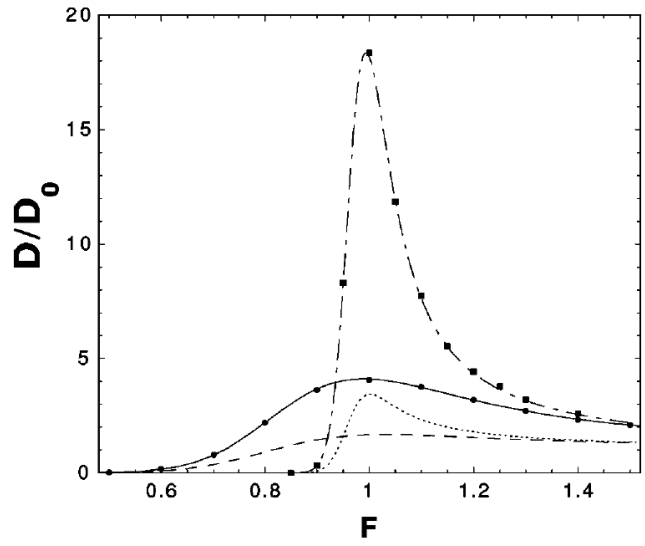

Figure 2.3: Diffusion coefficient as a function of the tilt F of a sinusoidal periodic potential, in dimensionless units. D_0 is the free diffusion coefficient $k_\mathrm{B}T/\eta$. $F = 1$ corresponds to the critical tilt (onset of deterministically running solution). Comparison of numerical simulation (dots) to analytical predictions at $k_\mathrm{B}T = 0.1$ (solid line) and $k_\mathrm{B}T = 0.01$ (dashed-dotted line). Other lines (dashed and dotted) represent an alternative model. Taken from [75].

"slide through" without much hindrance as well as reside in place for a very long time. For a suitably chosen set of parameter values (such as the viscosity and the ratio height of potential barriers to thermal energy), the effective diffusion may well exceed the free diffusion by more than an order of magnitude. This effect is of great practical relevance, *e.g.*, to facilitate the sorting or mixing of different species of suspended particles in microfluidic devices.

2.2 The ratchet effect

2.2.1 Historical notes

In 1912, at a congress of the *Gesellschaft Deutscher Naturforscher und Ärzte* in Münster, Marian Smoluchowski (1872–1917) proposed a *Gedankenexperiment* for a molecular ratchet. At that time, several scientists questioned the validity of the second law of thermodynamics on the molecular scale. In their artless reasoning, some simple mechanical device could rectify the thermal fluctuations of a heat reservoir and thereby produce utilizable work. A prominent example of a hypothetical rectifier is known as the Maxwell demon. Of course, such a mechanism would be tantamount to a *perpetuum mobile* of the second kind and thus violate the second law as formulated by Kelvin.

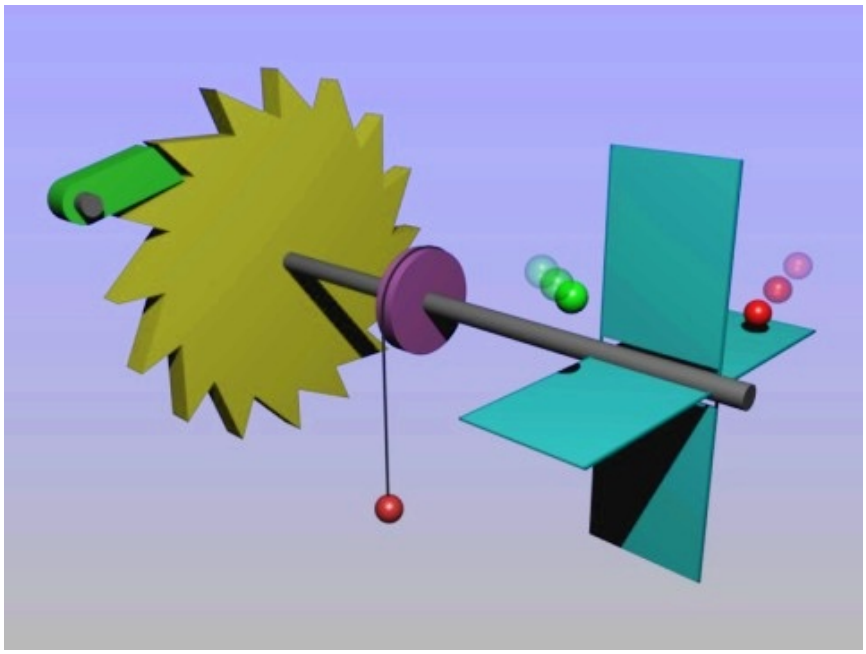

Figure 2.4: A ratchet-and-pawl device illustrating Feynman's *Gedankenexperiment*. If it worked properly, the thermal fluctuations of gas molecules at the paddle-wheel could only move the axle in one direction whereas motion into the opposite direction should be prohibited by the pawl. A small weight thus could be lifted against gravity. Taken from [78].

Smoluchowski demonstrated in a series of counterintuitive examples why such a machine cannot work properly, at least not on arbitrary time scales [76]. Although it is possible to construct microscopical systems that, in principle, are able to violate the second law, the mean waiting time until one will observe a violation increases, according to Boltzmann, exponentially with the weight of the violation which is to be measured in units of thermal energy. Large scale fluctuations in molecular systems thus emerge about once during 10^{10^x} years, where $x \gg 1$. Followingly, the mean waiting time may outlast the age of our universe by many orders of magnitude. One can safely argue that such giant fluctuations will, for all practical reasons, never occur.

Richard Phillips Feynman (1918–1988) explicitly calculated through a ratchet-and-pawl device [77] as depicted in Fig. 2.4. Regarding its strength, the pawl is subject to two competing restrictions, namely, it must be weak enough to let the axle slip into the wanted direction and, at the same time, it must be strong enough to prevent it from slipping backward. Feynman arrived at the conclusion that these restrictions exclude one another in any system of molecular size. If the thermal fluctuations on the paddle-wheel and the ratchet-and-pawl sides are comparable, then transitions between neighboring teeth of the cog-wheel are equally probable despite of its asymmetry.

However, Feynman observed that a modification of the ratchet-and-pawl device with different heat baths on both sides opens a pathway to circumvent the aforementioned restrictions. If the ambient temperature of the pawl mechanism is smaller than the ambient temperature of the paddle-wheel, the whole device acts as a molecular heat engine and can produce utilizable work without any difficulty and in full compliance to the second law. In this way, the simple ratchet-and-pawl mechanism turns into a prototypical Brownian heat engine, and the mechanism leading to unidirectional transport (*i.e.*, a broken symmetry and the departure from thermal equilibrium) is termed the ratchet effect. Its characteristic is the existence of a non-zero current without any external force. This means that, in a one-dimensional dynamical system $x(t)$, the ratchet effect is sufficiently described by

$$F = 0 \quad \Rightarrow \quad \langle \dot{x} \rangle \neq 0 \,, \tag{2.15}$$

where F is the applied force and $\langle \dot{x}(t) \rangle$ the average velocity.

For eight decades following Smoluchowski's talk, there have been publications from distant areas implying a ratchet effect for muscle contraction, molecular pumps, DC-SQUIDs (super conducting quantum interference devices), photovoltaic and -refractive effects, see Ref. [75] for a review. Yet the coverage of these works was narrow and important discoveries remained unnoticed by most colleagues. This lasted until the early 1990s, when the quest of the ratchet effect experienced a downright boom due to its re-invention for modeling molecular motors [79]. Soon, the scope widened to Brownian motors in general and their embedding into statistical mechanics, entailing theoretical as well as experimental contributions.

Today, the ratchet effect is considered as a fully approved member of the family of noise-induced or -assisted non-equilibrium phenomena, *e.g.*, stochastic resonance, noise induced (phase) transitions, reaction rate theory, and driven diffusive systems. A prime example of the ratchet effect that we will re-encounter in Chapters 4 and 5 is a pulsating ratchet, the so-called *on–off ratchet*. It is discussed, together with a summary of its theoretical framework, within the following subsections.

2.2.2 A minimal ratchet model

In order to elucidate the ratchet effect, an exact model of the Smoluchowski–Feynman ratchet is by far too intricate. Therefore, a minimalized version that comprises all relevant aspects of the original gadget but with as few variables and parameters as possible is to be preferred because its only purpose is purely to demonstrate the ratchet effect.

In the most simple fashion, we consider a Brownian particle in a one-dimensional periodic potential, $V(x) = V(x + kL)$, where k is an integer. A

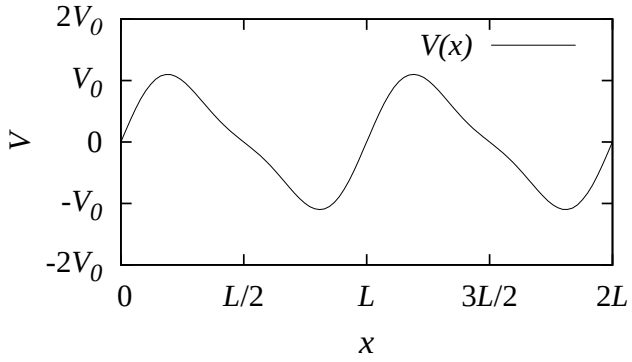

Figure 2.5: A commonly used *ratchet potential*, Eq. (2.16).

so-called *ratchet potential* with a suitably built-in asymmetry is commonly used,

$$V(x) = V_0 \left(\sin \frac{2\pi x}{L} + \frac{1}{4} \sin \frac{4\pi x}{L} \right), \tag{2.16}$$

see Fig. 2.5. The complete equation of motion reads

$$m\ddot{x}(t) = -V'\big(x(t)\big) - \eta\dot{x}(t) + \xi(t)\,, \tag{2.17}$$

with analogous notation as in Eq. (1.7). Again, $\xi(t)$ is an unbiased Gaussian white noise.

In case of a microscopically small system, inertial forces are marginal as compared to all other terms and the limit $m \to 0$ can safely be applied, thus yielding an *overdamped* equation of motion,

$$\eta\dot{x}(t) = -V'\big(x(t)\big) + \xi(t)\,. \tag{2.18}$$

Discretization in the time–domain yields a numerically tractable scheme allowing computer simulations of the stochastic dynamics. Choosing a small time increment Δt and replacing $\dot{x}(t)$ by $\left[x(t_{n+1}) - x(t_n)\right]/\Delta t$, where $t_n := n\Delta t$, leads to

$$x(t_{n+1}) = x(t_n) - \frac{\Delta t}{\eta}\left[V'\big(x(t_n)\big) + \xi_n\right], \tag{2.19}$$

which is an explicit Euler algorithm applied to Eq. (2.18). The time discretization of the stochastic process $\xi(t)$ results in a set of independent random numbers ξ_n that are Gaussian distributed with zero mean and where

$$\langle \xi_n^2 \rangle = \frac{2\eta k_\mathrm{B} T}{\Delta t} \tag{2.20}$$

determines the second moment.

It is instructive to look at the corresponding Fokker–Planck equation that can be deduced from simple considerations in a heuristic way. If one is interested not so much in a certain trajectory but in an ensemble average of many such stochastic processes based on different realizations of the noise term $\xi(t)$, one focuses on the probability density $P(x,t) := \langle \delta\big(x - x(t)\big) \rangle$. Its time evolution is governed by two fundamental contributions: drift and diffusion.

In the deterministic limit, *i.e.*, for $T \to 0$, the noise is constantly zero and the time evolution of $P(x,t)$ obeys a Liouville–Equation,

$$\frac{\partial}{\partial t} P(x,t) = \frac{\partial}{\partial x} \left(\frac{k_\mathrm{B} T}{\eta} P(x,t) \right). \tag{2.21}$$

In case of $V'(x) = 0$, only thermal fluctuations govern the time evolution of $P(x,t)$. This scenario is captured by the diffusion equation

$$\frac{\partial}{\partial t} P(x,t) = \frac{k_\mathrm{B} T}{\eta} \frac{\partial^2}{\partial x^2} P(x,t). \tag{2.22}$$

A superposition of both contributions yields the Fokker–Planck equation

$$\frac{\partial}{\partial t} P(x,t) = \left[\frac{\partial}{\partial x} \left(\frac{V'(x)}{\eta} + \frac{k_\mathrm{B} T}{\eta} \frac{\partial}{\partial x} \right) \right] P(x,t) \tag{2.23}$$

which is also known as the Smoluchowski equation. Hence, the Fokker–Planck operator which is enclosed in square brackets is said to comprise a "drift term" and a "diffusion term".

The probability current $J(x,t)$ is defined by $J(x,t) := \langle \dot{x}(t)\, \delta\big(x - x(t)\big) \rangle$. Please, note that x is a coordinate, whereas $x(t)$ is a stochastic process. By means of a continuity equation for the probability density,

$$\frac{\partial}{\partial t} P(x,t) + \frac{\partial}{\partial x} J(x,t) = 0\,, \tag{2.24}$$

the probability current $J(x,t)$ is readily expressed by

$$J(x,t) = -\left(\frac{V'(x)}{\eta} + \frac{k_\mathrm{B} T}{\eta} \frac{\partial}{\partial x} \right) P(x,t). \tag{2.25}$$

This is related to the average particle current $\langle \dot{x} \rangle := \langle \dot{x}(t) \rangle$ via

$$\langle \dot{x} \rangle = \int_{-\infty}^{\infty} dx\, J\,(x,t)\,. \tag{2.26}$$

It should be mentioned that, "as far as the particle current $\langle \dot{x} \rangle$ is concerned, it suffices to solve the Fokker–Planck equation with periodic boundary (and initial) conditions" [75]. This permits to reduce open boundaries (in case of infinitely stretched domains) to a finite, periodic boundary which are more "nicely" implemented on a computer.

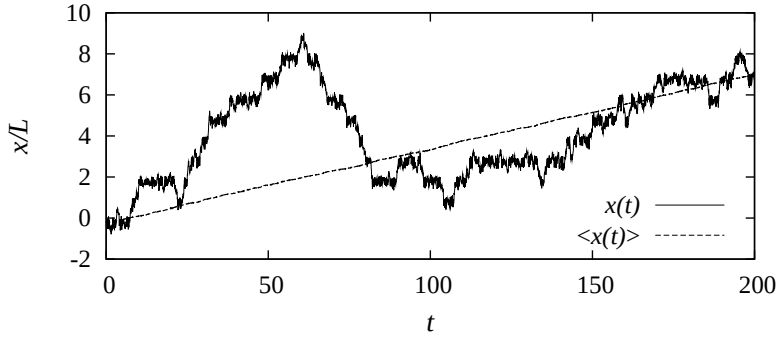

Figure 2.6: A single trajectory (solid line) and an ensemble average (dashed line) of the on–off ratchet system, Eq. (2.27). Parameter values were $V_0 = L = \eta = 1$, $k_\mathrm{B}T = 0.1$, $\Delta t = 0.05$, and the period of $f(t)$ is $\tau = 2$.

2.2.3 The on–off ratchet

The on–off ratchet is a subclass of the so-called *pulsating potential* ratchets, *i.e.*, the potential is modulated by a time-periodic signal $f(t) = f(t+\tau)$ with period τ. In case of the on–off ratchet, the time modulation is a rectangular signal periodically switching between 1 and 0 so as to switch the potential either "on" or "off". Eq. (2.18) thus is modified to

$$\eta\dot{x}(t) = -V'\big(x(t)\big)\, f(t) + \xi(t)\,. \tag{2.27}$$

The essential meaning of this modification is the destruction of the detailed balance symmetry in order to put the system periodically out of thermal equilibrium. Without this built-in "disturbance", there could not be any ratchet effect due to Curie's principle. The situation would be equivalent to a Smoluchowski–Feynman ratchet with only a single heat bath.

Results from computer simulations of the Langevin equation (2.27) including a rectangular signal $f(t)$ with duty cycle $1/2$, *i.e.*, the potential is on for half a period, are shown in Fig. 2.6. Both periodicities—in time (τ) and space (L)—appear distinctly. On the one hand, slip events occur at integer multiples of τ, the period of the signal $f(t)$. On the other hand, the trajectory moves stepwise and noisily by integer multiples of L, the corrugation length of the potential $V(x)$. Both effects lead us to a qualitative explanation of the particle dynamics and how the ratchet effect manifests itself.

Let us suppose that (a) the thermal energy is considerably smaller than the barrier height of the potential, $k_\mathrm{B}T \ll V_0$, and (b) the duration of the off-phase is substantially longer than the relaxation time of the Brownian particle toward the potential minimum, $\tau/2 \gg \eta/\max\{V''(x) \mid x \in [0, L)\}$. Consequently, the probability distribution $P(x,t)$ from Eq. (2.23) is dominated by the drift term. The Brownian particle unavoidably relaxes to a potential

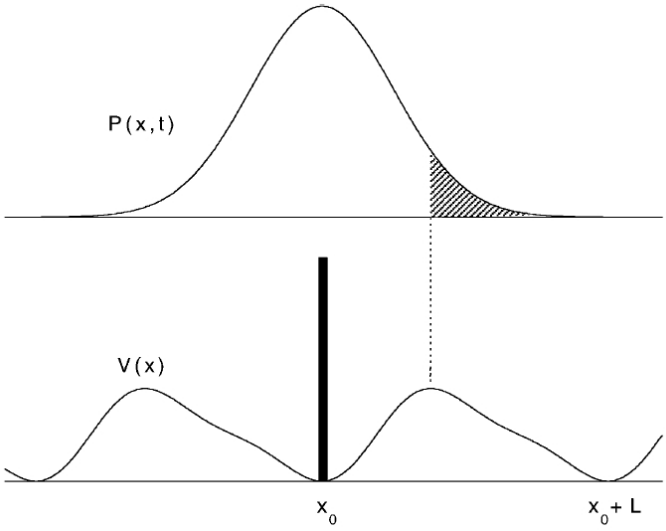

Figure 2.7: A minimal on–off ratchet: as soon as the potential is off, the initial δ like distribution (black bar, bottom) undergoes diffusive motion (top). When the potential is on again, one tail of the broadened distribution (gray area, top) ends up beyond the "short leg" of the ratchet potential (dotted line), thereby generating a net probability current. Taken from [75].

minimum so that $P(x,t)$ becomes stationary according to a Boltzmann distribution, $P^{\mathrm{st}}(x) \propto \exp\left[-V(x)/k_{\mathrm{B}}T\right]$. Due to supposition (a), this stationary distribution will be very narrow and can, on coarser scales, be approximated by a δ-peak, as it is depicted in form of a solid vertical bar at position x_0 in the lower part of Fig. 2.7.

At that moment in time when the signal $f(t)$ turns from 1 to 0, the Brownian particle's dynamics is governed by free diffusion according to Eq. (2.22). Its time evolution is determined by a Green's function $G(x,t|x',t')$ serving as a propagator that connects the probability density $P(x,t)$ with itself at some other time t' via the integral $P(x,t) = \int dx'\, G(x,t|x',t')\, P(x',t')$. The analogous stochastic process is called a *Wiener process* which is the standard mathematical idealization of Brownian motion. The exact form of the propagator is given by a Gaussian function,

$$G(x,t|x',t') = \frac{1}{\sqrt{4\pi\eta k_{\mathrm{B}}T\,(t-t')}}\,\exp\left(-\frac{(x-x')^2}{4\eta k_{\mathrm{B}}T\,(t-t')}\right). \tag{2.28}$$

At the end of the $f(t) = 0$ phase, the resulting distribution $P(x,t)$ is shown in the upper part of Fig. 2.7. It broadened significantly whereas its center, as to be expected, did not move away from x_0.

Pursuant to supposition (a), the motion of the Brownian particle becomes quasi-deterministic after $f(t)$ changed again from 0 to 1 (potential on). Be-

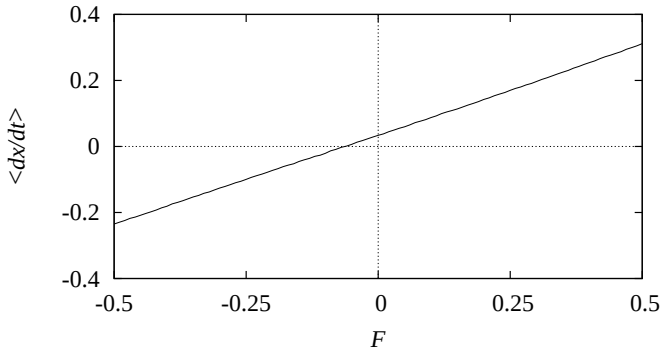

Figure 2.8: Average particle current of the on–off ratchet from Eq. (2.27) depending on the tilt F. All parameter values are the same as in Fig. 2.6.

cause of the spatial asymmetry of the ratchet potential, only one tail of the distribution $P(x,t)$ significantly extends beyond the potential maximum and thus falls into the basin of attraction of the neighboring minimum at $x_0 + L$. Indeed, this is the key mechanism that evokes the ratchet effect. As we have seen, it is a purely statistical effect—there is no way to predict the next transition for the trajectory of a single Brownian particle. But the ensemble average positively reveals a non-vanishing current without external bias.

If we introduce a constant bias F and add it to the right hand side of Eq. (2.27), our minimal model of a Smoluchowski–Feynman ratchet turns into a full-fledged Brownian heat engine. The force–velocity diagram shown in Fig. 2.8 exemplifies (a) the effectiveness of the ratchet effect ($\langle \dot{x} \rangle \neq 0$ for $F = 0$) and (b) a negative mobility for small negative bias ($\langle \dot{x} \rangle > 0$ for $F < 0$). The latter means that thermal energy from the heat bath (*i.e.*, noise) is transformed into utilizable work against an externally applied force. The Brownian particle thus actually climbs "uphill".

Early experimental demonstrations of the on–off ratchet followed immediately. They all used colloidal systems where micro-beads are suspended in a solution. The ratchet potential was more or less exactly adjusted by means of microfabricated electrodes [80] or optical tweezers [81]. Especially the optical tweezer experiments are well suited to provide a quantitative verification of the simple theoretical model. Today, the use of the ratchet effect in microfluidic devices is, besides other geometrical or thermal effects (*e.g.*, absolute negative mobility), considered as state-of-the-art particle separation technique, especially with regard to lab-on-a-chip applications.

3 Interaction-controlled Brownian motion in tilted periodic potentials

The laws of thermodynamics, as empirically determined,
express the approximate and probable behavior of systems
of a great number of particles, or, more precisely,
they express the laws of mechanics for such systems as they appear to beings
who have not the fineness of perception to enable them to appreciate quantities
of the order of magnitude of those which relate to single particles,
and who cannot repeat their experiments often enough
to obtain any but the most probable results.

Josiah Williard Gibbs

3.1 Introduction

Drift and diffusion of a single Brownian particle in a tilted washboard potential is a long-studied problem in non-equilibrium statistical physics. It is of relevance in a number of diverse research areas and belongs to the rare problems which can be solved analytically. As has been stated in subsection 2.1.2, the expression for the velocity in the overdamped limit has been obtained by Stratonovich some fifty years ago [73], while an analytic result for the diffusion coefficient was derived relatively recently [74]. A shorthand summary of the derivation can be found in the preceding chapter.

In many physical situations one deals not with single Brownian particles, but with arrays of a finite number of interacting particles finding themselves in a periodic potential and acted upon by some external force. These arrays comprise different geometries, from linear chains (*e.g.*, the Frenkel–Kontorova model) to complex three-dimensional structures that may even be composed of dissimilar constituents. The problem of coupled Brownian particles

in a periodic structure is important in a large number of fields. Examples include

- friction [18, 19, 67, 82–85]
- diffusion of dimers on surfaces [86–93]
- diffusion of colloidal particles [94–96]
- molecular motors [75, 97–107]
- DNA translocation through a nanopore [108]
- charge density waves [109, 110]
- arrays of Josephson junctions [111, 112]

to name but a few. Many-particle systems may exhibit some features not found in the single-particle counterparts, such as phase transitions, spontaneous ratchet effects, and negative mobility [113].

In the present chapter, we study the behavior of a one-dimensional array of a finite, typically small, number of overdamped Brownian particles in a tilted periodic potential. Our system is closely related to the one investigated in Ref. [93]. The difference of our model from the one considered in that work is that, on the one hand, we restrict ourselves to the case of the overdamped dynamics, while the authors of [93] consider a more general case of arbitrary damping; on the other hand, in Ref. [93], the motion of a pair of interacting particles is studied, whereas we do not impose any restriction on the number of particles in the array.

By numerically solving the underlying equations of motion, as well as by using asymptotic analytic results for the velocity and diffusion coefficient at low and high coupling strength, we report and qualitatively explain new features of the system's dynamics. Namely, we show that both velocity and diffusion coefficient can be maximized with respect to the coupling strength. Furthermore, we find that these characteristics exhibit an interesting multi-peaked dependence on the equilibrium interparticle separation.

Single point contact models (also known as single spring Prandtl–Tomlinson models) for atomic-scale friction can successfully explain many experimental results, but by far not all of them. Especially at the microsecond time domain of the stick–slip dynamics, regarding the so-called fine-structure of jump events, a distinction between the rapid thermal movement of the tip apex within a potential minimum and the relatively more inert bending motion of the cantilever is required [67, 69]. It turns out that an extension to a two-mass–two-spring model is better suited to explain the data consistently.

The extension can easily be carried forward to chains of more than two masses, thereby taking into account the influence of a geometrically extended

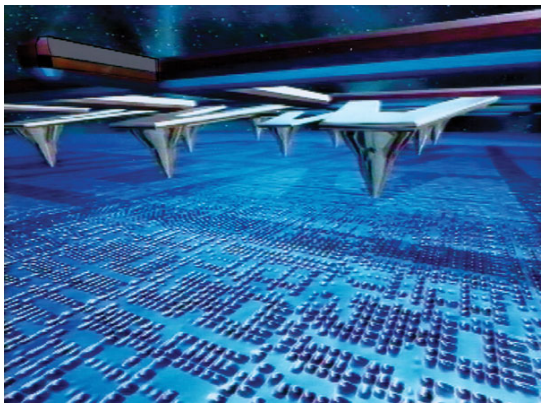

Figure 3.1: An artist's impression of IBM's Millipede, an experimental data storage device consisting of an 64×64 array of AFM cantilevers. The tips work in parallel and can "write" and "read" indentations or manipulate the magnetization of extremely small domains by electric currents. Taken from [114].

contact region. Because very sharp tips still have an apex radius of *ca.* 100 nm, so many elementary bounds actually do participate in the formation of the tip–sample contact that it is very unlikely not to find evidence for a many-particle interaction, tiny as its overall contribution may be.

A prominent example is the vanishing friction usually termed superlubricity, where in fact the many-particle contribution is the decisive one. As Müser pointed out [34], a high degree of non-local correlation is a necessary prerequisite for this extraordinary phenomenon. The experimental access to it has been greatly simplified by Dienwiebel *et al.* [31] and Dietzel *et al.* [33], and we may think of a linear chain of coupled masses in terms of a one-dimensional projection of their sliding graphite flake or antimony island. We assume this projection to be justified because of the sufficiently robust degree of orientation the nano-sliders maintain during the AFM experiments.

Finally, the necessity of a many-particle approximation becomes self-evident if one deals with a multi-asperity tip instead of the usual single-asperity tip or, more drastically, with an array of many AFM tips. The IBM Millipede project currently aims at utilizing microfabricated arrays of cantilevers as a novel storage device that mechanically punch indentations or read them out in parallel similar to the punch cards of early computers, see Fig. 3.1. The mutual influence of the atomic-scale stick–slip motion of each individual tip and the microscopically smooth movement of the whole array is one of the aspects that can ideally be studied with such a multi-asperity device.

In this context, the following considerations of coupled Brownian particles in tilted periodic potentials were performed to understand better how inter-particle cooperation can alter the sliding dynamics with special regard to the velocity (or rather mobility) of the chain.

3.2 Model

We consider an array of N interacting overdamped Brownian particles in a one-dimensional, periodic potential,

$$U(x) = U(x+L)\,, \tag{3.1}$$

tilted by a homogeneous, static force F. The equation of motion for the coordinate x_i of the ith particle is

$$\eta\dot{x}_i(t) = -U'\big(x_i(t)\big) + F - \frac{\partial V\big(x_1(t),\ldots,x_N(t)\big)}{\partial x_i} + \sqrt{2\eta k_\mathrm{B}T}\,\xi_i(t)\,. \tag{3.2}$$

Here, η is the friction coefficient and thermal fluctuations of energy $k_\mathrm{B}T$ are modeled as usual by Gaussian noises $\xi_i(t)$ with

$$\langle\xi_i(t)\rangle = 0\,, \qquad \langle\xi_i(t)\,\xi_j(s)\rangle = \delta_{ij}\,\delta(t-s)\,. \tag{3.3}$$

The meaning of the coordinates x_i depends on the concrete problem at hand. For instance, in the studies [18,19,67,75,82–108] of molecular motors, sliding friction, diffusion of dimers and colloids, and DNA translocation, they represent the physical coordinates of the respective components, such as heads of the molecular motors, surface atoms, colloidal particles, DNA segments, etc. In the models of pinned charge density waves [109, 110], they represent the local phases thereof. Finally, in the arrays of Josephson junctions [111, 112], they stand for the phase differences of the superconducting order parameter between both sides of the barrier.

The interaction potential $V(x_1,\ldots,x_N)$ in (3.2) is assumed to be confining and translation invariant,

$$V(x_1,\ldots,x_N) = V(x_1+b,\ldots,x_N+b)\,, \tag{3.4}$$

$$V(x_1,\ldots,x_N) \to \infty \quad \text{if} \quad |x_i - x_j| \to \infty \tag{3.5}$$

for all real b and all indices $i \neq j$. We furthermore assume that V has a single minimum, such that in the absence of all other forces, the particles are regularly spaced with period a at the positions

$$x_i^{\min} = ia + x - \frac{N+1}{2}\,a\,, \tag{3.6}$$

relatively to their common center of mass

$$x := \frac{1}{N}\sum_{i=1}^{N} x_i\,. \tag{3.7}$$

An example is provided by the all-to-all harmonic coupling

$$V(\{x_i\}) = \frac{\kappa}{2} \sum_{i=1}^{N} \left(x_i - x_i^{\min} \right)^2 , \tag{3.8}$$

where $x_i^{\min}$ is related to the center of mass via Eq. (3.6). Physically, this interaction may thus be viewed e.g. as emerging due to a rigid (but massless) "backbone", to which the "particles" x_i are attached via springs at regular distances a. Such systems quite naturally arise e.g. in the context of molecular motors [75,97,99,106] and atomic friction [18,19,67,83–85].

Our goal is to find the average velocity and diffusion coefficient of the center of mass (3.7) of the N-particle system (3.2),

$$v := \lim_{t\to\infty} \frac{\langle x(t) \rangle}{t} , \qquad D := \lim_{t\to\infty} \frac{\langle x^2(t) \rangle - \langle x(t) \rangle^2}{2t} , \tag{3.9}$$

and, in particular, their dependence upon the most important system parameters.

Unlike the majority of previous related works, we assume free rather than periodic boundary conditions and, most importantly, our main focus will not be on the large-N limit but rather on quite small particle numbers.

Due to the internal degrees of freedom of the many-particle system (3.2), this problem is considerably more complex than the single-particle counterpart. Therefore, an analytical treatment will be possible only in the situations when the many-particle problem can be approximately reduced to a single-particle one, namely for asymptotically weak and strong coupling. These analytical results will be derived in the next section. In Sect. IV, we will present the results of our numerical simulations of Eq. (3.2), as well as of the analytic approximations, to demonstrate and discuss some interesting peculiarities of the diffusion of the many-particle system.

3.3 Analytical Results

For a single, overdamped Brownian particle in a tilted periodic potential ($N = 1$ in Eqs. (3.2)-(3.7)) the mean velocity from (3.9) is given by the exact analytical formula [73,75]:

$$v_1(\{u_n\}, T) = \frac{1 - e^{-FL/k_B T}}{\int_{x_0}^{x_0+L} \frac{dx}{L}\, I_{\pm}(x)} , \tag{3.10}$$

for any choice of the reference point x_0 and of the indices $\pm$ in

$$I_{\pm}(x) := \frac{k_B T}{\eta} \int_0^L dz \, \exp\left(\pm \frac{U(x) - U(x \mp z) - F(x - z)}{k_B T} \right) . \tag{3.11}$$

The subscript 1 in Eq. (3.10) indicates that the result applies to a single particle and, for later convenience, we have explicitly indicated its dependence on temperature T and the Fourier components u_n of the periodic potential:

$$U(x) = \sum_{n=-\infty}^{\infty} u_n e^{inqx}, \qquad u_{-n} = u_n^*, \qquad q := \frac{2\pi}{L}. \tag{3.12}$$

Likewise, the single-particle diffusion coefficient from Eq. (3.9) is given by the exact analytical formula [75]

$$D_1(\{u_n\}, T) = \frac{k_B T}{\eta} \frac{\int_{x_0}^{x_0+L} \frac{dx}{L} I_\pm(x)\, I_+(x)\, I_-(x)}{\left(\int_{x_0}^{x_0+L} \frac{dx}{L} I_\pm(x)\right)^3}. \tag{3.13}$$

3.3.1 Weak-coupling limit

In the absence of the interaction potential W in (3.2), the N individual particles are statistically independent of each other and thus the correlation is separable, $\langle x_i(t) x_j(t)\rangle = \langle x_i(t)\rangle\langle x_j(t)\rangle$, for all $i \neq j$ and all times t. Exploiting this fact after introducing Eq. (3.7) into (3.9) readily yields the following result for the velocity and diffusion coefficient of the center of mass:

$$v = v_1(\{u_n\}, T), \qquad D = \frac{D_1(\{u_n\}, T)}{N}. \tag{3.14}$$

Turning to asymptotically weak but finite interactions, it is intuitively quite plausible that the concomitant modifications of velocity and diffusion of the center of mass will also be asymptotically small. Formally, this means that the limits of vanishing interaction in (3.2) and of large times in (3.9) commute. In other words, we expect the results (3.14) to remain approximately valid for sufficiently weak interaction potentials V. While we have no rigorous proof of this conjecture, it is in full agreement with our extensive numerical explorations.

3.3.2 Strong-coupling limit

For asymptotically strong coupling, the individual particles maintain fixed positions with respects to their common center of mass, namely $x_i^{\min}$ from Eq. (3.6). Hence we expect that the center of mass behaves like one single, "big" Brownian particle with some appropriately renormalized potential and thermal noise.

To work out this program, it is convenient to change to the shifted particle coordinates

$$\tilde{x}_i := x_i - ia \tag{3.15}$$

and their corresponding center of mass

$$\tilde{x} := \frac{1}{N} \sum_{i=1}^{N} \tilde{x}_i = x - \frac{N+1}{2}\, a\,, \tag{3.16}$$

where the last equality follows from (3.7) and (3.15). In the new coordinates, the equations of motion (3.2) assume the form

$$\eta \dot{\tilde{x}}_i(t) = -U'\big(\tilde{x}_i(t) + ia\big) + F - \frac{\partial V\big(\{\tilde{x}_j(t) + ja\}\big)}{\partial \tilde{x}_i} + \sqrt{2\eta k_{\mathrm{B}} T}\, \xi_i(t)\,. \tag{3.17}$$

Next, we sum over all i and divide by N, yielding $\eta \dot{\tilde{x}}$ on the left-hand side. On the right-hand side, the sum over the interaction terms vanishes, as follows by differentiating (3.4) with respect to b. The last arithmetic average of the N independent, delta-correlated Gaussian noises $\xi_i(t)$ results in $N^{-1/2}$ times a single, delta-correlated Gaussian noise $\xi(t)$. Specifically for asymptotically strong coupling it follows from $x_i = x_i^{\min}$ (see above) together with (3.6), (3.15), and (3.16) that $\tilde{x}_i = \tilde{x}$. All in all, we thus find in the strong coupling limit that

$$\eta \dot{\tilde{x}}(t) = -\tilde{U}\big(\tilde{x}(t)\big) + F + \sqrt{\frac{2\eta k_{\mathrm{B}} T}{N}}\, \xi(t)\,, \tag{3.18}$$

with an effective potential

$$\tilde{U}(x) := \frac{1}{N} \sum_{i=1}^{N} U(x + ia) \tag{3.19}$$

whose Fourier components are related to those of the bare potential in (3.12) via

$$\tilde{U}(x) = \sum_{n=-\infty}^{\infty} \tilde{u}_n\, e^{inqx}\,, \tag{3.20}$$

$$\tilde{u}_n = u_n\, \frac{e^{inqa}}{N}\, \frac{1 - e^{iqnNa}}{1 - e^{inqa}}\,. \tag{3.21}$$

In view of (3.16) one readily sees that the resulting drift and diffusion for $\tilde{x}$ will be the same as those for x from (3.9). Since (3.18) represents an effective single-particle dynamics for $\tilde{x}$, we can employ (3.10) and (3.13) to infer for the velocity and the diffusion coefficient in the strong-coupling limit:

$$v = v_1\left(\{\tilde{u}_n\}, \frac{k_{\mathrm{B}} T}{N}\right), \qquad D = D_1\left(\{\tilde{u}_n\}, \frac{k_{\mathrm{B}} T}{N}\right). \tag{3.22}$$

These expressions become exact for rigidly coupled particles. For large but finite coupling strengths, one can approximately account for the resulting

small but fast fluctuations of the individual particle positions around their accompanying "strong coupling equilibria" by integrating over those fluctuations [87]. We do not present the respective formulae, as we have found that all interesting effects are already captured by our leading order expressions (3.22).

3.3.3 Symmetries

Focusing on the specific interaction potential from (3.8), the equations of motion (3.17) for the shifted particle coordinates (3.15) can be rewritten (for arbitrary κ) in the form

$$\eta\dot{\tilde{x}}_i = -U'(\tilde{x}_i + ia) + F - \kappa\,(\tilde{x}_i - \tilde{x}) + \sqrt{2\eta k_\mathrm{B}T}\,\xi_i(t)\,. \tag{3.23}$$

It follows that velocity and diffusion coefficient remain unchanged if the equilibrium interparticle distance, a, is increased by an integer multiple of the lattice constant L of the potential: $v(a+kL) = v(a)$, $D(a+kL) = D(a)$. Furthermore, changing a to $-a$ is equivalent to renumbering the particles in the reverse order, again leaving the physical properties, such as v and D, unchanged. This implies the following symmetry property of the quantities of interest:

$$v(kL \pm a) = v(a)\,, \qquad D(kL \pm a) = D(a) \tag{3.24}$$

for any integer k.

We remark that the symmetry property (3.24) is valid for interactions (3.23) of arbitrary strength κ. Moreover, the periodic potential $U(x)$ may be arbitrary, and, in particular, does not need to be spatially symmetric.

3.4 Numerical results

To evaluate the velocity and the diffusion coefficient from numerical simulation of Eq. (3.2), direct application of the definition (3.9) is somewhat inconvenient. This is so because, in general, the numerical effort to reach good convergence is quite high and, in particular, the time necessary for convergence of the quantities $\langle x(t)\rangle/t$ and $\left(\langle x^2(t)\rangle - \langle x(t)\rangle^2\right)/2t$ is different for differently chosen parameter values. Therefore, we have employed an alternative numerical procedure based on the relations from [75] between v and D and the first two moments of the time necessary for the center of mass to cover the distance kL, where k is an integer:

$$v = \frac{kL}{\langle t\,(x_0 \to x_0 + kL)\rangle}$$

and

$$D = \frac{(kL)^2}{2} \frac{\langle t^2 (x_0 \to x_0 + kL)\rangle - \langle t (x_0 \to x_0 + kL)\rangle^2}{\langle t (x_0 \to x_0 + kL)\rangle^3}. \tag{3.25}$$

These relations are strictly valid if the transitions by the distance kL are statistically independent events [75]; in other words, information about the state of the system before the transition is lost after the transition. This is the case for one-particle systems for any value of k; hence, for a single particle, one can take its smallest value, $k = 1$. For the system consisting of several Brownian particles, this is not the case, because the system has "memory" in the form of the internal degrees of freedom, making the consecutive transitions not statistically independent. Therefore, additional care should be taken to make sure that this is a negligible effect. Numerical application of the formula above yielded identical (within statistical error) results for v and D for $k = 1$ and $k = 2$ for all parameter values tested. This means that such memory effects are indeed negligible, and one can apply the relation above, taking $k = 1$. For each data point, the results were based on at least 1 000 transitions by L.

For simplicity, we focus on the specific potential

$$U(x) = \frac{\Delta U}{2} \cos \frac{2\pi x}{L} \tag{3.26}$$

with fixed corrugation depth $\Delta U = 10 k_B T$ and unit periodicity, $L = 1$. In terms of the Fourier expansion from (3.12), the only non-zero Fourier components are thus $u_1 = u_{-1} = \Delta U/4$. Both the thermal energy $k_B T$ and the friction coefficient η are also set to unity. Furthermore, we use the all-to-all harmonic coupling from (3.23).

3.4.1 Dependence on the tilt

Fig. 3.2 shows the dependence of velocity and diffusion coefficient on the bias for the asymptotic cases considered in Sect. 3.3, see Eqs. (3.14) and (3.22), and for the intermediate cases $\kappa = 100$ and $\kappa = 200$. Depicted are results for the dimer ($N = 2$), while other values of N (not shown) produced similar curves.

For all values of the coupling constant, two regimes can be distinguished. At high value of the bias F, the spatial modulation of the potential is negligible. In this regime, the velocity asymptotically approaches F/η and the diffusion coefficient converges towards $k_B T/(\eta N)$. In the opposite regime of small bias F, the dynamics is governed by thermally activated transitions between local potential wells, leading for both the velocity and the diffusion to very small values with an approximately Arrhenius-type, exponential in-

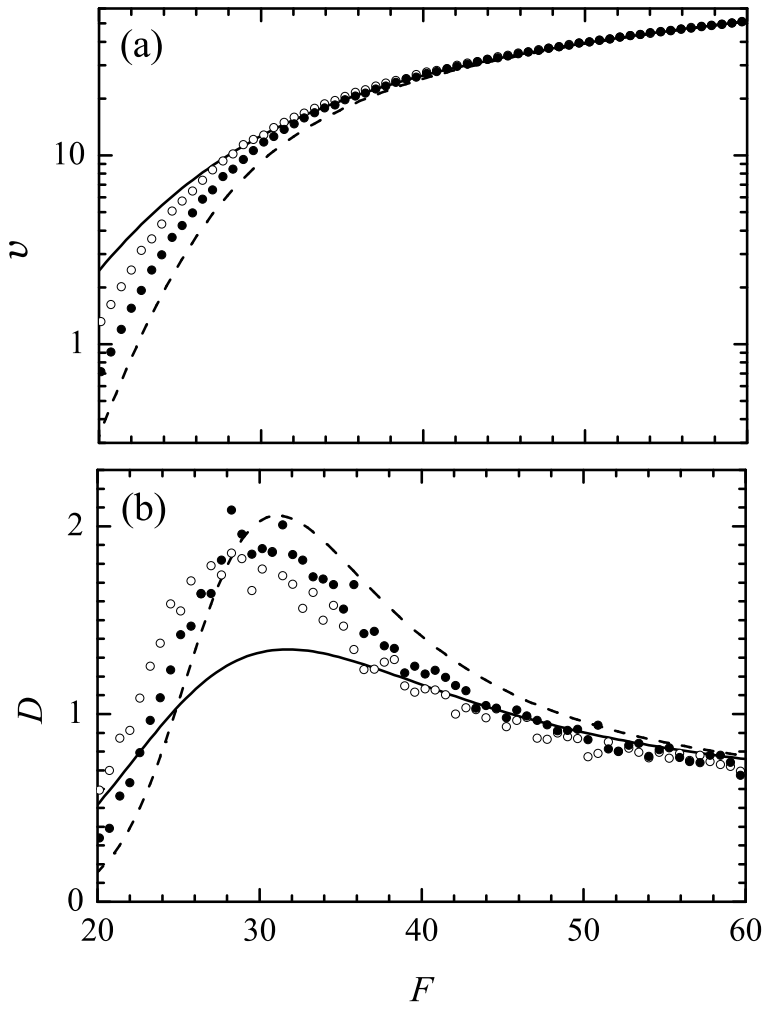

Figure 3.2: Velocity and diffusion coefficient (3.9) *vs*. tilt F for a dimer ($N = 2$), satisfying (3.2) with (3.8), (3.26), $\eta = k_B T = L = 1$, $\Delta U = 10$, vanishing equilibrium interparticle separation ($a = 0$), and different values of the coupling constant κ. According to (3.27), the critical tilt is $F_{\text{crit}} = 31.4\ldots$. Dashed lines: Analytical results (3.14) for asymptotically small κ. Solid lines: Analytical results (3.22) for asymptotically large κ. Filled and empty circles: Numerical results for $\kappa = 100$ and $\kappa = 200$, respectively. The numerical uncertainty is quantified by the small erratic deviations from a smooth behavior. For still smaller and larger κ-values (not shown), the numerically obtained results approach the respective analytical asymptotics.

crease with F. These two regimes are separated by the critical bias

$$F_{\text{crit}} = \frac{\pi \Delta U}{L}, \tag{3.27}$$

at which the barriers of the tilted periodic potential just disappear, degenerating into flat regions.

At $F \approx F_{\text{crit}}$, the diffusion coefficient exhibits a maximum. This maximum can be understood as follows. Instead of a single system, let us consider an ensemble of many non-interacting replicas of the system. If the tilt exceeds the value F_{crit}, all members of the ensemble are sliding down with approximately the same velocity around F/η. On the other hand, for F-values much smaller than F_{crit}, most of the members are trapped in the potential minima, with only a small fraction performing a thermally activated interwell jump at each moment of time. But in the critically tilted case, a notable part of the replicas will remain in the flat regions of the potential and have zero velocity (up to small thermal fluctuations) while the others will perform a downhill motion with a large velocity. This means that the spreading of the ensemble will proceed faster than in the overcritically tilted regime, when all the replicas are in the running state, and also faster than in the subcritical case, when the interwell transitions are rare events.

Conversely, if one considers velocity and diffusion coefficient as functions of the barrier height ΔU (or, equivalently, the value of F_{crit}) at a fixed nonzero F-value, then the former will be a decreasing function of the potential amplitude with a maximum $v_{\max} = F/\eta$ at $\Delta U = 0$, and the latter will exhibit a non-monotonic behavior. Namely, the diffusion coefficient will grow with ΔU until the corresponding critical force F_{crit} from Eq. (3.27) will reach the value of the tilt F, and then start to decrease upon further increase of the potential amplitude in the regime of subcritical tilt.

3.4.2 Dependence on the coupling strength

So far our discussion has been mainly focused on the situation when the many-particle array could be described as an effective one-particle system with properly renormalized potential and temperature. Yet, finite-coupling strengths are expected to lead to additional interesting effects which are captured neither by the weak- (3.14) nor strong-coupling (3.22) asymptotics.

To study these effects, we now turn to the dependence of the velocity and diffusion coefficient on the coupling strength. Fig. 3.3 illustrates the results of numerical simulation of Eq. (3.2). As before, we focus on the case of a dimer, $N = 2$, since the results for more particles were qualitatively the same.

Fig. 3.3 shows the velocity and diffusion coefficient for a dimer in the potential with the same parameters as before, tilted with the force $F = 22 \approx$

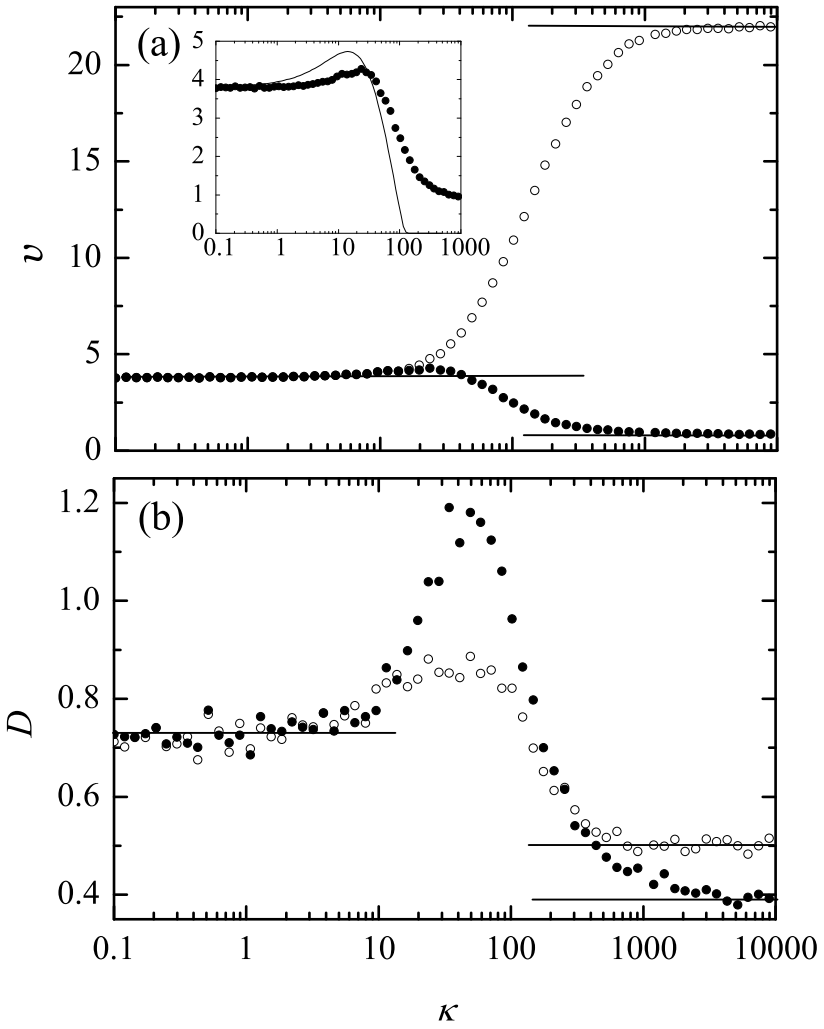

Figure 3.3: Velocity and diffusion coefficient *vs.* coupling constant κ for the same system as in Fig. 3.2 with a fixed tilt $F = 22$ and a dimer rest length of $a = 0$ (filled circles) and $a = L/2$ (empty circles). Horizontal lines correspond to the analytical results for asymptotically small and large κ from (3.14) and (3.22), respectively. The inset in (a) shows the velocity for $a = 0$ together with the results of the analytic approximation (3.29).

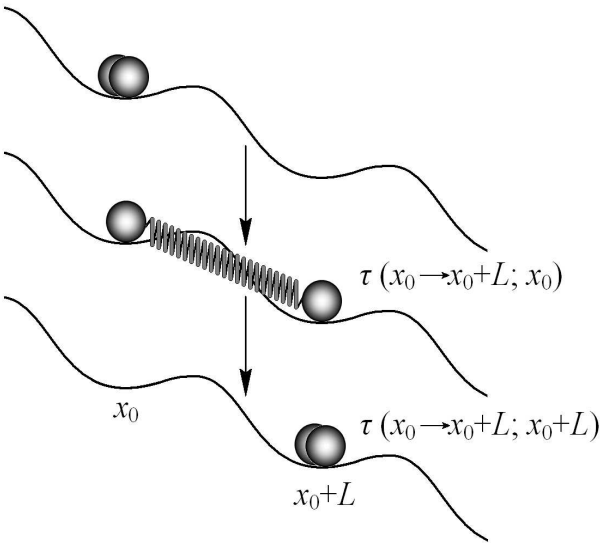

Figure 3.4: Model of dimer motion in a tilted periodic potential.

$0.7F_{\text{crit}}$. The two sets of curves correspond to the dimer rest length $a = 0$ (filled circles) and $a = L/2$ (open circles).

For small coupling constant κ, the diffusion properties of the dimer practically do not depend on the rest length and are given by Eq. (3.14). At large κ, on the other hand, the system behaves as a single Brownian particle in the effective potential (3.19), whose modulation depth equals 0 for $a = L/2$. Therefore, the velocity of the dimer with the rest length $a = L/2$ increases monotonically from the single-particle value given by Eq. (3.14) to the value F/η. On the other hand, for $a = 0$, the amplitude of the effective potential is the same as in the non-interacting case, i.e. ΔU, but the effective temperature in (3.18) is twice as small. Therefore, the probability of the interwell transitions become exponentially suppressed due to the Arrhenius factor, and the velocity drops from the same initial value to a smaller value.

Interestingly, in between the two extremes, the velocity of the dimer of zero rest length as a function of the coupling strength develops a maximum at some intermediate κ-value comparable to the second derivative of the host potential at a minimum, see the inset in Fig. 3.3(a). This behavior is reminiscent to the results reported in Ref. [100], although the underlying physical mechanism is quite different. The nature of this non-monotonicity is the correlated character of the jumps of the two dimer components between the minima of the tilted periodic potential. We propose that the following simplified picture captures the main qualitative features of the effect.

The motion essentially proceeds in steps as shown in Fig. 3.4. For a small

but finite κ, the "downhill" transition of the dimer consists of two stages. In the first stage, the system finds itself in the "ground state", where both components are found within one of the minima, x_0, of the tilted periodic potential $U(x) - Fx$. At some point, one of the particles, the "leader", performs a thermally activated transition into the next minimum, while the second particle, the "follower", remains in the previous potential well. The characteristic time for this process can be estimated as the mean first passage time $\tau(x_i \to x_f; z)$ for one particle to go from the initial position x_i to the final position $x_f > x_i$, provided that the other particle is at a fixed position z:

$$\tau(x_i \to x_f; z) = \frac{\eta}{k_B T} \int_{x_i}^{x_f} dx \, \exp\left(\frac{U(x) - Fx + \frac{\kappa}{2}(x-z)^2}{k_B T} \right) \times \int_{-\infty}^{x} dy \, \exp\left(-\frac{U(y) - Fy + \frac{\kappa}{2}(y-z)^2}{k_B T} \right). \quad (3.28)$$

The average time of entrance from the "ground state" to the "first excited state" in Fig. 3.4 is approximately $\tau(x_0 \to x_0 + L; x_0)$. Similarly, the transition of the "follower" into the next potential well takes approximately a duration $\tau(x_0 \to x_0 + L; x_0 + L)$. The resulting velocity is approximately the inverse average time to cover one spatial period L:

$$v = \frac{2L}{\tau(x_0 \to x_0 + L; x_0) + \tau(x_0 \to x_0 + L; x_0 + L)}, \quad (3.29)$$

where the factor 2 in the numerator accounts for the fact that any of the two particles can assume the role of the leader.

The formula (3.29) is rather crude, as it does not capture many important features. In particular, it assumes that one of the particles remains stationary during the second particle's transition into the next minimum. Furthermore, it approximates the true positions of the particles in different potential wells with the respective minima of the tilted periodic potential. Finally, this approach neglects the possibility of multiple transitions performed by either particle.

Despite all these approximations, Eq. (3.29) still reproduces qualitatively correctly the behavior of velocity with the coupling constant, in particular, the fact that v is maximized at some κ-value, see Fig. 3.3. Accordingly, we can understand this maximum as resulting from the competition between two effects: on the one hand, the presence of the follower hinders the transition of the leader into the next potential well, increasing $\tau(x_0 \to x_0 + L; x_0)$; on the other hand, once the leader makes such a transition into the next well, it is easier for the follower to get there, thus reducing the second contribution to the total time, $\tau(x_0 \to x_0 + L; x_0 + L)$.

It is interesting to observe that the diffusion coefficient is also maximized at the coupling strength of the order of the second derivative of the tilted periodic potential at a minimum. Similar to the diffusion enhancement with respect to the tilt (see Sect. 3.4.1), the diffusion maximum marks the boundary between the two modes of the dimer motion characterized by substantially different velocities – the uncorrelated jumps realized at weak coupling and completely correlated motion at large κ. At the intermediate coupling constants, both modes can be realized, meaning that in a large ensemble of the non-interacting system replicas, there will be a large spreading of velocities, resulting in the enhanced diffusion coefficient.

3.4.3 Dependence on the interparticle separation

If the strength of coupling between the constituents is weak, the effect of the equilibrium interparticle separation, a, on the diffusion properties is insignificant, cf. Sect. 3.4.1 and Fig. 3.5. Therefore, we will only consider the case of rigid coupling; for finite but still strong coupling between the particles, we numerically verified (not shown) that the main qualitative features discussed below are preserved.

In view of the symmetry property (3.24), we will focus on $a \in [0, L]$. Due to the invariance under $a \mapsto L - a$ it is in principle even sufficient to consider $a \in [0, L/2]$, but for the sake of better visualization of the essential features, the full range $a \in [0, L]$ will be plotted and discussed.

Fig. 3.5 shows the velocity (a) and the diffusion coefficient (b) for a system of $N = 5$ rigidly coupled Brownian particles as a function of a for several different tilt values. It is clear from Fig. 3.5(a) that the velocity as a function of a has four peaks, and these peaks become less and less pronounced as the tilt F is increased. With respect to the diffusion coefficient, it exhibits a more complicated multipeaked structure, Fig. 3.5(b): not only the positions and heights of the diffusion peaks, but also their number depend on the value of the applied tilt.

To understand this behavior, it is instructive to consider how the critical force corresponding to the effective periodic potential (3.20) depends on the interparticle separation a. It follows from Eqs. (3.20), (3.21) and (3.27) that the effective critical force is proportional to the amplitude $|\tilde{u}_1|$ of the effective potential:

$$\tilde{F}_{\mathrm{crit}} = \frac{4\pi}{L}\ |\tilde{u}_1| = \frac{\pi \Delta U}{NL}\ \left| \frac{\sin \pi N a/L}{\sin \pi a/L} \right|. \tag{3.30}$$

This dependence is shown in Fig. 3.5(c). The amplitude of the effective potential vanishes at $N-1$ values of $a = kL/N$, $k = 1, 2, \ldots, N-1$. Since the velocity of the system decreases with $\tilde{F}_{\mathrm{crit}} \propto |\tilde{u}_1|$ and attains the largest value $v_{\max} = F/\eta$ when $|\tilde{u}_1| = 0$, to each zero of $\tilde{F}_{\mathrm{crit}}$ there corresponds a velocity

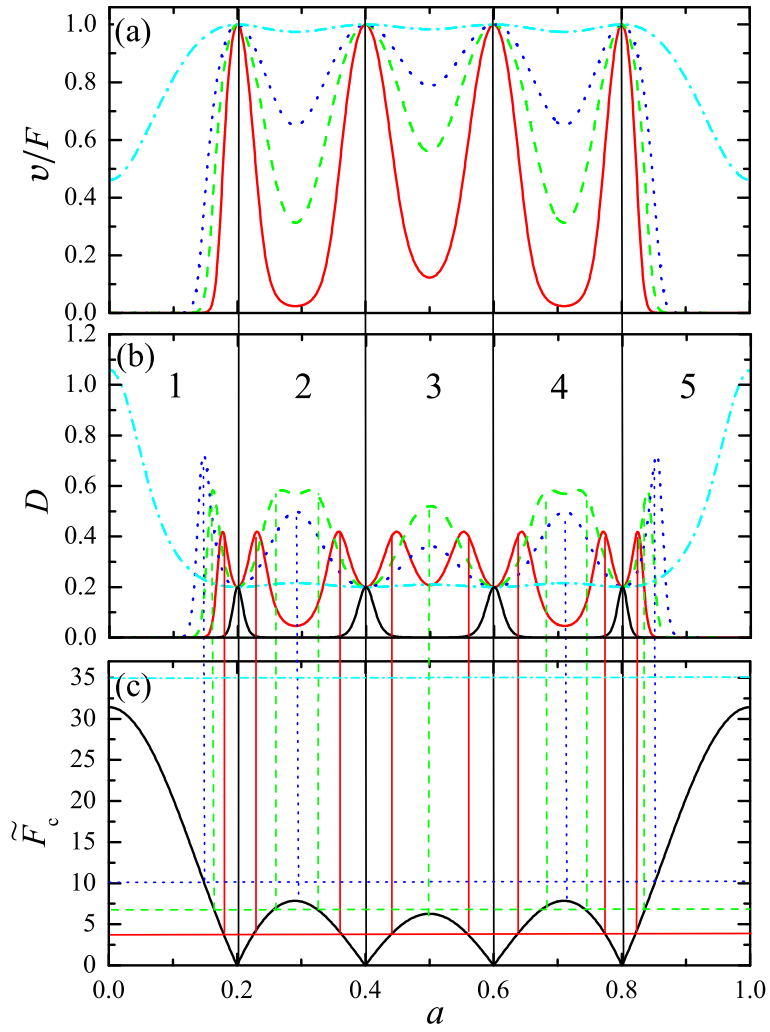

Figure 3.5: (a) Mobility, v/F, and (b) diffusion coefficient D from (3.22) for a system of $N = 5$ rigidly coupled Brownian particles *vs.* equilibrium interparticle separation a at different values of the tilt F. Solid red line: $F = 4$; dashed green line: $F = 7$; dotted blue line: $F = 10$; dash-dotted cyan line: $F = 35$. In (b), the solid black curve corresponds to the diffusion coefficient at zero tilt, $F = 0$. All other parameter values are the same as in Fig. 3.2. (c): The critical force (3.30) corresponding to the effective potential (3.19). The four horizontal lines correspond to the above specified four values of the applied bias F.

maximum, and at each maximum of $\tilde{F}_{\text{crit}}$ the velocity is minimized. For a system consisting of N particles, we therefore expect $N-1$ velocity maxima located at $a = kL/N$, $k = 1, \ldots, N-1$.

For convenience of further discussion, we divide the whole domain of $a \in [0, L]$ into N equal regions of size L/N, with the kth region being defined as $[(k-1)L/N, kL/N]$, $k = 1, \ldots, N$. For the special case $N = 5$, these regions are marked with numbers in Fig. 3.5(b). In each such region, the dependence of $\tilde{F}_{\text{crit}}$ on a has a single maximum. This maximum is located approximately in the "middle" of the regions with numbers $2, \ldots, N-1$, while in the first and the last region, the maxima coincide with the region boundaries, see Fig. 3.5(c). The heights of the $\tilde{F}_{\text{crit}}$-maxima in different regions, in general, are different.

At zero tilt value, $F = 0$, the diffusion coefficient is maximized at exactly the same $N-1$ values of the interparticle separation as the velocity, i.e. at $a/L = 1/N, \ldots, (N-1)/N$, where $D = k_{\text{B}}T/(\eta N)$. For other values of a, the untilted periodic potential possesses barriers hindering the diffusive motion of the system. The dependence of D on a at zero tilt is shown in Fig. 3.5(b) as a solid black line.

For a small but finite value of the applied bias $F > 0$, each of these maxima splits into two peaks. To understand this behavior, we note that for a small but finite bias, depending on the value of a, the system can be tilted either overcritically, or subcritically. The former situation is realized at those values of the interparticle separation a, for which $\tilde{F}_{\text{crit}}(a) < F$, and the latter for $\tilde{F}_{\text{crit}}(a) > F$. At each value of a where the effective critical force approximately equals the applied bias,

$$\tilde{F}_{\text{crit}}(a) = F\,, \tag{3.31}$$

the system finds itself in a critically tilted potential, where the diffusion coefficient is maximized, see the discussion in the end of Sect. 3.4.1. It is impossible to find the solution of Eq. (3.31) analytically for an arbitrary N, but graphically, the solution corresponds to the intersection of the curve $\tilde{F}_{\text{crit}}(a)$ with the straight line at the level of the tilt F, see Fig. 3.5(c).

At small tilt values, we have $2(N-1)$ solutions of the equation (3.31) in the domain $0 \le a \le L$, with 2 solutions in the $N-2$ middle regions, and 1 solution in each of the end regions with numbers 1 and N. Correspondingly, we have $2(N-1)$ maxima of the diffusion coefficient. In our numerical example, this situation is realized at $F = 4$ (solid red line) in Fig. 3.5(b).

The N maxima of $\tilde{F}_{\text{crit}}$ *vs.* a in Fig. 3.5(c) are not of the same height: the one in the region 3 is somewhat smaller than those in regions 2 and 4, and the maxima in the end regions 1 and 5 are the largest. This means that for a tilt value slightly exceeding the maximal $\tilde{F}_{\text{crit}}$ in region 3, but smaller than the maximal critical tilt in all other regions, the system is supercritically tilted in

the third region at all values of a, whereas in other regions, it can be tilted either super- or subcritically, depending on a. Correspondingly, the two diffusion maxima in region 3 merge into a single one located at that value of a, at which $\tilde{F}_{\mathrm{crit}}$ is the largest. In regions 2 and 4, the diffusion coefficient still has two maxima, approximately corresponding to the two solutions of Eq. (3.31) in those regions. This situation is realized at $F = 7$ (dashed green line) in Fig. 3.5(b).

Upon further increase of the applied force F we enter the regime, in which the system is overcritically tilted everywhere but in the end regions. Then, in the middle regions $2, \ldots, N-1$, we have a single diffusion peak, whose height gets smaller and smaller upon increasing the tilt. This situation is realized at $F = 10$ and shown as a blue dotted line in Fig. 3.5(b). Only in the end regions 1 and N does Eq. (3.31) have a solution at a non-zero value of a, resulting in a diffusion maximum around that value.

Finally, at very large bias, Eq. (3.31) does not have a solution in any a-region and remains overcritically tilted for all values of a. The diffusion coefficient in this case has N rather small maxima, corresponding to N maxima of $\tilde{F}_{\mathrm{crit}}$ in each region (see Fig. 3.5(b), dash-dotted cyan line corresponding to $F = 35$). These maxima become less and less pronounced as F increases.

For $N > 5$ one recovers analogous scenarios with essentially the same main features, while for $N < 5$ some important features are missing.

3.5 Concluding remarks

We have investigated the behavior of N coupled, overdamped Brownian particles in a tilted periodic potential both analytically and numerically. Analytic results for the center of mass velocity and diffusion coefficient have been obtained in the asymptotic limits of weak and strong coupling by way of reducing the many-particle problem to an effective single-particle dynamics with renormalized temperature and periodic potential.

The dependence of the transport properties of the many-particle system on the tilt does not differ qualitatively from the single-particle case. At the same time, when viewed as functions of the coupling parameters, the velocity and diffusion coefficient exhibit several interesting peculiarities. Due to the enhanced synchronization of the interwell transitions of the individual particles, both velocity and diffusion coefficient can be maximized with respect to the coupling strength.

Furthermore, for sufficiently large coupling strengths, the velocity as a function of the equilibrium interparticle separation of an N-particle system exhibits $N-1$ maxima, while the number of maxima of the diffusion coefficient, as well as their positions and heights depend on the applied tilt. More precisely, there are $N-1$ diffusion maxima for zero tilt, while for small but

finite tilt value, each of these maxima splits into two, resulting in $2(N-1)$ diffusion peaks. Further increase of tilt leads to sequential merging of the $N-2$ adjacent peak pairs, so that for sufficiently large bias, the number of diffusion peaks is N.

The relation to friction

The most obvious conclusion with regard to atomic-scale friction experiments can be found from the results in Fig. 3.3(a). Namely, the large spread in the chain mobility depending on the rest length of the dimer. For a strongly coupled chain, a rest length that is commensurate to the period of the surface potential causes a low mobility, whereas incommensurability (*e.g.*, $a = L/2$) boosts the mobility of the chain due to interparticle cooperation. The extension to a chain consisting of five atoms leads to the same qualitative result, see Fig. 3.5(a). The mobility is peaked for a dimer length a equal to integer multiples of $L/5$ except when a/L is an integer (commensurate).

This kind of cooperative behavior is the salient feature of any many-particle model because it provides one or more additional *internal* degrees of freedom that do not exist in the single-particle dynamics. Internal degrees of freedom can act very differently. On the one hand, they can act as an energy storage that enhances the overall performance of the chain (mobility) by redistributing large amounts of the potential energy that otherwise would be dissipated. On the other hand, they can open secondary paths of dissipation or increase the impact of the primary paths of dissipation as one can see in the case of commensurate a and L. The fundamental influence internal degrees of freedom have on the dynamics of the smallest many-particle system, a dimer, will be examined in greater detail in the following two chapters.

With regard to experimental results concerning the superlubricity of a nanoparticle on a crystalline surface, the orientational dependence is a well known fact [31]. The disappearance of a measurable amount of friction can be controlled by the relative angle between crystal lattice and graphite probe, resulting in different degrees of (in-)commensurability. A new feature that, as far as we know, has not yet been taken into consideration is the waiting time dispersion of the many-particle stick–slip movement of such a nano slider. Today, recording the average ("center of mass") position of the sliding probe with sub-micro second precision is no difficulty at all. Therefore, a statistical analysis of the torsional deflection should at least qualitatively reveal a similar peaked structure of the waiting time dispersion as for the diffusion in Fig. 3.5(b), depending on the ratio $a/L^{\mathrm{eff}}(\phi)$. Here, $L^{\mathrm{eff}}(\phi)$ is the effective distance between potential minima of the substrate as experienced by a probe pulled along a one-dimensional path with an angle ϕ to a principal axis.

In principle, the waiting time dispersion can be extracted from the autocorrelation function of the cantilever's torsional motion. May $x(t)$ be the trajectory, v the average pulling velocity and $L^{\mathrm{eff}}(\phi)$ the effective lattice spac-

ing under the angle ϕ. Then, the auto-correlation function is given by $c(\tau) = \langle x(t)x(t+\tau)\rangle$. The signature of the jump events should show up as a peak at

$$\tau_0 \approx L^{\mathrm{eff}}(\phi)/v\,. \tag{3.32}$$

The waiting time dispersion ΔT_2, being related to the diffusion coefficient of free Brownian motion in tilted periodic potentials via Eq. (2.14), translates directly into $\Delta\tau_2$, the width of the peak around τ_0. A close inspection of the dependence of $\Delta\tau_2$ on the angle ϕ via the effective lattice constant $L^{\mathrm{eff}}(\phi)$ thus may indicate whether the orientational variation of measured atomic friction is due to the kind of interaction-controlled Brownian motion as described in this chapter.

4 Ratchet effect of a dimer I The case of asymmetric surface binding

Nessuno effetto è in natura senza ragione;
intendi la ragione e non ti bisogna sperienza.

Leonardo da Vinci

4.1 Introduction

Theoretical studies of coupled Brownian particles in periodic structures is of great importance in many research areas, such as friction [18, 19, 67, 82–85], molecular motors [97], adsorbed atoms [88, 115], polymers [116], ferrofluids [117], colloids [94], to name but a few. It is known that in the absence of thermodynamic equilibrium and under broken inversion symmetry of the periodic structure, such systems are able to exhibit the so-called ratchet effect (see section 2.2 and [75] for a review), that is, spontaneous transport in the absence of any external bias.

Within this and the following chapter, we study the system where the periodic potential does possess inversion symmetry. Our interest to this problem is motivated by the fact that this is the case in many experimental situations, such as diffusion of a dimer on the surface. A further motivation is that, based on the experimental studies [118], it has been suggested that the mechanism responsible for the symmetry breaking in molecular motors may be related to their own internal structure rather than their environment. That is, one can achieve symmetry breaking by making use of the internal degree of freedom (DOF) by either periodically modulating the interaction parameters of the Brownian particles [119], or by applying different forcings to different components of the dimer [120].

We note that the ratchet effect is possible in a symmetric structure also when there is no internal DOF, but the heights of different potential barriers are modulated individually at different frequencies [121]. However, experimentally, such a symmetry breaking due to individual modulation of the energy barriers or dimer components may be more difficult to realize than to globally modulate the potential properties for all components.

In this chapter, we introduce a simple model, where the transport occurs in a system of interacting Brownian particles. In contrast to the previous studies of coupled Brownian motors [100–103, 105, 122, 123], we consider the case where the flashing potential has inversion symmetry at all times. The essential feature of our model is that different components of the system feel the potentials of the same shape but different amplitudes. Experimentally, this can be realized, *e.g.*, in the system of two dissimilar atoms, such as Si and Ge, adsorbed on the surface [115].

In what follows, we introduce the model and find an accurate analytic approximation for the velocity and diffusion coefficient. We show that at the origin of the ratchet effect is the internal DOF in such a dimer. Furthermore, we show that the velocity of the system is maximal at an optimal coupling strength, and that, similar to the phenomena of stochastic resonance [124] and resonant activation [125], it can be maximized also with respect to the noise intensity and frequency.

The generalization to atomic-scale friction experiments in the way proposed in the preceding chapter is quite obvious: instead of chains consisting of identical atoms consider a copolymer structure of two or more different constituents. In case of different constituents, the most important difference to a monomer is, of course, the impact the interaction of the different species exerts on the chain dynamics because this impact simply does not exist for a monomer. For exactly two constituents, choosing the dimer as a *minimal* model for a copolymer ensues by focusing on the "unit cell" of such a chain, namely a pair of different atoms. This enormous simplification will lead to qualitatively correct expectations as long as, after properly rescaling the system size, merely small corrections must be added to the results for the bare dimer when the actual chain length is accounted for.

Fortunately, the two most customary approximations, the strong and the weak coupling limit, promote precisely this simplification. In the strong coupling limit, the chain can be approximated by a single particle with higher order corrections due to the interaction of different constituents. In the weak coupling limit, the "unit cells" of the chain can be approximated by independent dimers with higher order corrections due to the extended length of the whole chain. In both cases, the dimer model is positively expected to be "well-behaved" and can safely be applied.

Also, this should hold for an array of AFM tips like the IBM Millipede mentioned in the previous chapter. If the tips were designed in two subunits

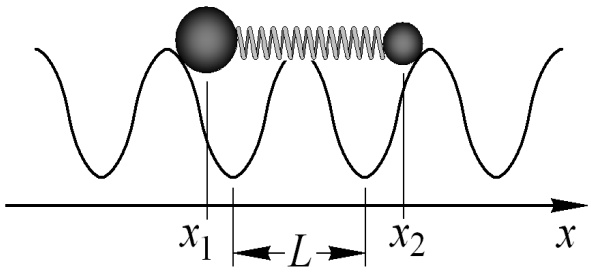

Figure 4.1: Schematic representation of the dimer model. The dimer constituents are labeled with coordinates x_1 and x_2, the corrugation length of the surface potential is denoted by L. Different sizes symbolize the unequal coupling to the surface.

that own a different coupling strength to the surface, the effect would be the same: the internal structure could be absorbed into the dimer's internal DOF.

The insufficient performance in the low coupling constant regime that will show up in the end of this chapter must not be misunderstood as a contradiction to the general applicability of the dimer model. As will be pointed out explicitely, the various approximations that were chosen to develop the model were not applicable to the weak coupling limit. This is so because of the violation of some assumptions concerning the complete thermalization of the dimer within specific time limits.

4.2 Model

We consider two overdamped coupled Brownian particles in symmetric synchronously flashing potentials, see Fig. 4.1. The equations of motion for the coordinates x_1, x_2 of the particles are

$$\eta \dot{x}_1 = -U'(x_1)\, f(t) - \kappa\,(x_1 - x_2 + a) + \sqrt{2\eta k_\mathrm{B} T}\,\xi_1(t) \tag{4.1}$$

and

$$\eta \dot{x}_2 = -\alpha U'(x_2)\, f(t) + \kappa\,(x_1 - x_2 + a) + \sqrt{2\eta k_\mathrm{B} T}\,\xi_2(t) \tag{4.2}$$

with η the viscous friction coefficient, $k_\mathrm{B}T$ the thermal energy, and $\xi_i(t)$ independent and unbiased Gaussian noises with δ-correlation $\langle \xi_i(t)\,\xi_j(s)\rangle = \delta_{ij}\,\delta\,(t-s)$. The periodic potential for the first particle is a harmonic function with amplitude ΔU and spatial period L

$$U(x) = \frac{\Delta U}{2}\left(1 - \cos\frac{2\pi x}{L}\right). \tag{4.3}$$

The parameter $\alpha \neq 1$ in Eq. (4.2) yields the amplitude of the potential felt by the second particle, $\alpha\Delta U$. Both potentials are periodically switched on and off by a rectangular signal $f(t) = f(t+\tau)$ of periodicity $\tau = \tau_{\text{on}} + \tau_{\text{off}}$ consisting of on-phases of duration τ_{on}, such that $f(t) = 1$ for $k\tau \leq t < k\tau + \tau_{\text{on}}$, and off-phases of duration τ_{off}, such that $f(t) = 0$ for $k\tau + \tau_{\text{on}} \leq t < (k+1)\tau$, where $k \in \mathbb{Z}$. For simplicity, we assume the interaction between the components to be elastic, with the spring constant κ and the rest length a.

4.3 Origin of symmetry breaking

As we will show below, the model (4.1), (4.2) exhibits the ratchet effect, *i.e.*, a non-zero velocity in the absence of any external forcing. At the origin of the effect in our model is the internal DOF. This is so, because the current is zero in the two opposite extremes of zero and rigid coupling. Indeed, in the uncoupled case, $\kappa = 0$, each of the two particles in Eqs. (4.1) and (4.2) finds itself in the flashing sinusoidal potential, where no current is possible for symmetry reason. On the other hand, in the opposite rigid limit, $\kappa \to \infty$, meaning $x_2 - x_1 = a$, one can consider the equation of motion for the center of mass and the relative coordinate,

$$X := \frac{x_1 + x_2}{2}\,, \qquad Y := x_2 - x_1 - a\,. \tag{4.4}$$

From the equations (4.1), (4.2) one obtains

$$\eta\dot{X} = -\frac{1}{2}\left[U'\left(X - \frac{Y+a}{2}\right) + \alpha U'\left(X + \frac{Y+a}{2}\right)\right] f(t) + \sqrt{\eta k_{\text{B}} T}\,\Xi_X(t) \tag{4.5}$$

and

$$\eta\dot{Y} = \left[U'\left(X - \frac{Y+a}{2}\right) - \alpha U'\left(X + \frac{Y+a}{2}\right)\right] f(t) - 2\kappa Y + \sqrt{4\eta k_{\text{B}} T}\,\Xi_Y(t)\,. \tag{4.6}$$

In the extreme case of rigid coupling, the distance between dimer components is fixed, $Y = 0$, so that from Eq. (4.5) one concludes that the center of mass finds itself in the potential $[U(X - a/2) + \alpha U(X + a/2)]\, f(t)/2$. Since both $U_1(x)$ and $U_2(x)$ are trigonometric functions of the same period, the resulting potential for X is also a trigonometric function of non-ratchet type, again excluding any possibility of current in the system.

In order to understand, how the internal DOF leads to the onset of the directed current, it is instructive to study the system dynamics in the asymptotic limit of large but finite stiffness κ. In this case, the dynamics of the relative coordinate Y occurs on the much faster time-scale than that of the center

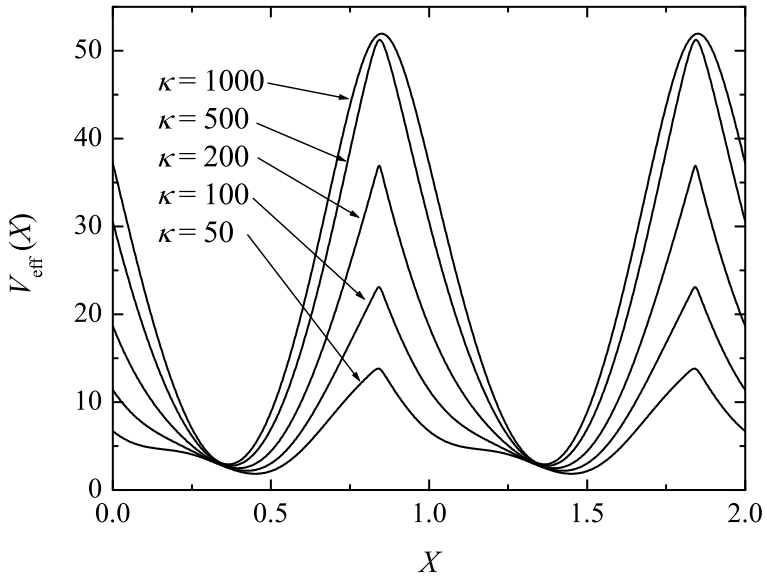

Figure 4.2: Effective potential Eq. (4.8) for the following parameter values in Eq. (4.3): $\Delta U = 100$, $L = 1$, $\alpha = 0.5$, $k_{\rm B}T = 1$, and five values of κ ranging from 1 000 (upper curve) to 50 (lower curve), as indicated.

of mass X. If the characteristic time-scale of change of the center of mass is much longer than the thermalization time scale for the relative coordinate Y, one can use the unnormalized probability distribution of the relative coordinate Y for a fixed value of X:

$$\rho(Y;X) = \exp\left(-\frac{\frac{1}{2}\kappa Y^2 + U\left(X - \frac{Y+a}{2}\right) + \alpha U\left(X + \frac{Y+a}{2}\right)}{k_{\rm B}T}\right). \qquad (4.7)$$

The slow coordinate X finds itself in a mean-field potential of the free-energy type

$$U_{\rm eff}(X) = -\frac{1}{2}\,k_{\rm B}T\,\ln\int\limits_{-\infty}^{\infty} dY\,\rho(Y;X)\,. \qquad (4.8)$$

Fig. 4.2 shows this effective potential for several values of the coupling constant, κ. It is seen that at high values of κ, the effective potential indeed represents a symmetric function prohibiting spontaneous currents, while reduction of κ leads to two effects: reduction of the potential amplitude and the onset of its asymmetry, allowing for the ratchet effect in the system.

4.4 Analytic relation for the velocity and diffusion coefficient

Our goal is to evaluate the average velocity,

$$v = \lim_{t\to\infty} \frac{\langle x_i(t)\rangle}{t}\,, \tag{4.9}$$

which will be identical for both indices for positive κ. For analytic evaluation of v, we assume a distinct inequality of amplitudes and deep potential wells for particle 1,

$$\Delta U \gg k_{\mathrm{B}}T, \qquad \alpha \ll 1, \tag{4.10}$$

allowing the periodic part of potential $U(x_1)$ to be harmonically approximated. When the potentials are switched on, coordinate x_1 will immediately relax to the nearest minimum of the potential $U(x_1)$ almost independently of x_2. If we suitably move the origin of the x-axis by integer multiples of L, we can always accomplish x_1 to be located in the interval from $-L/2$ to $L/2$ where $U(x_1)$ is minimal for $x_1 = 0$, thus rendering a straightforward harmonic approximation.

Our second assumption is that the on-phase of the driving is long enough to allow for the thermalization of the systems,

$$\tau_{\mathrm{on}} \gg \tau_{\mathrm{rel}}\,, \tag{4.11}$$

where τ_{rel} represents the characteristic relaxation time. In view of the condition (4.10), this quantity can be estimated as the relaxation time of the second particle, provided that the first particle is placed at $x_1 = 0$. In the on-phase, the potential energy of the second particle is

$$U_{\mathrm{on}}(x_2) = \alpha U(x_2) + \frac{\kappa}{2}\,(x_2 - a)^2\,. \tag{4.12}$$

The relaxation time in Eq. (4.11) can be estimated as $\tau_{\mathrm{on}} = \eta/\lambda$, where λ is the smallest non-vanishing eigenvalue of the corresponding Fokker-Planck operator $\frac{d}{dx_2}\big(U'_{\mathrm{on}}(x_2) + k_{\mathrm{B}}T\frac{d}{dx_2}\big)$.

Under the assumptions (4.10), (4.11), the joint probability distribution in the end of the on-phase is

$$W^{\mathrm{on}}(x_1, x_2) \propto \exp\left(-\frac{U''(0)\,x_1^2 + 2\alpha U(x_2) + \kappa\,(x_1 - x_2 + a)^2}{2k_{\mathrm{B}}T}\right), \tag{4.13}$$

up to the normalization constant. This probability distribution can be transformed to the center-of-mass probability distribution by integrating out the x_i to

$$W_1^{\mathrm{on}}(X) = \int_{-\infty}^{\infty} dx_1 \int_{-\infty}^{\infty} dx_2\; \delta\left(X - \frac{x_1 + x_2}{2}\right) W^{\mathrm{on}}(x_1, x_2)\,. \tag{4.14}$$

The expression for the distribution $W_2^{\mathrm{on}}(Y)$ of the relative coordinate in the end of the on-phase is the same, but with $Y + (x_1 - x_2 + a)$ as an argument in the delta-function.

For $f(t) = 0$, the beginning of the off-phase, the equations of motion for the center of mass, Eq. (4.5), and the relative coordinate, Eq. (4.6), describe the Wiener and Ornstein-Uhlenbeck processes, respectively. Using the corresponding transition probabilities, the center-of-mass probability distribution in the end of the off-phase can be expressed as

$$W_1^{\mathrm{off}}(X) \propto \int_{-\infty}^{\infty} dX' \, \exp\left(-\frac{\eta\,(X - X')^2}{2\tau_{\mathrm{off}} k_{\mathrm{B}} T}\right) W_1^{\mathrm{on}}(X')\,, \tag{4.15}$$

up to a normalization constant. In the same manner, we find the distribution of the relative coordinate in the end of the off-phase,

$$W_2^{\mathrm{off}}(Y) \propto \int_{-\infty}^{\infty} dY' \, \exp\left(-\frac{\kappa\left(Y - e^{-2\kappa\tau_{\mathrm{off}}/\eta}\, Y'\right)^2}{2k_{\mathrm{B}} T\left(1 - e^{-4\kappa\tau_{\mathrm{off}}/\eta}\right)}\right) W_2^{\mathrm{on}}(Y_0)\,, \tag{4.16}$$

up to a normalization constant.

At the beginning of the next on-phase, x_1 may either drop back into the same potential well where it was one period ago or fall into a neighboring well, with the respective probabilities depending on the properties of

$$W^{\mathrm{off}}(x_1) = \int_{-\infty}^{\infty} dX \int_{-\infty}^{\infty} dY \, \delta\left(x_1 - X + \frac{Y + a}{2}\right) W_1^{\mathrm{off}}(X)\, W_2^{\mathrm{off}}(Y)\,. \tag{4.17}$$

This enables us to calculate the probability to find particle 1 between the k-th and the $(k+1)$-th maximum (*i.e.*, within the basin of attraction of the minimum at kL) by

$$P_k = \int_{kL - L/2}^{kL + L/2} dx_1 \, W^{\mathrm{off}}(x_1)\,, \tag{4.18}$$

resulting in the average velocity

$$v = \frac{L}{\tau} \sum_{k=-\infty}^{\infty} k P_k \tag{4.19}$$

and diffusion coefficient

$$D = \frac{L^2}{2\tau} \sum_{k=-\infty}^{\infty} k^2 P_k - \frac{v^2 \tau}{2}\,. \tag{4.20}$$

4.5 Results and discussion

4.5.1 Symmetry and dimer length

In the following, we present a comparison of simulation data from Langevin equations (4.1) and (4.2) with numerical results from our theory according to Eqs. (4.19) and (4.20). We have chosen the following constant parameter values: $\eta = L = 1$, $\Delta U = 100$, and $\alpha = 0.05$, so that conditions (4.10) are guaranteed throughout. Successively, four parameters were varied: rest length (a), thermal energy ($k_B T$), switching frequency (ω), and coupling strength/elasticity (κ). Simulation data represents an average of 15 trajectories for velocity, 200 for diffusion, where each single trajectory covers a time span of 1.25×10^4 in dimensionless units. All simulations are performed for the duty cycle $\tau_{\mathrm{on}}/\tau = 1/2$ (*i.e.*, $\tau_{\mathrm{on}} = \tau_{\mathrm{off}}$).

The inherent mirror symmetry of Langevin equations (4.1) and (4.2) implies that the current is an odd function of the dimer length a. As translational symmetry of the periodic potential $U(x)$ permits shifts by integer multiples of period L, we recognize this symmetry to be valid for all integer k according to $v(a) = v(kL + a) = -v(kL - a)$. This means that for all $a = kL/2$ the net current must vanish, $v(kL/2) = 0$.

The sign of the current depends on the character of the dimer's deformation during the on-phase. If the dimer was squeezed, then after turning the potentials off, the first particle will move to the left of its original position. Consequently, it will diffuse into the left maximum with greater probability than into the right one, and will be trapped there in the next on-phase. Since the character of the potential (4.12) is such that the dimer is squeezed for $kL < a < (k + 1/2)L$, $k \in \mathbb{Z}$, the overall velocity will be negative in this case. Following an analogous line of reasoning, we conclude that the velocity will be positive for $(k + 1/2)L < a < (k + 1)L$.

Both features, current reversal and symmetry, are shown in Fig. 4.3 for dimer lengths a within the interval from 0 to L. At low switching frequency ($\omega = 2\pi/\tau = 10$), the coincidence of theory and simulation is unequivocal. Current reversal appears at a equal to integer multiples of $L/2$, as explained above. In each node, the average velocity is an odd function of the dimer length. This qualitative behavior is not impaired by higher frequencies, as is also shown in this figure. For growing frequency, the exact probability distribution will increasingly deviate from the stationary Boltzmann distribution $W^{\mathrm{on}}(x_1, x_2)$ given by Eq. (4.13). Therefore, our theoretical prediction of the average velocity exceeds the simulation data for $\omega \gtrsim 20$.

Nevertheless, even for higher frequencies, Eq. (4.19) very accurately predicts the behavior of the current for a near all integer multiples of L. This is so because in this case, the potential (4.12) has a single minimum, with the relaxation time given approximately by $\tau_{\mathrm{rel}}\,(a \simeq kL) \approx \eta/\left[\kappa + \alpha U''(0)\right]$, $k \in \mathbb{Z}$.

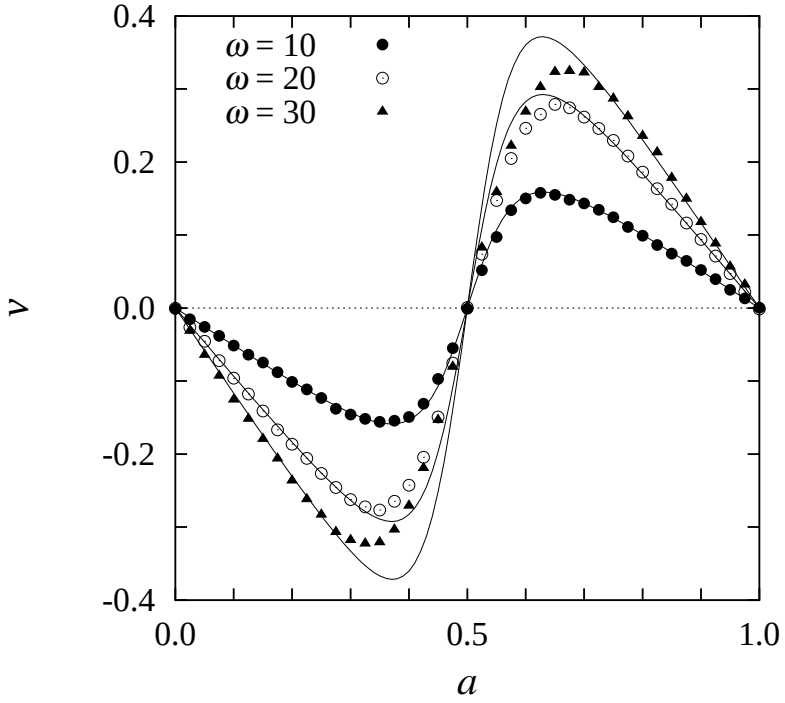

Figure 4.3: Average velocity v *vs.* rest length a at three different switching frequencies $\omega = 10$, 20, 30, for $\eta = k_B T = L = 1$, $\Delta U = 100$, $\alpha = 0.05$, and $\kappa = 50$. Circles and triangles are simulation data, solid lines show the corresponding theoretical predictions. The results are uneven periodic functions with period L. A single period of the dimer's rest length ($0 \leq a \leq L$) is shown. With increasing frequency, theoretical prediction looses accuracy for $a \approx L/2$.

For the parameter values chosen, this relaxation time is much smaller than the duration of the on-phase, so the condition (4.11) is satisfied. On the other hand, for $a \simeq (k + 1/2)L$, the potential (4.12) becomes bistable, so that the relaxation of the coordinate x_2 involves a slow process of thermally activated hopping over the potential barrier with a substantially longer relaxation time.

4.5.2 Dependence on temperature

The temperature dependence of v reveals a good agreement of simulation and theory over two orders of magnitude of thermal energy, as does the diffusion coefficient D (Fig. 4.4). The v-$k_B T$-diagram bears the signature of stochastic resonance as there is a clear-cut maximum of the current for an optimal amount of noise in the system. On the one hand, if temperature becomes zero, there is no motion at all and the current must vanish. On the

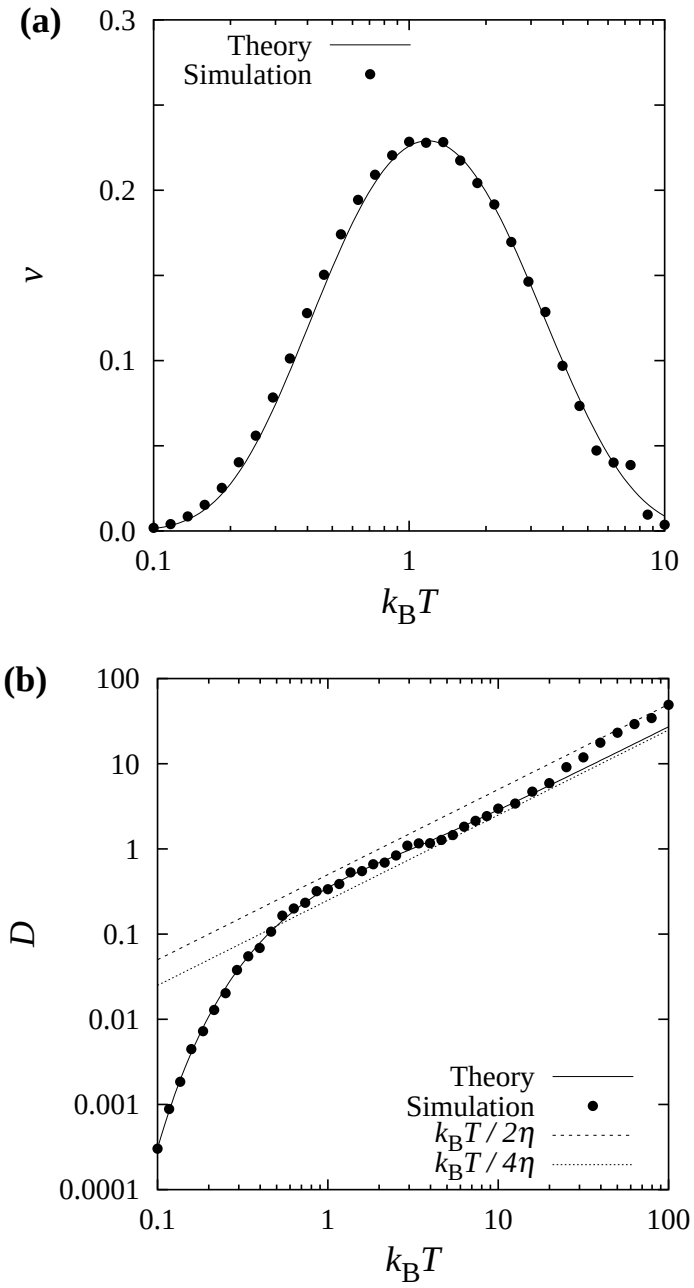

Figure 4.4: (a) Average velocity v *vs.* thermal energy $k_B T$ for $\eta = L = 1$, $\Delta U = 100$, $\alpha = 0.05$, $\omega = 25$, $\kappa = 50$, and $a = 0.75$. Solid line: analytic expression (4.19); circles: simulations. The velocity clearly shows a stochastic resonance-like maximum at $k_B T \simeq 1$. (b) Diffusion coefficient D *vs.* $k_B T$ for the same parameter values as in (a). Solid line: analytic expression (4.20); circles: simulations. At $k_B T \simeq 1$, D starts to converge towards $k_B T / 4\eta$ (dashed line).

other hand, if temperature increases above all limits, the effective potential, Eq. (4.8), becomes insignificant and overall symmetry is restored, thus inhibiting any ratchet effect. In between, there must be a finite current (for all $a \neq kL/2$, $k \in \mathbb{Z}$) because at any finite value of T the distribution $W^{\mathrm{off}}(x_1)$ is non-symmetric at $x_1 = 0$, leading to a non-vanishing sum in Eq. (4.19).

The dashed line in figure 4.4(b) corresponds to the free diffusion of an analogous system where the periodic potential $U(x)$, Eq. (4.3), stays switched off permanently and where in lieu thereof the temperature is periodically switched on ($k_{\mathrm{B}}T > 0$) and off ($k_{\mathrm{B}}T = 0$) according to the same duty cycle $\tau_{\mathrm{on}}/\tau = 1/2$. For very high temperature, the diffusion coefficient converges towards this free diffusivity $D_{\mathrm{free}} = k_{\mathrm{B}}T/4\eta$, thereby indicating the vanishing dependence on the periodic potential in this temperature regime. At about $k_{\mathrm{B}}T \simeq 1$, where there is a maximal current, the actual diffusion coefficient has discernibly risen above its free counterpart and starts to converge from this higher value. At $T \to 0$, the decline of D is much steeper than of D_{free} due to the increasing probability of x_1 returning to its starting point of the previous on-phase, corresponding to a "loss" of diffusion over a whole period.

4.5.3 Dependence on driving frequency

Fig. 4.5(a) illustrates how switching frequency $\omega = 2\pi/\tau$ affects the accuracy of the theoretical prediction. It reproduces the asymptotic behavior for $\omega \to 0$ and for $\omega \to \infty$, where $v \to 0$. The explanation for this is apparent: On the one hand, there will be no net probability current for extremely long times of free diffusion because $W^{\mathrm{off}}(x_1)$ gets very flat. On the other hand, $W^{\mathrm{off}}(x_1)$ will be sharply peaked for very short times of free diffusion so that the $P_k \approx 0$, for $k \neq 0$, generating no current, either. In between, there is necessarily a finite amount of probability spreading beyond the interval from $-L/2$ to $L/2$, giving rise to a finite net current. This current shows a clear-cut maximum, too, which one would call a resonant activation in terms of escape from a metastable state. The aforementioned deviation of W^{on} for high frequencies thereby leads to a slight overestimation of the maximal current.

The diffusion coefficient (see Fig. 4.5(b)) also converges towards $D_{\mathrm{free}} = k_{\mathrm{B}}T/4\eta$, which in this case is $D_{\mathrm{free}} = 1/4$, but here the convergence takes place in the low frequency limit, as it provides long times of free diffusion. In the high frequency limit, the time of free diffusion becomes too short to allow for a finite current, in analogy to the low temperature limit. The maximal value of the diffusion coefficient can be found in vicinity to the resonant activation frequency. Please, note that the statistical nature of simulation data regarding the diffusion coefficient is responsible for the scattering. In Fig. 4.4(b), this effect is merely obscured by the logarithmic scale that spans five orders of magnitude.

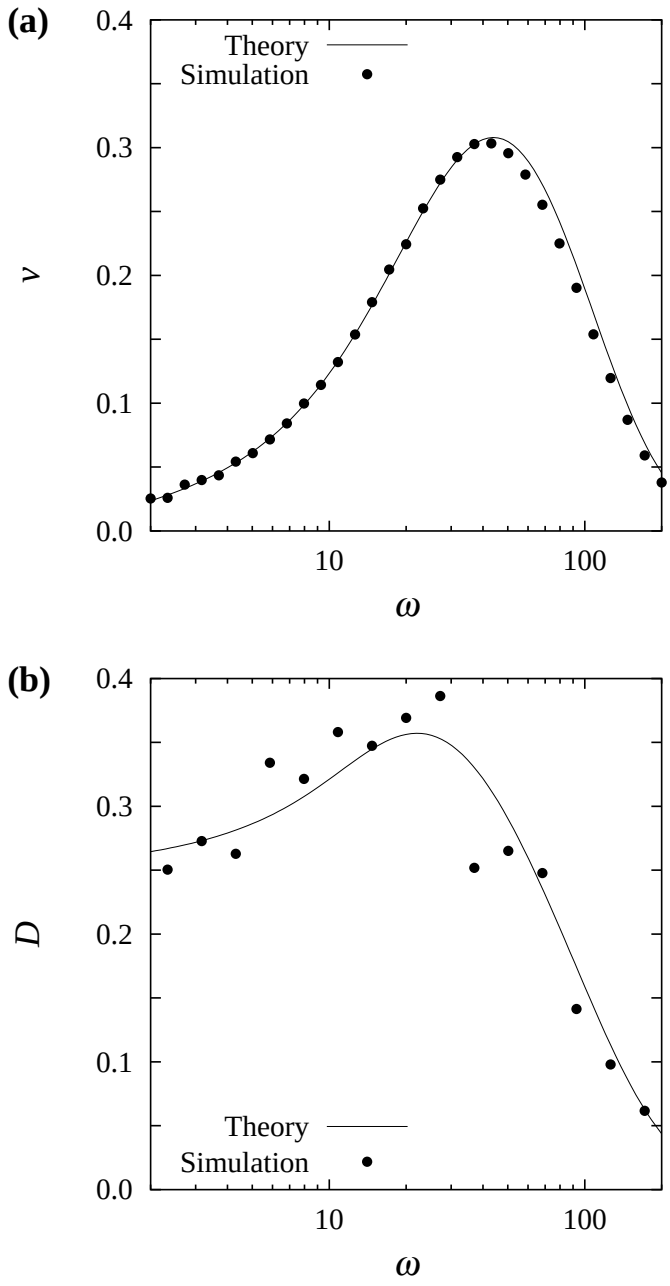

Figure 4.5: (a) Average velocity v *vs.* switching frequency ω for $\eta = k_B T = L = 1$, $\Delta U = 100$, $\alpha = 0.05$, $\kappa = 50$, and $a = 0.7$. For $\omega \gtrsim 40$, the theoretical prediction starts to deviate slightly from simulation data. The reason for this is that τ is too short to allow for a relaxation of x_2 according to W^{on}. A resonant activation-like maximum stands out at $\omega \simeq 40$. (b) Diffusion coefficient D *vs.* ω for the same parameter values as in (a).

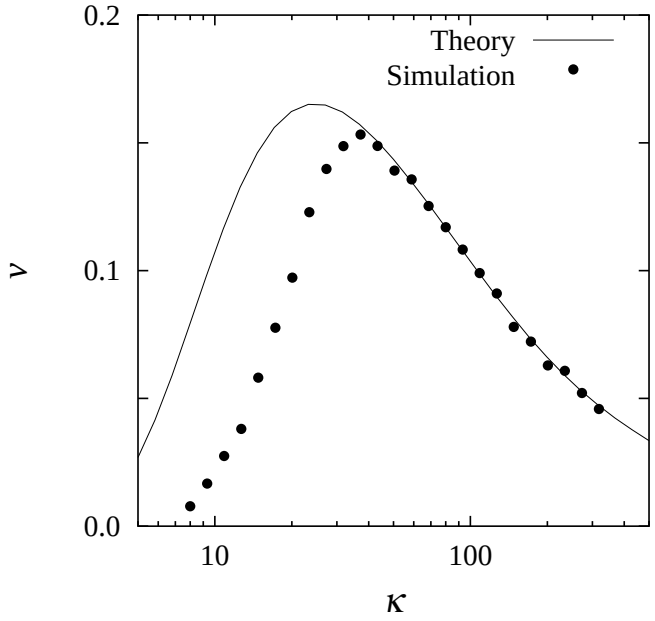

Figure 4.6: Average velocity v *vs.* elastic coupling κ for $\eta = k_B T = L = 1$, $\Delta U = 100$, $\alpha = 0.05$, $\omega = 10$, and $a = 0.7$. For low values of κ, the assumed Boltzmann distribution $W^{\mathrm{on}}(x_1, x_2)$ cannot describe the real situation sufficiently exact, thereby predicting an exceedingly high average current. This is due to the onset of a much slower relaxation process taking effect at low κ.

4.5.4 Dependence on elasticity

The line of reasoning is different when it comes to the role of the elastic coupling κ (Fig. 4.6). There will be an asymptotically vanishing net current for $\kappa \to 0$ and for $\kappa \to \infty$, but this is due to the decisive role of the internal DOF, as explained in section 4.3. The internal DOF can only exist as long as κ is finite, thus breaking symmetry and inducing a ratchet effect. Similar to temperature and frequency, where we could find a stochastic resonance-like and a resonant activation-like maximum, respectively, we can distinguish an optimal value of the coupling constant that leads to a maximal current.

We shall briefly discuss the obvious inability of (4.19) to give any accurate prediction of the net current for small values of the elastic coupling constant. We see a pronounced spread between theory and simulation for $\kappa \lesssim 30$. For decreasing κ, the potential $U_{\mathrm{on}}(x_2)$, Eq. (4.12), is transformed to a multistable one-dimensional landscape consisting of two or more relative minima. The barriers separating these minima approach a height of $\alpha\Delta U$ as $\kappa \to 0$, leading to a thermalization time much larger than τ_{on}. Since $W^{\mathrm{on}}(x_1, x_2)$ relies on the equilibrium distribution, it cannot describe the actual probability distribution at the end of the on-phase with sufficient exactitude. Consequently, the

theory does not hold for low κ. For this reason, any viable theoretical prediction of the diffusion coefficient depending on the elastic coupling constant could not be made.

4.6 Concluding remarks

In this chapter, we have demonstrated, both analytically and by means of numerical simulations, that an internal DOF can lead to the onset of the symmetry breaking and to a ratchet effect in a dimer finding itself in a flashing symmetric potential. The current can be maximized with respect to various system parameters describing the properties of the potential, environment, and coupling. We expect that the effect will be also observable for other asymmetry types, *e.g.*, inclusion of additional degrees of freedom and/or inertia or different values of the friction coefficient of the two particles should preserve the effect. Detailed studies of the intriguing possibilities offered by dissimilar friction coefficients will be the subject of the following chapter.

In view of the new results for experimental control of atomic-scale friction [66], the possibility to observe a nanotribological system exhibiting the ratchet effect seems to be close at hand. The reason for this is that the way friction control experiments achieve the modulation of the dissipation of the sliding object is very similar to the externally imposed modulation necessary to drive a system out of equilibrium. It can be done in three different ways:

- by mechanically excited vibration,
- by varying load onto the tip,
- by applying an AC voltage.

Each way modulates the coupling between probe and surface. In any case, a periodic modulation of some kind is involved which can be used as a drive for the ratchet effect.

The symmetry breaking that is of fundamental importance to the ratchet effect can be established by means of the internal DOF arising from the relative coordinate of the ratchet model, *i.e.*, from the interaction of the two different constituents of a chain/copolymer (or an array, if suitably extended into the plain). For example, the experimental setup can be similar to a single file diffusion experiment (see Fig. 4.7), where particles are placed within etched troughs on a crystal surface of some sort, thereby imposing a one-dimensional geometry. Of course, such an experiment must be reduced in size, from microbeads to nano-droplets, which is by no means a trivial task. Then an actuation by AC voltage could directly evoke a transport without external bias that could be measured directly via the position of the droplet.

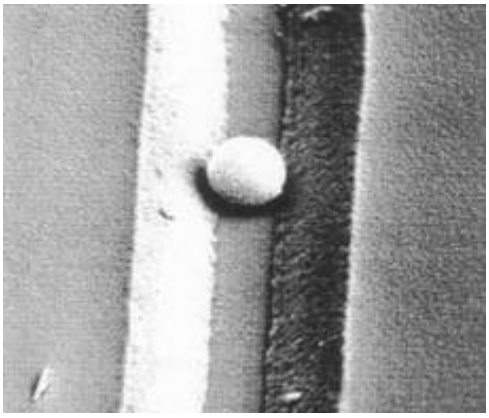

Figure 4.7: Image of a microbead in a one-dimensional channel that is used in a single file diffusion experiment. Image from the Homepage of C. Bechinger, 2. Physikalisches Institut, Universität Stuttgart.

An indirect proof via the deflection of a cantilever beam that is attached to the nano-droplet is more promising because the experimental setup is very close to the aforementioned attempts to control friction in an FFM experiment through the actuation of nano-contacts. The main difference is that instead of a direct contact between the FFM tip and the surface a small island of a suitably chosen material (*i.e.*, consisting of at least two dissimilar constituents) is intercalated. Thereby, the probe–sample interaction will primarily be established, not by the contact of the tip to the sample, but by the interaction between sample and surface.

With this setup, three different modes of operation are possible:

1. Tip and surface are in lateral motion without actuation. This is equivalent to a usual FFM measurement where the force–velocity curve for the material under consideration is determined.

2. There is no lateral motion between tip and surface but the contact is actuated by an applied AC voltage. In this mode, a possible ratchet effect would evoke a bending of the cantilever that grows until the restoring force precisely counteracts the ratchet effect.

3. Both, lateral motion and contact actuation, are in operation. This mode allows for an additional control of friction by means of the ratchet effect being superimposed on the forced lateral motion.

To our knowledge, a threefold friction experiment of this kind has not yet been performed. Since the different components (*e.g.*, the manipulation of nano-droplets on surfaces, the actuation of nanometer-size contacts, *etc.*) are all available and successfully applied, we are quite confident that an experimental verification of our findings is, in principle, technically feasible.

5 Ratchet effect of a dimer II The case of asymmetric friction

Nichts setzt dem Fortgang der Wissenschaft
mehr Hindernis entgegen,
als wenn man zu wissen glaubt,
was man noch nicht weiß.

Georg Christoph Lichtenberg

5.1 Introduction

Throughout this thesis, it has always been emphasized how versatile the dimer model can be applied to distant and seemingly unrelated fields of research. For example, the model treated within this penultimate chapter was originally put into the context of molecular motors—but with a clear relation to atomic-scale friction. Anyway, the bottom line is much the same as in the preceding chapter: results from the abstract dimer model to the concrete situation of an atomic-scale friction experiment can be transferred in the same manner as explained in sections 4.1 and 4.6.

Since molecular motion within the body of living organisms takes place in a noisy and viscous environment, fluctuation and dissipation phenomena are of paramount importance with regard to developing and investigating theoretical models of molecular motors [97, 126]. The key mechanism of these models that enables the transformation of isotropic thermal noise into average unidirectional motion is the ratchet effect [75, 127]. For over a decade it is known experimentally that the internal properties of motor molecules (*e.g.*, kinesin, myosin, *etc.*) play, if not the decisive, at least a prominent role in the emergence of directed motion in living organisms [118]. These internal properties, their symmetry-breaking and transport generating ef-

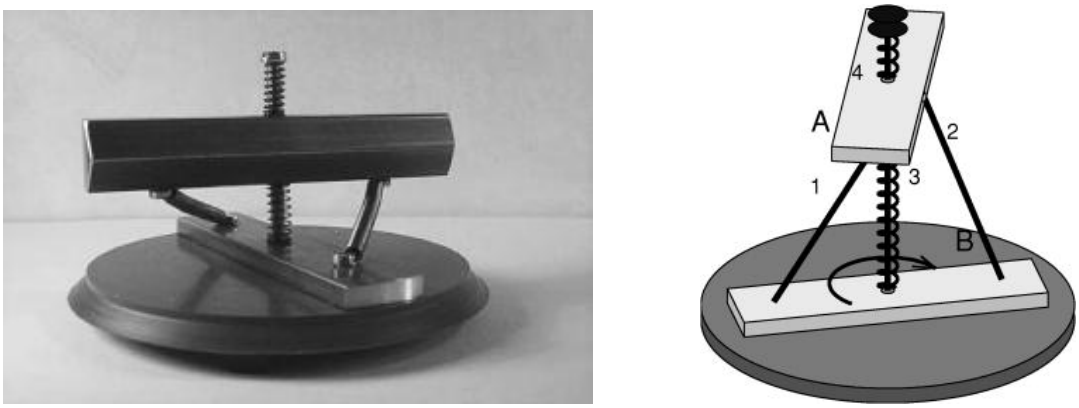

Figure 5.1: Mechanical ratchet device with broken friction symmetry. It consists of two (upper and lower) helically rotating coupled plates. The supporting bottom plate creates friction for the lower plate. A driving oscillating or fluctuating force is applied to the upper plate, *e.g.*, by hitting it slightly from various directions. Colored noise was created by the sound from a fog horn, acting on a horizontal membrane glued on top of the upper plate. In all cases of forcing vertically (from above or below), the helical system was observed to rotate only clockwise when viewed from above. Taken from [137].

fects in spite of originally symmetric environments, are addressed by numerous theoretical studies of coupled particle chains [113], arrays [119], and dimers [88,89,101,107,120], to name but a few. Dimers are especially suited to model such systems because of their internal degree of freedom, their structural simplicity, and because they can easily mimic geometrical properties of motor molecules like the stepwise "hand-over-hand" motion of two molecular branches.

A subclass of systems with internally broken symmetry consists of ratchet systems based on inhomogeneous friction. In underdamped systems, friction applied to the internal degree of freedom can lead to self-propulsion [129], even in the absence of an external potential [130]. Another way of enforced frictional inhomogeneity is a space dependent friction coefficient, both for overdamped and underdamped ratchets [131–133]. In non-ratcheting systems, sliding friction of dimers on periodic substrates reveals nonlinear velocity dependence and a striking periodic variation with the ratio of dimer length and substrate period [134–136].

A macroscopic mechanical device with frictional asymmetry was experimentally realized by Nordén *et al.* in 2001 [137]. It converts fluctuating motion (actual sound waves from a fog horn) into unidirectional rotation, see Fig. 5.1. Although it is an inertia ratchet, its relation to the overdamped model we will discuss within this chapter is very close. It consists of two masses that are harmonically coupled by stiff springs. One mass can freely

rotate (since the air resistance is negligibly small) whereas the other mass is attenuated through sliding friction on the ground plate. While the upper mass is exposed to random forcings in various directions, accompanied by colored noise, the whole apparatus is on average always turning clockwise (as seen from above). This "gadget" was intended to visualize the underlying Brownian dynamics of a molecular motor with broken friction symmetry. If we imagine the device being immersed in a viscous fluid (*e.g.*, oil), it may serve to visualize the overdamped Brownian motion of our dimer model.

In this chapter, we study the same one-dimensional model consisting of two elastically coupled Brownian particles in a symmetric flashing potential as in chapter 4. Instead of a different coupling to the surface potential we now establish two independent friction coefficients, thereby breaking the friction symmetry of the dimer. This kind of friction asymmetry is different from the two-state systems with protein friction modeling a molecular motor in [138–140], where fluctuations are rectified by means of switching between states of high and low friction in order to account for cyclical attachment to the track (*e.g.*, cell filaments). In our model, the friction coefficients are neither time nor space dependent but fixed quantities generating a nonzero average velocity. We show that the dimer velocity can be maximized with respect to the noise intensity and driving frequency, and that it is maximal at some optimal coupling strength.

5.2 Model

The total energy U^{tot} of the dimer consists of two parts: a flashing potential representing the interaction of each dimer component with the surface plus the bond energy of the dimer,

$$U^{\mathrm{tot}}(x_1, x_2, t) = [U(x_1) + U(x_2)]\, f(t) + \frac{\kappa}{2}(x_2 - x_1 - a)^2 . \tag{5.1}$$

The surface interaction U is a sinusoidal function with barrier height ΔU and spatial period L,

$$U(x_i) = \frac{\Delta U}{2}\left(1 - \cos\frac{2\pi x_i}{L}\right). \tag{5.2}$$

Both contributions, $U(x_1)$ and $U(x_2)$, are synchronously and periodically switched on and off by a rectangular signal $f(t) = f(t+\tau)$ of periodicity $\tau = \tau_{\mathrm{on}} + \tau_{\mathrm{off}}$. On-phases of duration τ_{on} and off-phases of duration τ_{off} alternate such that $f(t) = 1$ for $k\tau \le t < k\tau + \tau_{\mathrm{on}}$, and $f(t) = 0$ for $k\tau + \tau_{\mathrm{on}} \le t < (k+1)\tau$, where $k \in \mathbb{Z}$. The coupling interaction is assumed to be elastic, with spring constant κ and rest length a, meaning that there is no internal force acting between the components if $x_2 - x_1 = a$.

The dynamics of the dimer is modeled as overdamped Brownian motion at absolute temperature T, yielding two coupled equations of motion,

$$\eta_i \dot{x}_i(t) = -\frac{\partial U^{\mathrm{tot}}(x_1, x_2, t)}{\partial x_i} + \sqrt{2\eta_i k_{\mathrm{B}} T}\, \xi_i(t)\,, \tag{5.3}$$

for $i \in \{1,2\}$. The η_i are the viscous friction coefficients of the respective dimer components, k_{B} is the Boltzmann constant, and the $\xi_i(t)$ are Gaussian white noises with $\langle \xi_i(t) \rangle = 0$ and $\langle \xi_i(t)\, \xi_j(s) \rangle = \delta_{ij}\, \delta(t-s)$, for $i, j \in \{1,2\}$. The ratio of the friction coefficients can be merged into a dimensionless asymmetry parameter α, allowing us to identify

$$\eta := \eta_1 \quad \text{and} \quad \alpha := \frac{\eta_2}{\eta_1} \tag{5.4}$$

throughout the rest of the text. For definiteness, we will focus on the case $\alpha \leq 1$. In other words, x_1 is the "slow" and x_2 the "fast" component of the dimer.

The quantities of main interest to us are the average dimer velocity

$$v := \lim_{t\to\infty} \frac{\langle x_i(t) \rangle}{t} \tag{5.5}$$

and the diffusion coefficient

$$D := \lim_{t\to\infty} \frac{\langle x_i^2(t) \rangle - \langle x_i(t) \rangle^2}{2t}. \tag{5.6}$$

Focusing on $\kappa > 0$, both quantities are independent of the index i.

5.3 Origin of the ratchet effect

Before deriving the analytical approximations for the current and diffusion coefficient of the system described in the previous section, we would like to qualitatively discuss the basic mechanisms leading to the onset of a spontaneous current. The origin of the ratchet effect can be understood from Fig. 5.2, depicting various stages of the dimer's motion.

In each on-phase of driving, the dimer may be trapped either (A) near the minimum of the potential $U(x)$, or (B) near its maximum. In case A, the dimer is compressed so that, immediately after the potential $U(x)$ is switched off, the distance between the dimer components will begin to increase towards the equilibrium value a. This relaxation will proceed predominantly via the motion of that component, whose friction coefficient is the smaller. As a result, the geometrical center of the dimer will more likely be displaced in the direction of that component in the end of each off-phase so that the

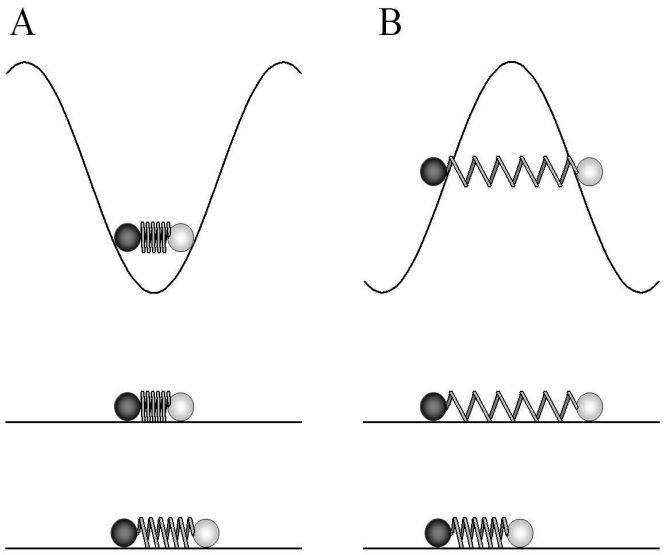

Figure 5.2: Schematic representation of two different dimer equilibrium configurations during on-phases (dimer plus sinusoidal potential, upper part) and their subsequent deterministic relaxation (off-phase, lower part). Dimer constituents are depicted as black (x_1) and white (x_2) balls connected by a spring. For each configuration, a typical relaxation scenario of the dimer is shown for low α values, *i.e.*, x_2 moves faster than x_1. The upper horizontal line represents the initial distribution when the potential U is switched off, the lower line exemplifies the equilibrated spring. The net displacement of the dimer's geometrical center is the origin of the ratchet effect.

overall current direction in Fig. 5.2 (A) will be to the right. Turning to case B, the dimer is initially stretched over one of the maxima of the potential $U(x)$. Immediately after this potential is switched off, the dimer length will relax toward the equilibrium value predominantly via the motion of the component with the smaller friction coefficient while the other component will move much more slowly. As a result, the geometrical center will, on average, be displaced to the left in the end of each off-phase, resulting in the overall current in the negative direction.

Depending on the rest length and stiffness of the dimer, as well as on the values of the friction coefficient of its components, one of these two scenarios will dominate. At specific values of the system's parameters, both mechanisms can even mutually cancel, resulting in zero net current.

5.4 Analytical derivation of average dimer velocity and diffusion coefficient

The key to a description of the dimer dynamics is a treatment in terms of transition probabilities from distinct potential wells to neighboring wells for the various relevant dimer configurations (*e.g.*, stretched or compressed). However, at a critical coupling strength,

$$\kappa_{\text{crit}} := U''(0) = \frac{2\pi^2 \Delta U}{L^2}\,, \tag{5.7}$$

the distinctness of potential minima is severely disturbed by antagonistic superposition of equally strong sinusoidal and elastic parts. It is only for κ well below or above κ_{crit} that we were able to deduce applicable schemes leading to analytical approximations for weak and strong coupling. This can be expressed through the dimensionless parameter

$$\epsilon := \frac{\kappa}{\kappa_{\text{crit}}} = \frac{\kappa L^2}{2\pi^2 \Delta U}\,, \tag{5.8}$$

thereby referring to $\epsilon \ll 1$ as weak-coupling regime, and $\epsilon \gg 1$ as strong-coupling regime.

In order to gain analytical results, we need to make three assumptions. The first of them concerns the barrier height. While the periodic driving $f(t)$ of the surface interaction is necessary to drive the dimer out of equilibrium, its amplitude ΔU must be large enough to substantially "freeze" the diffusion in the on-phase. Escapes from potential minima must be rare events in order to neglect them completely within an analytical approximation. Therefore, we require

$$\Delta U \gg k_{\text{B}} T\,. \tag{5.9}$$

This also guarantees a sharply peaked equilibrium probability distribution of the dimer components whenever the driving is active, $f(t) = 1$.

Our second assumption is that τ_{on}, the duration of the switching-on of the surface potential, must be substantially larger than the relaxation time $\tau_{\text{on}}^{\text{rel}}$ of the slower component x_1,

$$\tau_{\text{on}} \gg \tau_{\text{on}}^{\text{rel}}\,. \tag{5.10}$$

Otherwise, the dimer would not reach a quasistationary equilibrium distribution during the on-phase. This relaxation time is mainly governed by the curvature of the total potential U^{tot} at its relative minima. Since the maximal curvature of the potential U equals to κ_{crit}, the relaxation time in the on-phase is roughly $\tau_{\text{on}}^{\text{rel}} \sim \eta/(\kappa + \kappa_{\text{crit}})$.

Our third assumption requires that κ is not too small since the spring constant determines the relaxation time $\tau_{\text{off}}^{\text{rel}} = \alpha\eta/(1+\alpha)\kappa$ of the dimer length in the off-phase (see below). For

$$\tau_{\text{off}} \gg \tau_{\text{off}}^{\text{rel}}\,, \tag{5.11}$$

a lower bound of κ is given by $\kappa \gg \alpha\eta/[(1+\alpha)\tau_{\text{off}}]$ to ensure a stationary equilibrium distribution of the relative coordinate at the end of the off-phase.

5.4.1 Weak-coupling approximation

Because of conditions (5.9) and (5.10), at the end of each on-phase, $f(t) = 1$, the system finds itself in a sharply peaked equilibrium distribution. Both dimer components will be localized close to minima of $U(x_i)$, say, $x_1 \approx kL$ and $x_2 \approx (k+m)L$, where $k, m \in \mathbb{Z}$. Further, we expect both dimer components to be localized near the positions where $\partial U^{\text{tot}}/\partial x_1 = \partial U^{\text{tot}}/\partial x_2 = 0$, whence we can directly deduce $\sin\left(2\pi x_1^{\text{eq}}/L\right) = -\sin\left(2\pi x_2^{\text{eq}}/L\right)$ with $x_1^{\text{eq}} + x_2^{\text{eq}} = (2k+m)\,L$. This means that any equilibrium distribution is completely described by the pair (k, m). By a harmonic approximation of U^{tot} about $x_1 = kL$ and using $x_2^{\text{eq}} = (2k+m)L - x_1^{\text{eq}}$, the equilibrium positions can be calculated approximately for small ϵ and not too large $|m|$ as

$$x_1^{\text{eq}} = kL + \frac{\epsilon}{1+2\epsilon}\,(mL - a) \tag{5.12}$$

and

$$x_2^{\text{eq}} = (k+m)\,L - \frac{\epsilon}{1+2\epsilon}\,(mL - a)\,. \tag{5.13}$$

In the off-phase, $f(t) = 0$, the equation of motion (5.3) can be decoupled by introducing a dynamically weighted central coordinate,

$$X := \frac{x_1 + \alpha x_2}{1+\alpha}\,, \tag{5.14}$$

and a relative coordinate,

$$Y := x_2 - x_1 - a\,. \tag{5.15}$$

We find for the central coordinate

$$(1+\alpha)\,\eta\dot{X} = \sqrt{2\,(1+\alpha)\,\eta k_{\mathrm{B}}T}\,\xi_X(t), \tag{5.16}$$

which is a Wiener process, and for the relative coordinate

$$\frac{\alpha\eta}{1+\alpha}\,\dot{Y} = -\kappa Y + \sqrt{\frac{2\alpha\eta k_{\mathrm{B}}T}{1+\alpha}}\,\xi_Y(t), \tag{5.17}$$

being an Ornstein-Uhlenbeck (OU) process. Here, $\xi_X(t)$ and $\xi_Y(t)$ are once again independent delta-correlated Gaussian noises. For initial central coordinate $X^{\mathrm{eq}} = (x_1^{\mathrm{eq}} + \alpha x_2^{\mathrm{eq}})/(1+\alpha)$, see Eqs. (5.12)-(5.14), the Wiener process evolves, in the end of the off-phase, to the probability density

$$W_1(X) = C_X\,\exp\left(-\frac{(1+\alpha)\,\eta\,(X-X^{\mathrm{eq}})^2}{4k_{\mathrm{B}}T\tau_{\mathrm{off}}}\right) \tag{5.18}$$

where C_X is a normalization constant. Because of condition (5.11), the OU process approaches its long-time asymptotics

$$W_2(Y) = C_Y\,\exp\left(-\frac{\kappa Y^2}{2k_{\mathrm{B}}T}\right), \tag{5.19}$$

with a normalization constant C_Y. The joint probability distribution for the original dimer components follows by a backward transformation,

$$\begin{aligned} W(x_1,x_2) &= \iint dX\,dY\,\delta\left(X - \frac{x_1+\alpha x_2}{1+\alpha}\right)\,\delta\left(Y - x_2 + x_1 + a\right)\,W_1(X)\,W_2(Y) \\ &= W_1\left(\frac{x_1+\alpha x_2}{1+\alpha}\right)\,W_2\left(x_2 - x_1 - a\right). \end{aligned} \tag{5.20}$$

The pair distribution function $W(x_1,x_2)$ is a valid approximation at precisely that moment in time when the potential $U(x_i)$ is switched on again.

Any initial dimer configuration (j,m) can naturally be mapped onto $(0,m)$ by a shift of the coordinate axis by j multiples of L. From there on, the transition probability into any final configuration (k,l) is given by an integral of the pair distribution function,

$$P_{(0,m)\to(k,l)} = \int\limits_{c^-(\alpha)}^{c^+(\alpha)} dx_1 \int\limits_{b^-(x_1)}^{b^+(x_1)} dx_2\,W(x_1,x_2). \tag{5.21}$$

The integration limits, $c^{\pm}(\alpha)$ and $b^{\pm}(x_1)$, must be chosen so as to match the basins of attraction of each minimum, which is a precarious matter for moderately weak coupling. A naive ansatz would be the following: since $\langle Y \rangle = 0$, the elastic part of the potential U^{tot} can be averaged out and the remaining part $U(x_i)$ leads to $c^{\pm} = (k \pm \frac{1}{2})L$ and $b^{\pm} = (k + l \pm \frac{1}{2})L$. But this rather loose approximation is limited to very small κ and thus is of little use.

Nevertheless, both for $\alpha \to 0$ and $\alpha \to 1$, refined asymptotical approximations of the limits can be established. In both cases, we identify $b^{\pm}(x_1)$ with the instantaneous local maximum of $U^{\text{tot}}(x_1, x_2)$ with respect to the variable x_2 for a given value of x_1. Since, in most cases, $\alpha < 1$, the relaxation of the component x_2 then will start toward the accompanying equilibrium closest to $(k + l)\, L$. Therefore, we determine $b^{\pm}(x_1)$ by expanding $\partial U^{\text{tot}}(x_1, x_2) / \partial x_2$ to first order about $x_2 \approx \left(k + l \pm \frac{1}{2}\right) L$ and setting it equal to zero, yielding

$$b^{\pm}(x_1) = \frac{\left(k + l \pm \frac{1}{2}\right) L - \epsilon\,(x_1 + a)}{1 - \epsilon}. \tag{5.22}$$

In a similar manner we wish to determine the basin of attraction of particle x_1 by an effective one-particle potential $\tilde{U}^{\text{tot}}(x_1) = U^{\text{tot}}\big(x_1, \tilde{x}_2(\alpha)\big)$. This must not depend on component x_2 anymore because the integration over x_2 is already completed. Instead of that we introduce a parameter $\tilde{x}_2(\alpha)$ having different meanings in both limits $\alpha \to 0$ and $\alpha \to 1$. In the first case ($\alpha \to 0$), component x_2 becomes frictionless and will immediately relax to its accompanying equilibrium. This adiabatically accompanying equilibrium is found to be

$$\tilde{x}_2\,(\alpha = 0) = \frac{(k + l)\, L + \epsilon\,(x_1 + a)}{1 + \epsilon} \tag{5.23}$$

by expanding $\partial U^{\text{tot}}(x_1, x_2) / \partial x_2$ to first order about $x_2 \approx (k + l)L$ and setting it equal to zero. In the second case ($\alpha \to 1$), the relaxation dynamics of both components proceed on the same time scale. After integrating out the variable x_2, the best estimate we have for $\tilde{x}_2$ is its expectation value in case of x_1 being close to one of its own relative potential maxima at $(k \pm \frac{1}{2})L$. This expectation value is easily calculated to be

$$\tilde{x}_2^{\pm}\,(\alpha = 1) = \iint dx_1\, dx_2\, x_2\, \delta\left[x_1 - \left(k \pm \frac{1}{2}\right) L\right] W(x_1, x_2)\,, \tag{5.24}$$

where the superscript $\pm$ indicates which sign is to be taken at the upper $(+)$ or the lower $(-)$ integration limit.

Now, estimates for the instantaneous boundaries of the basins of attraction for component x_1, denoted by $c_\alpha^{\pm}$, are obtained from an expansion of $\partial \tilde{U}^{\text{tot}}(x_1)/\partial x_1$ at $x_1 \approx (k \pm \frac{1}{2})L$. By using $\tilde{x}_2\,(\alpha = 0)$ within this expansion,

we find

$$c_0^{\pm} = \left(k \pm \frac{1}{2}\right) L + \epsilon \left[\left(-l \pm \frac{1}{2}\right) L + a\right], \tag{5.25}$$

and with $\tilde{x}_2^{\pm}$ $(\alpha = 1)$ that

$$c_1^{\pm} = c_0^{\pm} + \frac{\epsilon}{1+\epsilon} \left[(k+l) L - \tilde{x}_2^{\pm}\right]. \tag{5.26}$$

For intermediate α, we choose a linear interpolation for the whole range $0 \leq \alpha \leq 1$ and obtain

$$c^{\pm}(\alpha) = c_0^{\pm} + \alpha \left(c_1^{\pm} - c_0^{\pm}\right). \tag{5.27}$$

With these boundaries, Eq. (5.21) becomes applicable to all values of α with sufficient accuracy.

At the beginning of a new cycle of driving, the final configuration (k, l) will be mapped onto $(0, m)$, as before. Therefore, we are able to deduce the transition probabilities from initial to final relative distance between components 1 and 2 (*i.e.*, $P_{(0,m)\to(\,\cdot\,,l)}$) via the summation

$$P_{(0,m)\to(\,\cdot\,,l)} = \sum_{k=-\infty}^{\infty} P_{(0,m)\to(k,l)}. \tag{5.28}$$

These transition probabilities correspond to some stationary nontrivial probability distribution P_m with $\sum P_m = 1$ since the matrix elements $P_{(0,m)\to(\,\cdot\,,l)}$ vanish exponentially for large $|l|$ and $|m|$. Thus, a formal solution of

$$\sum_{m=-\infty}^{\infty} \left(P_{(0,m)\to(\,\cdot\,,l)} - \delta_{ml}\right) P_m = 0, \tag{5.29}$$

where δ_{ml} is the Kronecker symbol, determines P_m, which are the probabilities of $(0, m)$ states at the beginning of each driving cycle.

For any finite κ, the average velocity of the dimer must be equal to each $\langle \dot{x}_i \rangle$ according to Eq. (5.5), which by now can be calculated for component x_1 from the transition probabilities $P_{(0,m)\to(k,l)}$. As we are interested in the average shift of x_1 alone, we can first sum over all final l configurations, $\sum_l P_{(0,m)\to(k,l)}$. The next step is to sum over all initial m configurations, where the previously determined probabilities P_m enter. Then, after one period of duration τ, each possible step width kL may occur with the assigned probability $\sum_{l,m} P_m P_{(0,m)\to(k,l)}$. Finally, the average dimer velocity is obtained by means of a threefold summation,

$$v = \frac{L}{\tau} \sum_k k \sum_m P_m \sum_l P_{(0,m)\to(k,l)}, \tag{5.30}$$

where all sums run from $-\infty$ to ∞. The diffusion coefficient according to Eq. (5.6) is obtained from the transition probabilities $P_{(0,m)\to(k,l)}$ in an analogous manner,

$$D = \frac{L^2}{2\tau} \sum_k k^2 \sum_m P_m \sum_l P_{(0,m)\to(k,l)} - \frac{v^2\tau}{2}. \tag{5.31}$$

5.4.2 Strong-coupling approximation

In the limit of strong coupling, the potential landscape is simplified significantly. In the weak-coupling case considered before, there was a broad variety of "frozen" dimer configurations $(0, m)$ in each on-phase, whereas for overcritical κ, there is (in most cases) but a unique equilibrium configuration left. A straightforward but somewhat tedious analysis of the relaxation dynamics on a short time scale leads, for a given ϵ and restricting the rest length a to the interval $[-L/2,\ L/2]$, to the following approximate upper bound

$$|a| < \frac{L}{\pi} \arccos\left(\sqrt{4\epsilon^2+2} - 2\epsilon\right). \tag{5.32}$$

Below this bound, any stretched configuration (*i.e.*, dimer components separated by a potential maximum) is always unstable, thus leaving a single stable minimum for any one given x_i.

A further simplification arises from neglecting variations in the relative coordinate Y because of the decreasing width of its distribution function. Since small deviations from the center of this distribution are completely symmetric, their effect cancels in first-order approximation. Therefore it suffices to derive a single parameter transition probability $P_{(0,0)\to(k,0)}$ for the dimer to move by kL as a whole solely from the central coordinate distribution function $W_1(X)$, Eq. (5.18).

The equilibrium distribution can now be derived by expanding U^{tot} with respect to x_1, not about kL as before but about $kL - a/2$ since this is the correct value in the limit $\epsilon \to \infty$:

$$x_1^{\mathrm{eq}} = kL - \frac{a}{2} + \frac{L}{2\pi} \frac{\sin(\pi a/L)}{2\epsilon + \cos(\pi a/L)} \tag{5.33}$$

and

$$x_2^{\mathrm{eq}} = 2kL - x_1^{\mathrm{eq}}, \tag{5.34}$$

where $\epsilon \gg 1$ (overcritical coupling). The equilibrium central coordinate that follows from these new values still equals $X^{\mathrm{eq}} = \left(x_1^{\mathrm{eq}} + \alpha x_2^{\mathrm{eq}}\right) / (1+\alpha)$, yielding for the transition probability the result

$$P_{(0,0)\to(k,0)} = \int_{d^-(\alpha)}^{d^+(\alpha)} dx_1 \int_{-\infty}^{\infty} dX\, \delta\left(X - x_1 - \frac{\alpha\, a}{1+\alpha}\right) W_1(X). \tag{5.35}$$

Again, we determine the limits of integration, $d^+(\alpha)$ and $d^-(\alpha)$, from the two limiting cases of the asymmetry parameter α. For $\alpha \to 1$, the dimer will settle into that potential well to which its (geometrical) center is the closest. Since we assume $Y \approx 0$, we have $X \approx x_1 + a/2$. The dimer therefore will relax to the minimum at kL for $d_1^- < x_1 < d_1^+$, where

$$d_1^\pm = \left(k \pm \frac{1}{2}\right) L - \frac{a}{2}. \tag{5.36}$$

In the opposite case $\alpha \to 0$, an expansion of U^{tot} about $x_1 = (k \pm \frac{1}{2})L - a/2$ and using $x_1 + x_2 = (k \pm \frac{1}{2})L$ leads to a basin of attraction of minimum kL between

$$d_0^\pm = d_1^\pm + \frac{L}{2\pi} \frac{\sin(\pi a/L)}{2\epsilon - \cos(\pi a/L)}. \tag{5.37}$$

As before, we choose a linear interpolation for $0 \leq \alpha \leq 1$,

$$d^\pm(\alpha) = d_0^\pm + \alpha \left(d_1^\pm - d_0^\pm\right). \tag{5.38}$$

Average dimer velocity and diffusion coefficient follow immediately by adjusting Eqs. (5.30) and (5.31), yielding

$$v = \frac{L}{\tau} \sum_k k P_{(0,0)\to(k,0)} \tag{5.39}$$

and

$$D = \frac{L^2}{2\tau} \sum_k k^2 P_{(0,0)\to(k,0)} - \frac{v^2 \tau}{2}. \tag{5.40}$$

5.5 Results and discussion

To verify the above predictions we compared velocity and diffusion coefficient from Eqs. (5.30) and (5.31) in the case of weak coupling, or Eqs. (5.39) and (5.40) in the case of strong coupling, to numerical simulations of the original Langevin Eq. (5.3). Some parameter values were kept fixed throughout all simulations and scaled to unity: thermal energy $k_B T$, friction coefficient η, and corrugation length L. The barrier height was fixed at $\Delta U = 100\, k_B T = 100$ in order to satisfy assumption (5.9). Also, the duty cycle stayed unaltered, $\tau_{\text{on}}/\tau = 1/2$, dividing the time into equally long on- and off-phases. Each data point resulted from averaging over 100 trajectories with more than 15 000 duty cycles for undercritical and 1 500 for overcritical coupling.

5.5.1 Dependence on dimer length

The symmetries of the total energy U^{tot} naturally depend on the dimer length a through the properties of the elastic part of the potential. Clearly, any U^{tot} and a dependent quantity (*e.g.*, average dimer velocity) must be affected by those fundamental properties, and we shall discuss these effects briefly. Since the interplay of surface and elastic contributions to total energy U^{tot} can only be seen during the on-phases, $f(t) = 1$, we assume time t to have an appropriate constant value. Therefore, within the subsequent discussion the so far t dependence of the potential $U^{\mathrm{tot}} = U^{\mathrm{tot}}(x_1, x_2; t)$ will be abandoned in favor of its dependence on a, *i.e.*, from now on $U^{\mathrm{tot}} = U^{\mathrm{tot}}(x_1, x_2; a)$.

There are three different symmetry transformations applicable to the spatial variables of U^{tot}:

1. translational invariance,
   $U^{\mathrm{tot}}(x_1, x_2; a) = U^{\mathrm{tot}}(x_1 + nL, x_2 + ml; a - nL + mL)$, where $n, m \in \mathbb{Z}$;

2. inversion symmetry, $U^{\mathrm{tot}}(x_1, x_2; a) = U^{\mathrm{tot}}(-x_1, -x_2; -a)$;

3. exchange symmetry, $U^{\mathrm{tot}}(x_1, x_2; a) = U^{\mathrm{tot}}(x_2, x_1; -a)$.

A change from a to $-a$ can be understood as inversion of the dimer's orientation. Necessarily, if the average velocity was nonzero before reorientation, it must be reversed, $v(a) = -v(-a)$. On the one hand, this immediately implies nodes of $v(a)$ at all integer multiples of L due to translation symmetry. On the other hand, translational invariance makes the average velocity a periodic function, $v(a) = v(a + kL)$, where $k \in \mathbb{Z}$. Accordingly, we find $v(L/2) = v(-L/2) = -v(L/2)$, which implies nodes of $v(a)$ at all half integer multiples of L. Therefore, if v is not constantly zero, it must change its sign in each node at any integer multiple of half the corrugation length, $L/2$. The direction of the average current depends on several parameters and will be discussed in the following subsections.

Besides the above mentioned symmetry properties of $v(a)$, Fig. 5.3 includes variations in a further parameter, the driving frequency $\omega = 2\pi/\tau$. Values of ω were chosen from a range well within the bounds imposed by Eqs. (5.10) and (5.11). They yield a succession of increasing amplitudes of v, starting from $\omega = 50$ and ending at $\omega = 100$. The abscissa represents the dimer length a and ranges from $-L/2$ to $L/2$, thus covering a single full period of the odd L-periodic function $v(a)$. Nodes with change in sign appear at each integer multiple of $L/2$, see explanation above. The absolute value of v exhibits maxima at $|a/L| \approx 0.3$. The agreement of theory and simulation within statistical uncertainty is very good for all values depicted.

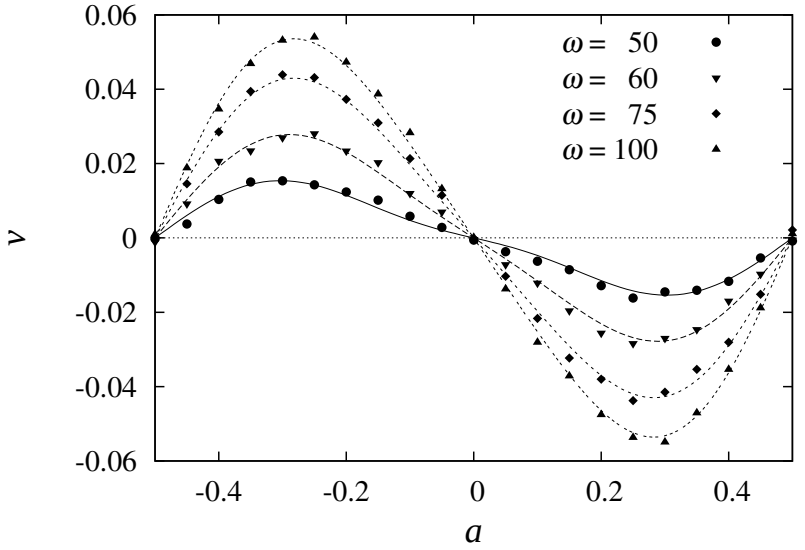

Figure 5.3: Average dimer velocity v vs rest length a at four different values of driving frequency $\omega = 50$ (circles and solid line), 60 (downward triangles and long dashed line), 75 (diamonds and medium dashed line), and 100 (upward triangles and short dashed line), where $k_B T = \eta = L = 1$, $\alpha = 0.3$, $\Delta U = 100$, and $\kappa = 50$. Data points are taken from simulation data, lines show the corresponding theoretical predictions.

5.5.2 Dependence on friction

The linear interpolation [Eq. (5.27)] yields accurate results, as can be seen from Fig. 5.4. Therein, the rest length is a quarter of the spatial period, $a = L/4$, so that velocity $v(a)$ is potentially large. For $\alpha = 1$, which means $\eta_1 = \eta_2$, the equations of motion become completely symmetric and the average current must be zero. For decreasing α, the average velocity increases until it reaches a maximal absolute value at $\alpha \approx 0.3$. Ongoing decrease in α leads to a current reversal at $\alpha \approx 0.07$ and finally to some finite current in the opposite direction for $\alpha \to 0$.

The qualitative behavior of the velocity v can be explained by two antagonistic effects. The first effect depends on the off-phase equilibrium position of the dimer in the deterministic case, see Fig. 5.2. At $\alpha = 1$, the whole situation is symmetric with respect to the surface potential U. A decrease in α leads to a shift in the final position either to the right (A) or to the left (B), as explained above. For a dimer with rest length $L/4$, as it is the case in Fig. 5.4, the shift in B is substantially larger than in A, yielding a negative average velocity.

The second effect depends on the shift in the boundaries of integration, *i.e.*, the friction dependent change in the basins of attraction for each dimer

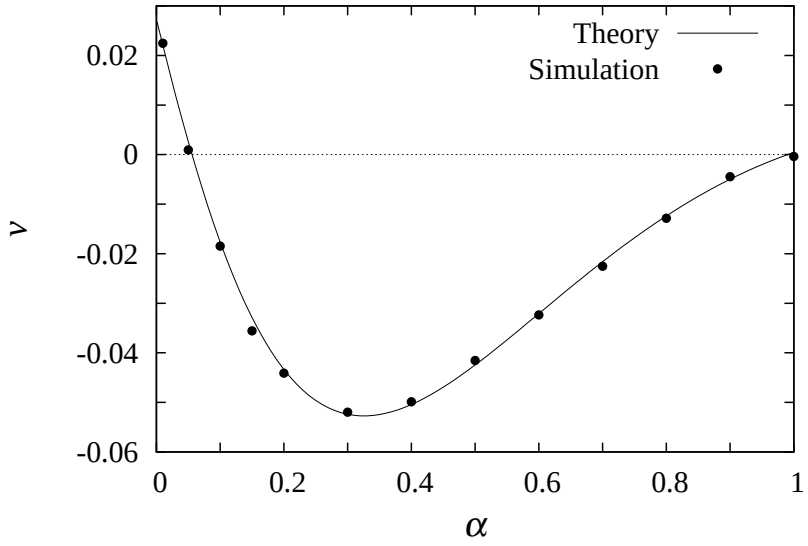

Figure 5.4: Dimer velocity v vs asymmetry parameter α, where $\eta = k_B T = L = 1$, $a = 0.25$, $\Delta U = \omega = 100$, and $\kappa = 50$. For $\alpha = 1$, symmetry is restored and the average current is zero; the limit $\alpha \to 0$ means vanishing friction of dimer component x_2 and gives rise to a current reversal.

component. From simple geometrical reasoning one can deduce that, with $\alpha = 1$ and $l_0 = L/4$, the dimer approximately will end up in A with probability $3/4$ and in B with probability $1/4$. For $\alpha < 1$, the probability to arrive in a B state is reduced because the fast component x_2 may sometimes pull the slow component x_1 over the top of a potential barrier. This results in a drastic enhancement of the transition probability from any A state into the next A state to the right instead of the B state lying in between. Since the B states have a high transition probability to the left A state, jumps to the left are further decreased for low α. Eventually, with $\alpha \to 0$, the second effect becomes dominating and the average velocity turns to positive values.

5.5.3 Dependence on temperature

The vanishing velocity at both extremal temperature limits, see Fig. 5.5, is readily explained. At zero temperature, the only possible motion is the purely deterministic motion between equilibrium positions of on- and off-phases, see Fig. 5.2. This oscillatory motion clearly is bound to a fixed position, generating no net current. At very high temperature, the probability distribution functions of both dimer components become extremely flat. Furthermore, the influence of the surface potential becomes negligible as compared to thermal energy so that the transport generating influence of the driving is substan-

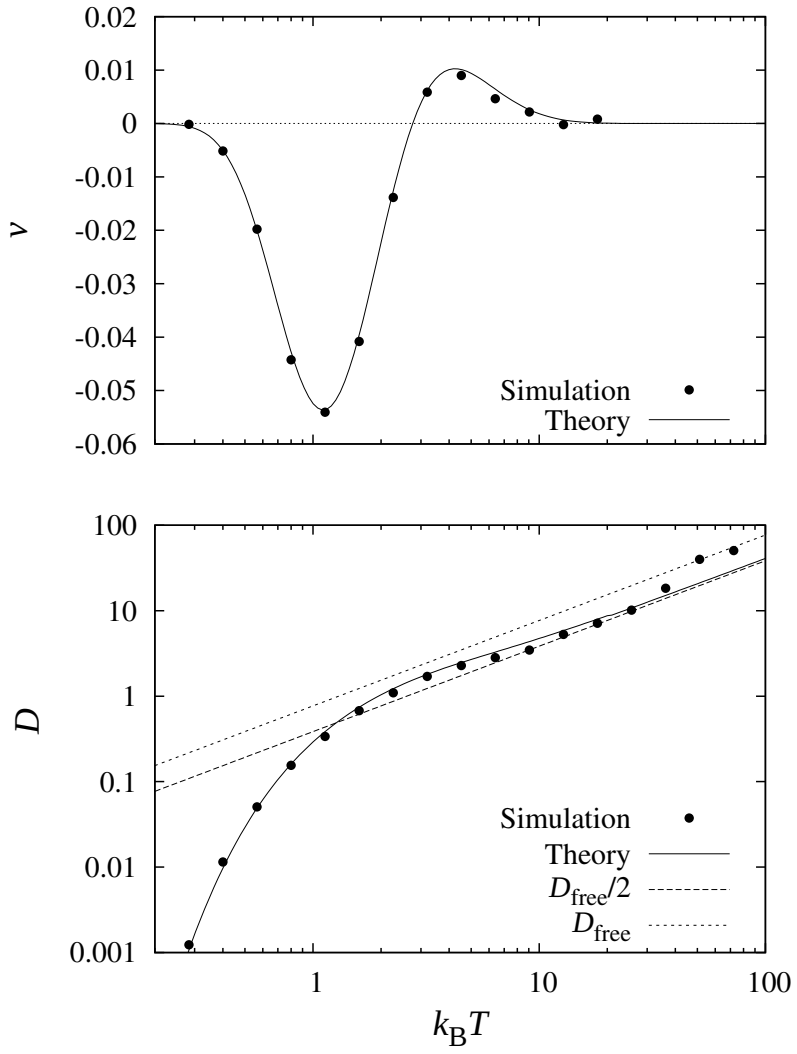

Figure 5.5: Dimer velocity v and diffusion coefficient D vs thermal energy $k_{\text{B}}T$, where $\eta = k_{\text{B}}T = L = 1$, $\alpha = 0.3$, $a = 0.25$, $\Delta U = \omega = 100$, and $\kappa = 50$. Upper graph: The velocity shows two extremal values of opposite sign. Lower graph: The coefficient of free diffusion D_{free}, *i.e.*, dimer diffusion without driving, and $D_{\text{free}}/2$ are depicted in dashed lines, too.

tially reduced.

Everything being of physical interest, *e.g.*, a ratchet effect, is to be found in the intermediate temperature regime about $0.1 < k_\mathrm{B}T < 100$. The pronounced maximum of negative velocity at $k_\mathrm{B}T \approx 1$ and the less prominent maximum of positive velocity at $k_\mathrm{B}T \approx 4$ can be explained similarly to the preceding section. When temperature rises from zero, the width of any final off-phase probability distribution grows and transitions into neighboring states become more probable. As long as temperature is low, those widths are rather narrow meaning that any dimer in a B state will proceed to the left A state with high probability. At higher temperature, the transition from a B state to the A state on the right becomes more and more probable, finally leading to a current reversal. Further reversals at still higher temperature could not be observed because assumption (5.9) is no longer valid.

With regard to the diffusion coefficient, the same temperature ranges reveal different features of the dimer dynamics. For $T \to 0$, the dimer motion becomes subdiffusive since the probability to leave the basin of attraction of a specific state rapidly approaches zero. The free diffusion coefficient of the same dimer but without driving, *i.e.*, with spatially constant surface potential, is $D_\mathrm{free} = k_\mathrm{B}T / (1+\alpha)\,\eta$, which is the diffusion coefficient of Wiener process (5.18). One half of D_free is the respective free diffusion coefficient of a dimer that is "frozen" in place according to the same duty cycle $\tau_\mathrm{on}/\tau = 1/2$ for half of the time but without being relocated to discrete rest positions. At $k_\mathrm{B}T \approx 1$, the diffusion coefficient grows larger than $D_\mathrm{free}/2$, and at $k_\mathrm{B}T \approx 4$ it has grown distinctly beyond this value, marking a local maximum of D/D_free. This corresponds to the appearance of those transitions that lead directly from an A state to the neighboring A state instead of looping between A and B state. Since this happens while transitions in opposite direction are still important, an ensemble of dimers is tuned toward an optimal mixing. At higher temperatures ($5 < k_\mathrm{B}T < 30$) this advantage is counterbalanced by the enhancement of transitions from B to the right A state, as explained above, and the diffusion coefficient declines asymptotically to $D_\mathrm{free}/2$. Finally, for $k_\mathrm{B}T \geq \Delta U$, the diffusion becomes quasi-free and the coefficient D approaches D_free.

5.5.4 Dependence on driving frequency

The frequency dependence is related to the temperature dependence of the dimer dynamics via Eq. (5.18) which has the most decisive influence onto the final result. Therein, thermal energy and duration of the off-phase are multiplied to yield the width of the final probability distribution. For duty cycle $1/2$, this equals to the ratio of thermal energy and driving frequency according to $k_\mathrm{B}T\tau_\mathrm{on} = \pi k_\mathrm{B}T/\omega$. Therefore, one may expect similar results for

variation in ω at fixed $k_\mathrm{B}T$ as one had for variation in $1/k_\mathrm{B}T$ at fixed ω, as long as the assumptions concerning times τ_on and τ_off are respected.

Regarding velocity, this connection is self-evident from Fig. 5.6. Starting at low frequency, velocity grows from zero to a first positive maximal value, corresponding to the positive velocity maximum in Fig. 5.5. Further increase in frequency ω reverts the sign of the net current to a much larger negative velocity, as is the case for decreasing temperature. At even higher frequency, theory disagrees with simulation because assumptions (5.10) and (5.11) concerning the relaxation times of dimer components are no longer complied with. The apparent prediction of a second node in the velocity relation therefore lies outside the range of validity; nevertheless the asymptotical decrease in velocity for very high frequency is correct.

The similarity regarding the diffusion coefficient is not so complete because the barrier surmounting effect of very high temperature can only be imitated by such a low-frequency that the corresponding large driving period τ entering the denominator of Eq. (5.31) cancels everything. Therefore a transition from an asymptotic $D_\mathrm{free}/2$ to a D_free regime for $\omega \to 0$ cannot be observed. Instead, in the low frequency limit analogous to moderately high temperature ($5 < k_\mathrm{B}T < 30$), there is a saturation of the diffusion coefficient at $D_\mathrm{free}/2$. Increasing the frequency leads to a clear maximum of diffusivity, above $D_\mathrm{free}/2$ but still well below D_free. The explanation for this maximum of D/D_free was given in the preceding subsection. This maximum of the diffusion coefficient coincides with the sign reversal of the net current, as well. At high frequency, analogous to low temperature, the time τ_off is not long enough to allow for diffusive escape from one of the discrete "rest" states to which the dimer is periodically confined by the surface potential.

5.5.5 Dependence on elasticity

As we pointed out in the previous section, the approximation scheme we applied to the dimer dynamics prevents us from any proposition concerning $\kappa \approx \kappa_\mathrm{crit}$. This particular shortcoming obviously appears in Fig. 5.7, where there is very good agreement between theory and simulation data in the weak-coupling and the strong-coupling regimes, but not at critical coupling where the average dimer velocity is maximized. At this point, both approximations fail completely.

The reasons for the asymptotic behavior of v for weak and strong coupling are clear. In the uncoupled limit ($\kappa \to 0$), the dimer resolves into two independent particles, each in a symmetric potential that does not yet allow for unidirectional motion. Neither is there any net transport possible in the rigid coupling limit ($\kappa \to \infty$) because in this case the dynamics can be reduced to the Brownian motion of a single particle (*e.g.*, center of mass) in a symmetric

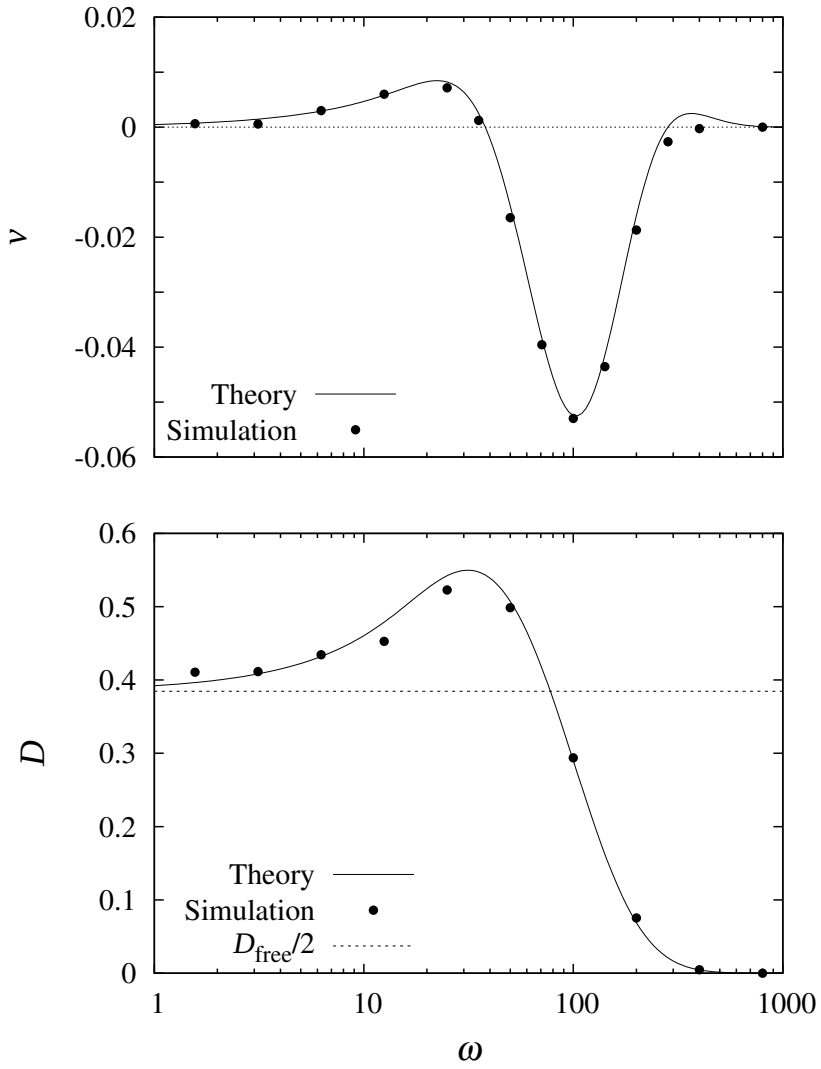

Figure 5.6: Dimer velocity v and diffusion coefficient D vs driving frequency $\omega = 2\pi/\tau$, where $\eta = k_B T = L = 1$, $\alpha = 0.3$, $l_0 = 0.25$, $\Delta U = 100$, and $\kappa = 50$. Upper graph: The velocity shows two extremal values of opposite sign. The similarity to v as a function of $1/k_B T$ is striking. Lower graph: The maximum of diffusion coincides with the low-ω maximum of v.

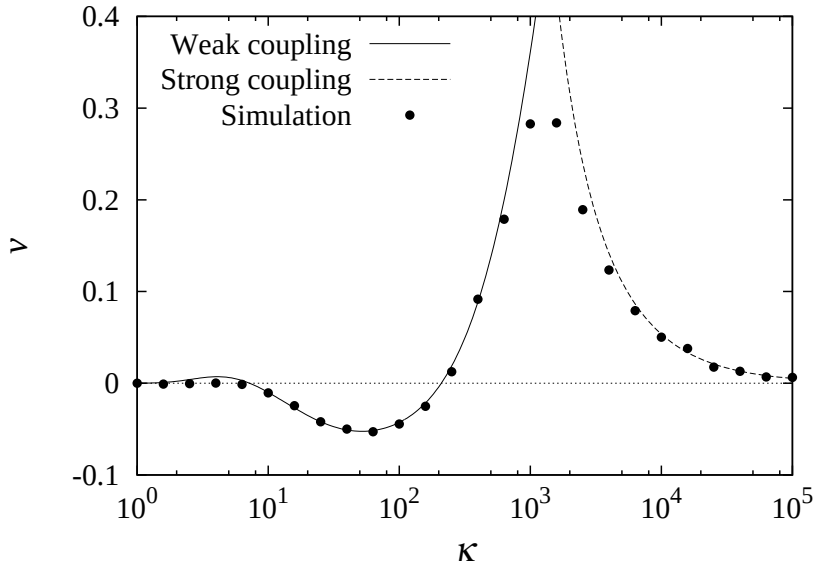

Figure 5.7: Dimer velocity v vs elasticity κ, where $\eta = k_B T = L = 1$, $\alpha = 0.3$, $a = 0.25$, and $\Delta U = \omega = 100$. Weak and strong coupling approximations are in good accordance with simulation data over several orders of magnitude of the coupling strength κ. Only at critical coupling, $\kappa_{\text{crit}} \approx 2\,000$, both approximations fail. In the weak-coupling limit, the average velocity v converges to infinitely small *negative* values, whereas the approximation suggests a small *positive* velocity. This is an artifact due to incomplete relaxation of the dimer that was not accounted for.

periodic potential. The small positive velocity visible at $\kappa < 10$ is a mere artifact. It occurs because assumption (5.11) concerning the relaxation time in the off-phase is violated. If it was desirable to remedy this situation, the stationary probability distribution $W(Y)$ could be replaced by its non-stationary representation.

The internal degree of freedom, Y, becomes physically relevant for finite elasticity only. Similarly to the two preceding subsections, the average velocity possesses two extremal values with different sign. The low-κ maximum (in negative direction) is captured by the weak-coupling approximation, whereas its high κ counterpart (in positive direction) coincides with the critical coupling strength. Anyway, both approximations enclose this maximum very tight so that one can easily do without a precise theoretical prediction at κ_{crit}.

Unlike all former results, the maximal velocity in positive x direction is about six times larger than its negative counterpart. There are several reasons for this: the probability of reaching a B state (cf. Fig. 5.2) with its relaxation into negative direction is diminished because the fast component x_2 can more rigidly pull the slow component x_1 over a potential barrier top. Furthermore,

the maximal displacement of A states is increased whereas that of B states is decreased with increasing κ. Last but not least, with further increasing coupling strength, B states become unstable so that the probability for traveling backward is reduced largely. Therefore, the effect onto the average dimer velocity is by far larger than it was with all previously varied parameters.

5.6 Concluding remarks

We have investigated the one-dimensional overdamped Brownian motion of a dimer whose elastically coupled components differ in their friction coefficients and are located in a flashing sinusoidal potential. Approximations for the average velocity and diffusion coefficient have been obtained for wide ranges of parameter values, yielding precise theoretical predictions as compared to numerical simulations of the Langevin dynamics. Ratcheting motion has been observed and explained upon variation in rest length, temperature, frictional asymmetry, driving frequency and elasticity. In each case two parameter values have been found that optimize the velocity, either in positive or in negative direction. For the two most relevant parameters—temperature and frequency— the characteristics of the effective diffusion coefficient have been obtained.

Regarding the relevance for atomic-scale friction, these results can, in principle, be considered in the same way as before (see section 4.6). Admittedly, there is a certain difficulty involved to find appropriate materials. Those must have a relatively simple structure that can be modeled as a dimer and, at the same time, a complex dynamics because they must possess different friction coefficients. Although the required asymmetry in dissipation is, in the first instance, a *quantitative* aspect, it clearly can only be generated by a *qualitative* disparity between the two interacting components to produce a large enough difference in friction. A problem arises if one wants to produce the necessary qualitative difference directly within the components. This can only be obtained by a sufficiently complex internal structure as one can observe in motor molecules like kinesin or myosin. This means, in turn, that the appropriate samples are likely composed of small, separate units and not geometrically extended, as would be helpful for AFM manipulation. Or they are geometrically extended but their complex internal structure prevents us from simplifying them, in a minimalist model, to a dimer. However, any new results offering means and ways to overcome this dilemma and to refute the author's overcautious attitude are very welcome.

A more promising alternative is not to produce AFM tips that form multicontacts through different kinds of asperities, which probably is hardly possible at all, but instead to design a specially suited surface. A hot candidate for this is a silicon p–n junction (*cf*. Fig. 1.14) like it was used by Park and

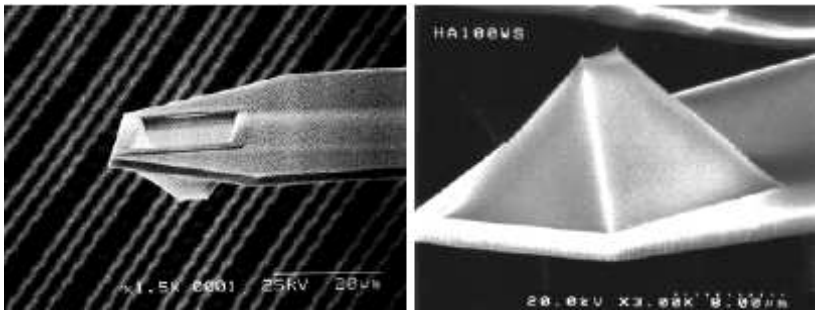

Figure 5.8: A low wear AFM tip produced by Olympus Co. (Japan) with two protrusions of *ca*. 10nm radius. Picture from the producer's internet site.

co-workers in their friction experiment [66]. A surface patterned with strips of p- and n-doted silicon could produce two different regimes of friction and thus break friction symmetry. The experiment could be operated by using either a multi-cantilever device like the Millipede (*cf*. Fig. 3.1) or, in a smaller version, an AFM cantilever with a twin tip, see Fig. 5.8. The latter may indeed be applied very nicely to verify the theoretically predicted ratchet effect and further to inquire its usability as a means of atomic-scale friction control.

6 Summary and Conclusions

What most experimenters take for granted
before they begin their experiments
is infinitely more interesting than any results
to which their experiments lead.

Norbert Wiener

Until less than a hundred years ago, the research of friction has first and foremost been a material science. Engineers and technicians have been diligently collecting friction coefficients of all materials being in use, with and without various lubricants. It goes without saying that filling technical data sheets is a very useful task with regard to technical advancement and industrial benefits. But, according to Leonardo, a thorough analysis of the *ragione* behind the natural effect of friction could not be achieved in this way. Asking with Wiener, what are the basic principles of friction that were taken for granted so long, has been a question hard to answer before the experimental accessability of molecular and even atomic dynamics was established. Today, we are in a position not only to ask questions about friction in a more sophisticated manner, but also to find at least some clarifying answers in experiment.

The centerpiece of this thesis is the crossover of nanotribology and Brownian motion for those systems that possess an internal interaction which substantially influences the dynamics of the whole system. One aspect of Brownian motion, the role thermal activation can play, is the object of current research on stick–slip motion and atomic-scale friction of single asperities. Another aspect of Brownian motion consists of the more complex phenomena that arise in systems out of thermal equilibrium treated herein. What this thesis aspires to is to elucidate the possibility of non-equilibrium phenomena, especially the ratchet effect, in the context of nanotribology. It does so by concentrating on minimalist models that are concerned with the dynamics of coupled particle chains and, in particular, dimers on a crystal surface.

For the sake of simplicity, the model systems under consideration were chosen one-dimensional, *i.e.*, each particle is fully described by a single coordinate. This simplification was shown to be justified because, in a pulling

experiment where the FFM tip moves across a crystal surface or it moves a nanoparticle across it, the main direction of motion is firmly imposed onto the nanocontact by the relative motion of cantilever and sample stage. The two-dimensional geometry of the surface potential can be split into the direction parallel to the imposed pulling path and its orthogonal complement. The one-dimensional model thus can be seen as the projection of the full potential onto the parallel direction, whereas the direction orthogonal to the pulling path can, in a rough estimate, be neglected to a large extent. As we desired a qualitative exploration, we left the models one-dimensional. For a meaningful comparison to experimental results, more effort is necessary to incorporate the two-dimensional corrections.

Since minimalist models arise in many different fields of research (*e.g.*, diffusion of dimers on surfaces, molecular motors, DNA translocation through nanopores, *etc.*), they are presented in a generic form, meaning that they were originally not limited to a distinct area like nanotribology. Instead, the familiar quantities that usually describe the dynamical response of a many particle system, *i.e.*, the average velocity and the diffusion coefficient, are connected to the relevant quantities of an atomic-scale friction experiment which are the mobility (force–velocity relation) and the moments of the waiting time distribution for slip events.

The connection between the diffusion coefficient and the second moment of the waiting time distribution has been established qualitatively via plausibility considerations. The connection between the average velocity of the statistical models and the experimentally measured mobility is more obvious—the decisive relation is encoded in the $F(v)$- or $v(F)$-curve. To show that the two different *modi operandi* (pulling with constant velocity *vs.* pulling with constant force) are comparable is a little bit more intricate. It was established under certain assumptions regarding the stiffness of the cantilever.

Throughout this thesis, it is the same geometrical property of the systems under consideration that attracts most of our attention: the interplay of the dimer (or polymer) rest length with the corrugation length of the surface potential. For chains of interacting particles, the existence of cooperative effects was shown. In case of incommensurate rest length and lattice constant, the idealized springs between the particles (harmonic coupling) serve as storages for potential energy and thereby facilitate the surmounting of the individual surface potential barriers. For dimers, a high sensitivity of the ratchet effect was shown to be due to the namely geometric ratio. In this case, the energy storage function of the internal DOF is decisive for the emergence of the ratchet effect, whereas symmetry reasons (comparable to commensurability) lead to its overall suppression.

The influence of the control parameters temperature/noise level, driving frequency, and spring constant/coupling strength was studied with extensive numerical simulations. The numerical results were compared to the

predictions derived from the analytical models based on the Langevin equations of the model systems. These showed a fair to excellent agreement and thereby justified the underlying assumptions and approximations.

Concluding remarks to each of the chapters 3 through 5 named possible (or, at least, thinkable) experimental applications, mainly AFM studies that in the first instance may show whether the proclaimed effects (a) do exist at all and (b) do really contribute to atomic-scale friction. Furthermore, a positive detection of ratcheting motion in coupled asperities or cantilevers opens new perspectives to control friction effectively on the atomic level. The most impressive outcome would be an experimental verification of either of the following two: the multi-peaked structure of the velocity and waiting time dispersion of multi-contacts, or the ratchet effect for a dimer with broken friction symmetry, as pointed out in section 5.6.

Progress in nanotribology can certainly not be achieved without properly incorporating the Brownian motion that governs the single- and multi-asperity contact dynamics. We are convinced that any *Theory of friction* aiming at completeness will not come without a good portion of non-equilibrium statistical mechanics.

ZUSAMMENFASSUNG

Die vorliegende Dissertation behandelt minimale stochastische Modelle im Überlappungsbereich von atomarer Reibung und Nichtgleichgewichts-Phänomenen der Brown'schen Molekularbewegung. Der thematische Schwerpunkt liegt dabei auf der Untersuchung von dynamischen Effekten in Zwei- und Mehrteilchen-Systemen, in denen thermische Aktivierung und gegenseitige Kopplung die entscheidende Rolle spielen. Insbesondere der sogenannte Ratschen-Effekt wird am Beispiel des Dimers eingehend untersucht. Die erforderliche Symmetriebrechung wird (a) durch unterschiedliche Bindung an das Oberflächen-Potenzial, (b) durch unterschiedliche Reibungskoeffizienten der beiden Dimer-Komponenten erreicht.

Neben der approximativen analytischen Ausarbeitung der zugrunde liegenden Langevin-Dynamik finden umfangreiche numerische Simulationen der betrachteten Ensembles ihre Berücksichtigung. Wichtige Resultate sind

- die durch mehrfache Extrema gekennzeichneten Kurven für mittlere Geschwindigkeit und Diffusionskoeffizient einer Teilchenkette im gekippten periodischen Potenzial,
- der Nachweis des Ratschen-Effektes mit Hilfe von Computer-Simulationen und die detaillierte Erklärung seines Zustandekommens sowie
- mehrere Möglichkeiten der Maximierung des durch den Ratschen-Effekt erzeugten Transportes über verschiedene Kontroll-Parameter.

Ferner finden sich Vorschläge zu möglichen oder in näherer Zukunft denkbaren experimentellen Überprüfungen der theoretischen Resultate.

Diese Dissertation beruht auf folgenden Veröffentlichungen:

1. Sebastian von Gehlen, Mykhaylo Evstigneev und Peter Reimann, *Dynamics of a dimer in a symmetric potential: Ratchet effect generated by an internal degree of freedom*, Physical Review E **77**, 031136 (2008).
2. Mykhaylo Evstigneev, Sebastian von Gehlen und Peter Reimann, *Interaction-controlled Brownian motion in a tilted periodic potential*, Physical Review E **79**, 011116 (2009).
3. Sebastian von Gehlen, Mykhaylo Evstigneev und Peter Reimann, *Ratchet effect of a dimer with broken friction symmetry in a symmetric potential*, Physical Review E **79**, 031114 (2009).

Übersetzung der Zitate

Kapitel 1

> Reibung ist keine Materialeigenschaft, sondern eine Systemantwort.
>
> Bharat Bhushan

Kapitel 2

> Eine Intelligenz, die, zu einem gegebenen Zeitpunkt, alle Kräfte wüsste, welche die Natur beleben, und die jeweilige Lage der Dinge, aus denen diese besteht, wenn sie außerdem umfassend genug wäre um diese Gegebenheiten einer Analyse zu unterziehen, die in derselben Formel die Bewegungen der größten Körper des Universums und jene der leichtesten Atome umfasste: Nichts bliebe ihr ungewiss und das Zukünftige wie das Vergangene wäre vor ihren Augen gegenwärtig.
>
> Pierre Simon de Laplace

Kapitel 3

> Die Gesetze der Thermodynamik, wie sie empirisch festgestellt wurden, bringen das näherungsweise und wahrscheinliche Verhalten von Systemen einer großen Zahl von Teilchen zum Ausdruck, oder, genauer, sie bringen die Gesetze der Mechanik für solche Systeme zum Ausdruck, wie sie Lebewesen erscheinen, die nicht die Feinheit der Wahrnehmung besitzen, die es ihnen ermöglichte, Größen von einer derartigen Größenordnung abzuschätzen wie jene, die sich auf einzelne Teilchen beziehen, und die ihre Experimente nicht oft genug wiederholen können, als dass sie irgendwelche außer den wahrscheinlichsten Ergebnissen erzielten.
>
> Josiah Williard Gibbs

Kapitel 4

> Es gibt keine Wirkung in der Natur ohne Ursache; verstehe die Ursache und du brauchst kein Experiment.
>
> Leonardo da Vinci

Kapitel 6

> Was die meisten Experimentatoren als gegeben annehmen, bevor sie ihre Experimente beginnen, ist unendlich viel interessanter als irgendeines der Ergebnisse, zu denen ihre Experimente führen.
>
> Norbert Wiener

Danksagung

Mein ausdrücklicher Dank gilt den folgenden Personen und Institutionen:

- Prof. Dr. Peter Reimann, für die Betreuung meiner Dissertation und für das erfolgreiche Einwerben der Drittmittel für meine Promotionsstelle;
- Prof. Dr. Jürgen Schnack, für seine Bereitschaft, sich als zweiter Gutachter mit dem vorliegenden Konvolut auseinander zu setzen;
- Dr. Mykhaylo Evstigneev, für die vielen wissenschaftlichen und inspirierenden Diskussionen sowie für die regelmäßige Nachfrage "*Sebastiano, how is your thesis going?*"
- Hanne Litschewsky als "Mutter der Kompanie", die mit höchster Effizienz alles notwendige für die Arbeitsgruppe erledigt, was man *nicht* in physikalischen Gleichungen ausdrücken kann;
- allen weiteren Mitgliedern der Arbeitsgruppe "Theorie der kondensierten Materie", für das angenehme Arbeitsklima und den freundschaftlichen Umgang;
- allen nicht namentlich genannten Begleitern, Lehrern und Gefährten, die meinen Lebensweg mitgeprägt und ihn positiv beeinflusst haben;
- der Deutschen Forschungsgemeinschaft, für die Finanzierung meiner Stelle als wissenschaftlicher Mitarbeiter.

Die unendliche Geduld, Hoffnung und Liebe, mit der mich meine Eltern, meine Schwiegereltern und ganz besonders meine Frau begleitet haben und noch immer begleiten, lassen sich kaum in schlichte Dankesworte fassen. Ich hoffe stattdessen, die unendliche Geduld, Hoffung und Liebe so gut es geht zu erwidern und für Maximilian ein guter Vater zu sein.

BIBLIOGRAPHY

[1] B. Bhushan, J. N. Israelachvili, and U. Landman, *Nanotribology: friction, wear and lubrication at the atomic scale*, Nature **374**, 607 (1995).

[2] M. Urbakh, J. Klafter, D. Gourdon, and J. N. Israelachvili, *The nonlinear nature of friction*, Nature **430**, 525 (2004).

[3] M. Müser, *How static is static friction?* Proceedings of the National Acadamy of Sciences of the USA **105**, 13187 (2008).

[4] R. W. Carpick and R. Salmeron, *Scratching the surface: Fundamental investigations of tribology with atomic force microscopy*, Chemical Review **97**, 1163 (1997).

[5] F. L. Griffith, P. E. Newberry, and G. W. Fraser, *El Bersheh: Part I*, Archeological Survey of Egypt, Egyptian Exploration Fund (1893).

[6] B. N. J. Persson, *Sliding Friction: Physical Principles and Applications*, second edition, Springer (2000).

[7] C. M. Mate, *Tribology on the Small Scale: A Bottom Up Approach to Friction, Lubrication and Wear*, Oxford University Press (2008).

[8] M. H. Müser, L. Wenning, and M.O. Robbins, *Simple Microscopic Theory of Amontons's Laws for Static Friction*, Physical Review Letters **86**, 1295 (2000).

[9] F. P. Bowden and D. Tabor, *The Friction and Lubrication of Solids*, reprint, Clarendon Press, Oxford (1986).

[10] J. A. Greenwood and J. B. P. Williamson, *Contact of Nominally Flat Surfaces*, Proceedings of the Royal Society of London, Series A, Mathematical and Physical Sciences **295**, 300 (1966).

[11] G. Binnig and H. Rohrer, *In Touch with Atoms*, Reviews of Modern Physics **71**, S324 (1999).

[12] G. Binnig and H. Rohrer, *Scanning Tunneling Microscopy—from Birth to Adolescence* (Nobel Lecture), *Les Prix Nobel 1986*, p. 85, The Nobel Foundation, Stockholm (1987); Reprinted in Revies of Modern Physics **59**, 615 (1987).

[13] G. Binnig, C. F. Quate, and Ch. Gerber, *Atomic Force Microscope*, Physical Review Letters **56**, 930 (1986).

[14] C. M. Mate, G. M. McClelland, R. Erlandsson, and S. Chiang, *Atomic-Scale Friction of a Tungsten Tip on a Graphite Surface*, Physical Review Letters **59**, 1942 (1987).

[15] J. Krim and A. Widom, *Damping of a crystal oscillator by an adsorbed monolayer and its relation to interfacial viscosity*, Physical Review B **38**, 12 184 (1988).

[16] J. Krim, D. H. Solina, and R. Chiarello, *Nanotribology of a Kr monolayer: A quartz-crystal microbalance study of atomic-scale friction*, Physical Review Letters **66**, 181 (1991).

[17] J. N. Israelachvili and D. Tabor, *The measurement of van der Waals dispersion forces in the range* 1.5 *to* 130nm, Proceedings of the Royal Society of London, Series A, Mathematical and Physical Sciences **331**, 19 (1972).

[18] L. Prandtl, *Ein Gedankenmodell zur kinetischen Theorie der festen Körper*, Zeitschrift für angewandte Mathematik und Mechanik **8**, 85 (1928).

[19] G. A. Tomlinson, *A molecular theory of friction*, Philosophical Magazine S. 7 **7**, 905 (1929).

[20] M. Evstigneev and P. Reimann, *A refined force–velocity relation in friction force spectroscopy experiments*, Physical Review B **73**, 113401 (2006);
Velocity dependence of atomic friction: Rate theory and beyond, in: *Fundamentals of Friction and Wear*, edited by E. Gnecco and E. Meyer, Springer (2007).

[21] O. K. Dudko, A. E. Filippov, J. Klafter, and M. Urbakh, *Dynamic force spectroscopy: a Fokker–Planck approach*, Chemical Physics Letters **352**, 499 (2002).

[22] H. Risken, *The Fokker–Planck Equation: Methods of Solution and Applications*, second edition, Springer, Berlin (1996).

[23] O. M. Braun, A. G. Naumovets, *Nanotribology: Microscopic mechanisms of friction*, Surface Science Reports **60**, 79 (2006).

[24] K. L. Johnson and J. Woodhouse, *Stick–slip motion in the atomic force microscope*, Tribology Letters **5**, 155 (1998).

[25] B. Luan and M. O. Robbins, *Effect of ineratia and elasticity on stick–slip motion*, Physical Review Letters **93**, 036105 (2004);
The breakdown of continuum models for mechanical contacts, Nature **435**, 929 (2005).

[26] Y. I. Frenkel and T. A. Kontorova, *On the theory of plastic deformation and twinning*, Journal of Physics of the USSR **13**, 1 (1938);
T. A. Kontorova and Y. I. Frenkel, Zhurnal Eksperimental'noi i Teoreticheskoi Fiziki **8**, 89 (1939).

[27] S. Aubry, *The twist map, the extended Frenkel–Kontorova model and the devil's staircase*, Physica D **7**, 240 (1983).

[28] G. M. McClelland, *Friction at weakly interacting interfaces*, in: *Adhesion and Friction*, edited by M. Grunze and H. Kreuzer, Springer, Berlin (1989).

[29] M. Hirano and K. Shinjo, *Atomistic locking and friction*, Physical Review B **41**, 11 837 (1990).

[30] K. Shinjo and M. Hirano, *Dynamics of friction: superlubric state*, Surface Science **283**, 473 (1993).

[31] M. Dienwiebel, G. S. Verhoeven, N. Pradeep, J. W. M. Frenken, J. A. Heimberg, and H. W. Zandbergen, *Superlubricity of graphite*, Physical Review Letters **92**, 126101 (2004).

[32] T. Zijlstraa, J. A. Heimberg, E. van der Drift, D. Glastra van Loon, M. Dienwiebel, L. E. M. de Groot, and J. W. M. Frenken, *Fabrication of a novel scanning probe device for quantitative nanotribology*, Sensors and Actuators A: Physical **84**, 18 (2000).

[33] D. Dietzel, C. Ritter, T. Mönninghoff, H. Fuchs, A. Schirmeisen, and U. D. Schwarz, *Frictional duality observed during nanoparticle sliding*, Physical Review Letters **101**, 125505 (2008).

[34] M. H. Müser, *Structural lubricity: Role of dimension and symmetry*, Europhysics Letters **66**, 97 (2004).

[35] M. H. Müser, M. Urbakh, and M. O. Robbins, *Statistical mechanics of static and low-velocity kinetic friction*, Advances in Chemical Physics **126**, 187 (2003).

[36] A. Socoliuc, R. Bennewitz, E. Gnecco, and E. Meyer, *Transition from Stick–Slip to Continuous Sliding: Entering a New Regime of Ultralow Friction*, Physical Review Letters **92**, 134301 (2004).

[37] P. Steiner, R. Roth, E. Gnecco, A. Baratoff, S. Maier, T. Glatzel, and E. Meyer, *Two-dimensional simulation of superlubricity on NaCl and highly oriented pyrolytic graphite*, Physical Review B **79**, 045414 (2009).

[38] E. Gnecco, S. Maier, and E. Meyer, *Superlubricity of dry nanocontacts*, Journal of Physics: Condensed Matter **20**, 354004 (2008).

[39] B. Bhushan and J. Ruan, *Atomic-scale friction measurements using friction force microscopy: Part II—Application to Magnetic Media*, Journal of Tribology **116**, 389 (1994);
B. Bhushan, *Atomic-scale and microscale friction studies of graphite and diamond using friction force microscopy*, Journal of Applied Physics **76**, 5022 (1994);
V. N. Koinkar and B. Bhushan, *Effect of scan size and surface roughness on microscale friction measurements*, Journal of Applied Physics **81**, 2472 (1997).

[40] B. Bhushan, *Nanotribology and nanomechanics*, Wear **259**, 1507 (2005).

[41] S. Sundararajan and B. Bhushan, *Topography-induced contributions to friction forces measured using an atomic force/friction force microscope*, Journal of Applied Physics **88**, 4825 (2000).

[42] E. Gnecco and E. Meyer (Editors), *Fundamentals of Friction and Wear on the Nanoscale* (Nanoscience and Technology), Springer (2007).

[43] B. Bhushan, *Introduction to Tribology*, Wiley (2002).

[44] B. Bhushan (Editor), *Nanotribology and Nanomechanics: An Introduction*, second edition, Springer (2008).

[45] M. Nosonovsky and B. Bhushan, *Multiscale Dissipative Mechanisms and Hierarchical Surfaces: Friction, Superhydrophobicity, and Biomimetics* (Nanoscience and Technology), Springer (2008).

[46] I. L. Singer, *Friction and energy dissipation at the atomic scale: A review*, Journal of Vacuum Science and Technology A **12**, 2605 (1994).

[47] M. O. Robbins and M. H. Müser, *Computer simulations of friction, lubrication and wear*, in: *Modern Tribology Handbook*, editet by B. Bhushan, CRC Press (2001).

[48] E. Gnecco, R. Bennewitz, T. Gyalog, and E. Meyer, *Friction experiments on the nanometre scale*, Journal of Physics: Condensed Matter **13** R619 (2001).

[49] I. Szlufarska, M. Chandross, and R. W. Carpick, *Recent advances in single-asperity nanotribology* Journal of Physics D: Applied Physics **41**, 123001 (2008).

[50] P. Reimann and M. Evstigneev, *Nonmonotonic velocity dependence of atomic friction*, Physical Review Letters **93**, 230802 (2004).

[51] M. Evstigneev and P. Reimann, *Rate Description in Friction Force Microscopy*, Europhysics Letters **67**, 907 (2004).

[52] M. Evstigneev and P. Reimann, *Rate Description of the Stick–Slip Motion in Friction Force Microscopy Experiments*, Physical Review E **71**, 056119 (2005).

[53] P. Reimann and M. Evstigneev, *Description of Atomic Friction as Forced Brownian Motion*, New Journal of Physics **7**, 25 (2005).

[54] M. Evstigneev, A. Schirmeisen, L. Jansen, H. Fuchs, and P. Reimann, *Force Dependence of Transition rates in Atomic Friction*, Physical Review Letters **97**, 240601 (2006).

[55] M. Evstigneev, A. Schirmeisen, L. Jansen, H. Fuchs, and P. Reimann, *Contact ageing in atomic friction*, Journal of Physics: Condensed Matter **20**, 354001 (2008).

[56] T. Bouhacina, J. P. Aimé, S. Gauthier, D. Michel, and V. Heroguez, *Tribological behavior of a polymer grafted on silanized silica probed with a nanotip*, Physical Review B **56**, 7694 (1997).

[57] O. K. Dudko, A. E. Filippov, J. Klafter, and M. Urbakh, *Dynamic force spectroscopy: a Fokker–Planck approach*, Chemical Physics Letters **352**, 499 (2002).

[58] Y. Sang, M. Dubé, and M. Grant, *Thermal Effects on Atomic Friction*, Physical Review Letters **87**, 174301 (2001).

[59] C. Fusco and A. Fasolino, *Velocity dependence of atomic-scale friction: A comparative study of the one- and two-dimensional Tomlinson model*, Physical Review E **71**, 045413 (2005).

[60] O. Zwörner, H. Hölscher, U. D. Schwarz, and R. Wiesendanger, *The velocity dependence of frictional forces in point-contact friction*, Applied Physics A **66**, S263 (1998).

[61] E. Gnecco, R. Bennewitz, T. Gyalog, Ch. Loppacher, M. Bammerlin, E. Meyer, and H.-J. Güntherodt, *Velocity Dependence of Atomic Friction*, Physical Review Letters **84**, 1172 (2000).

[62] E. Riedo, E. Gnecco, R. Bennewitz, E. Meyer, and H. Brune, *Interaction Potential and Hopping Dynamics Governing Sliding Friction*, Physical Review Letters **91**, 084502 (2003);

E. Riedo and E. Gnecco, *Thermally activated effects in nanofriction*, Nanotechnology **15**, S288 (2004).

[63] S. Y. Krylov, K. B. Jinesh, H. Valk, M. Dienwiebel, and J. W. M. Frenken, *Thermally induced suppression of friction at the atomic scale*, Physical Review E **71**, 065101(R) (2005).

[64] Z. Tshiprut, A. E. Filippov, and M. Urbakh, *Tuning Diffusion and Friction in Mocroscopic Contacts By Mechanical Excitations*, Physical Review Letters **95**, 016101 (2005).

[65] S. Jeon, T. Thundat, and Y. Braiman, *Effect of narmal vibration on friction in the atomic force experiment*, Applied Physics Letters **88**, 214102 (2006).

[66] R. W. Carpick, *Controlling Friction*, Science **313**, 184 (2006);
J. Y. Park, D. F. Ogletree, P. A. Thiel, and M. Salmeron, *Electronic Control of Friction in Silicon pn Junctions*, Science **313**, 186 (2006);
A. Socoliuc, E. Gnecco, S. Maier, O. Pfeiffer, A. Baratoff, R. Bennewitz, and E. Meyer, *Atomic-scale Control of Friction by Actuation of Nanometer-Sized Contacts*, Science **313**, 207 (2006).

[67] S. Maier, Y. Sang, T. Filleter, M. Grant, and R. Bennewitz, *Fluctuations and jump dynamics in atomic friction experiments*, Physical Review B **72**, 245418 (2005).

[68] S. Y. Krylov, J. A. Dijksman, W. A. van Loo, and J. W. M. Frenken, *Stick–Slip Motion in Spite of a Slippery Contact: Do We Get What We See in Atomic Friction?*, Physical Review Letters **97**, 166103 (2006);
D. G. Abel, S. Y. Krylov, and J. W. M. Frenken, *Evidence for Contact Delocalization in Atomic Scale Friction*, Physical Review Letters **99**, 166102 (2007);
S. Y. Krylov and J. W. M. Frenken, *The crucial role of temperature in atomic scale friction*, Journal of Physics: Condensed Matter **20**, 354003 (2008);
K. B. Jinesh, S. Y. Krylov, H. Valk, M. Dienwiebel, and J. W. M. Frenken, *Thermolubricity in atomic-scale friction*, Physical Review B **78**, 155440 (2008).

[69] Z. Tshiprut, A. E. Filippov, and M. Urbakh, *Effect of tip flexibility on stick–slip motion in friction force microscopy experiments*, Journal of Physics: Condensed Matter **20**, 354002 (2008).

[70] O. M. Braun and M. Peyrard, *Modeling Friction on a Mesoscale: Master Equation for the Earthquakelike Model*, Physical Review Letters **100**, 125501 (2008).

[71] A. Einstein, *Über die von der molekularkinetischen Theorie der Wärme geforderte Bewegung von in ruhenden Flüssigkeiten suspendierten Teilchen*, Annalen der Physik **17**, 549 (1905);
Zur Theorie der Brownschen Bewegung, Annalen der Physik **19**, 371 (1906).

[72] C. W. Gardiner, *Handbook of Stochastic Methods*, third edition, Springer (2004).

[73] R. L. Stratonovich, Radiotekh. Elektron. (Moscow), **3**, 497 (1958);
English translation in: *Non-linear Transformations of Stochastic Processes*, edited by P. I. Kuznetsov, R. L. Stratonovich, and V. I. Tikhonov, Pergamon, Oxford (1965).

[74] P. Reimann, C. Van den Broeck, H. Linke, P. Hänggi, J. M. Rubi, and A. Pérez-Madrid, *Giant Acceleration of Free Diffusion by use of Tilted Periodic Potentials*, Physical Review Letters **87**, 010602 (2001);
Diffusion in tilted periodic potentials: Enhancement, universality, and scaling, Physical Review E **65**, 031104 (2002).

[75] P. Reimann, *Brownian motors: noisy transport far from equilibrium*, Physics Reports **361**, 57 (2002).

[76] M. Smoluchowski, *Experimentell nachweisbare, der üblichen Thermodynamik widersprechende Molekularphänomene*, Physikalische Zeitschrift **13**, 1069 (1912).

[77] R. P. Feynman, *The Feynman Lectures on Physics*, Vol. 1, Addison–Wesley (1963).

[78] The Japanese Wikipedia, *Brownian ratchet*,
http://ja.wikipedia.org/wiki/%E3%83%96%E3%83%A9%E3%82%A6%E3%83%B3%E3%83%BB%E3%83%A9%E3%83%81%E3%82%A7%E3%83%83%E3%83%88 (2009).

[79] A. Ajdari and J. Prost, *Mouvement induit par un potentiel périodique de basse symétrie: diélectrophorèse pulsée*, Comptes Rendus de l'Académie des sciences Paris Série II **315**, 1635 (1992);
M. O. Magnasco, *Forced thermal ratchets*, Physical Review Letters **71**, 1477 (1993).

[80] J. Rousselet, L. Salome, A. Ajdari, and J. Prost, *Directional motion of Brownian particles induced by a periodic asymmetric potential*, Nature **370**, 446 (1994);
L. P. Faucheux and A. Libchaber, *Selection of Brownian particles*, Journal of the Chemical Society, Faraday Transactions **91**, 3163 (1995).

[81] L. P. Faucheux, L. S. Bourdieu, P. D. Kaplan, and A. Libchaber, *Optical thermal ratchets*, Physical Review Letters **74**, 1504 (1995).

[82] A.E. Filippov, J. Klafter, and M. Urbakh, *Friction through dynamical formation and rupture of molecular bonds*, Physical Review Letters **92**, 135503 (2004).

[83] F. Family, H. G. E. Hentschel, and Y. Braiman, *Friction at the nanoscale*, Journal of Physical Chemistry B **104**, 3984 (2000).

[84] O. M. Braun and Y. S. Kivshar, *Nonlinear dynamics of the Frenkel–Kontorova model*, Physics Reports **306**, 1 (1998).

[85] M. H. Müser, in *Fundamentals of Friction and Wear on the Nanoscale*, edited by E. Gnecco and E. Meyer, Springer, 2007.

[86] H. D. Vollmer, *Two Particle Model for the Diffusion of Interacting Particles in Periodic Potentials*, Zeitschrift für Physik B **33**, 103 (1979).

[87] O. M. Braun, *Role of entropy barriers for diffusion in the periodic potential*, Physical Review E **63**, 011102 (2000).

[88] O. M. Braun, R. Ferrando, and G. E. Tommei, *Stimulated diffusion of an adsorbed dimer*, Physical Review E **68**, 051101 (2003).

[89] C. Fusco and A. Fasolino, *Microscopic mechanisms of thermal and driven diffusion of non rigid molecules on surfaces*, Thin Solid Films **428**, 34 (2003).

[90] S. Gonçalves, V. M. Kenkre, and A. R. Bishop, *Nonlinear friction of a damped dimer sliding on a periodic substrate*, Physical Review B **70**, 195415 (2004).

[91] S. Gonçalves, C. Fusco, A. R. Bishop, and V. M. Kenkre, *Bistability and hysteresis in the sliding friction of a dimer*, Physical Review B **72**, 195418 (2005).

[92] X. R. Qin, B. S. Swartzentruber, and M. G. Lagally, *Diffusional Kinetics of SiGe Dimers on Si(100) Using Atom-Tracking Scanning Tunneling Microscopy*, Physical Review B **85**, 3660 (2000).

[93] E. Heinsalu, M. Patriarca, and F. Marchesoni, *Dimer diffusion in a washboard potential*, Physical Review E **77**, 021129 (2008).

[94] A. Libál, C. Reichhardt, B. Jankó, and C. J. Olson Reichhardt, *Dynamics, Rectification, and Fractionation for Colloids on Flashing Substrates*, Physical Review Letters **96**, 188301 (2006).

[95] C. Lutz, M. Kollmann, and C. Bechinger, *Single-File Diffusion of Colloids in One-Dimensional Channels*, Physical Review Letters **93**, 026001 (2004).

[96] C. Lutz, M. Reichert, H. Stark, and C. Bechinger, *Surmounting barriers: The benefit of hydrodynamic interactions*, Europhysics Letters **74**, 719 (2006).

[97] F. Jülicher, A. Ajdari, and J. Prost, *Modeling molecular motors*, Reviews of Modern Physics **69**, 1269 (1997).

[98] A. Ajdari, *Force-free motion in an asymmetric environment: a simple model for structured objects*, Journal de Physique I France **4**, 1577 (1994).

[99] I. Derényi and T. Vicsek, *The kinesin walk: a dynamic model with elastically coupled heads*, Proceedings of the National Academy of Sciences USA **93**, 6775 (1996); *Realistic Models of Biological Motion*, Physica A **249** 397 (1998).

[100] Z. Csahók, F. Family, and T. Vicsek, *Transport of elastically coupled particles in an asymmetric periodic potential*, Physical Review E **55**, 5179 (1997).

[101] S. Klumpp, A. Mielke, and C. Wald, *Noise-induced transport of two coupled particles*, Physical Review E **63**, 031914 (2001).

[102] H. Y. Wang, and J. D. Bao, *The roles of ratchet in transport of two coupled particles*, Physica A **337**, 13 (2004);
Cooperation behavior in transport process of coupled Brownian motors, Physica A **357**, 373 (2005);
Transport coherence in coupled Brownian ratchet, Physica A **374**, 33 (2007).

[103] J. L. Mateos, *A random walker on a ratchet*, Physica A **351**, 79 (2005).

[104] S. E. Mangioni and H. S. Wio, *A random walker on a ratchet potential: effect of a non Gaussian noise*, European Journal of Physics B **61**, 67 (2008).

[105] E. M. Craig, M. J. Zuckermann, and H. Linke, *Mechanical coupling in flashing ratchets*, Physical Review E **73**, 051106 (2006).

[106] J. Menche and L. Schimansky-Geier, *Two particles with bistable coupling on a ratchet*, Physical Letters A **359**, 90 (2006).

[107] S. von Gehlen, M. Evstigneev, and P. Reimann, *Dynamics of a dimer in a symmetric potential: Ratchet effect generated by an internal degree of freedom*, Physical Review E **77**, 031136 (2008).

[108] K. Luo, T. Ala-Nissila, S.-C. Ying, and A. Bhattacharya, *Sequence Dependence of DNA Translocation through a Nanopore*, Physical Review Letters **100**, 058101 (2008).

[109] D. S. Fisher, *Sliding charge-density waves as a dynamic critical phenomenon*, Physical Review B **31**, 1396 (1985).

[110] L. L. Bonilla, *Nonequilibrium phase transition to a time-dependent probability density for a model of charge-density waves*, Physical Review B **35**, 3637 (1987).

[111] A. V. Ustinov, M. Cirillo, and B. A. Malomed, *Fluxon dynamics in one-dimensional Josephson-junction arrays*, Physical Review B **47**, 8357 (1993).

[112] H. S. J. van der Zant, T. P. Orlando, S. Watanabe, and S. H. Strogatz, *Kink Propagation in a Highly Discrete System: Observation of Phase Locking to Linear Waves*, Physical Reviw Letters **74**, 174 (1995).

[113] P. Reimann, R. Kawai, C. Van den Broeck, and P. Hänggi, *Coupled Brownian Motors: Anomalous Hysteresis and Zero-bias Negative Conductance*, Europhysics Letters **45**, 545 (1999).

[114] P. Zubko and J.-M. Triscone, *Applied physics: A leak of information*, Nature **460**, 45 (2009).

[115] X. R. Qin, B. S. Swartzentruber, and M. G. Lagally, *Diffusional Kinetics of SiGe Dimers on Si(100) Using Atom-Tracking Scanning Tunneling Microscopy*, Physical Review Letters **85**, 3660 (2000);
Z.-Y. Lu, F. Liu, C.-Z. Wang, X. R. Qin, B. S. Swartzentruber, M. G. Lagally, and K.-M. Ho, *Unique Dynamic Appearance of a Ge–Si Ad-dimer on Si(001)*, Physical Review Letters **85**, 5603 (2000).

[116] M. T. Downton, M. J. Zuckermann, E. M. Craig, M. Plischke, and H. Linke, *Single-polymer Brownian motor: A simulation study*, Physical Review E **73**, 011909 (2006).

[117] V. Becker and A. Engel, *Role of interactions in ferrofluid thermal ratchets*, Physical Review E **75**, 031118 (2007).

[118] U. Henningsen and M. Schliwa, *Reversal in the direction of movement of a molecular motor*, Nature **389**, 93 (1997);
S. Rice *et al.*, *A structural change in the kinesin motor protein that drives motility*, Nature **402**, 778 (1999).

[119] M. Porto, M. Urbakh, and J. Klafter, *Atomic Scale Engines: Cars and Wheels*, Physical Review Letters, **84**, 6058 (2000).

[120] S. Cilla, F. Falo, and L. M. Floría, *Mirror symmetry breaking through an internal degree of freedom leading to directional motion*, Physical Review E **63**, 031110 (2001).

[121] P. Reimann and M. Evstigneev, *Pulsating potential ratchet* , Europhysics Letters **78**, 50004 (2007).

[122] D. Dan, A. M. Jayannavar, and G. I. Menon, *A biologically inspired ratchet model of two coupled Brownian motors*, Physica A **318**, 40 (2003).

[123] A. Igarashi, S. Tsukamoto, and H. Goko, *Transport properties and efficiency of elastically coupled Brownian motors*, Physical Review E **64**, 051908 (2001);
A. Igarashi, H. Goko, and S. Tsukamoto, *One- and two-dimensional dynamics of elastically coupled Brownian motors*, Physica A **325**, 62 (2003);
H. Goko and A. Igarashi, *Elastically coupled two-dimensional Brownian motors*, Physical Review E **71**, 061108 (2005).

[124] L. Gammaitoni, P. Hänggi, P. Jung, and F. Marchesoni, *Stochastic resonance*, Reviews of Modern Physics **70**, 223 (1998).

[125] C. H. Doering and J. C. Gadoua, *Resonant activation over a fluctuating barrier*, Physical Review Letters **69**, 2318 (1992).

[126] R. D. Astumian, *Thermodynamics and kinetics of a Brownian motor*, Science **276**, 917 (1997).

[127] P. Reimann, *Current Reversal in a White Noise driven flashing Ratchet*, Physics Reports **290**, 149 (1997).

[128] C. Van den Broeck, I. Bena, P. Reimann, and J. Lehmann, *Coupled Brownian Motors on a Tilted Washboard*, Annalen der Physik (Leipzig) **9**, 713 (2000).

[129] S. Denisov, *Particle with internal dynamical asymmetry: chaotic self-propulsion and turning*, Physics Letters A **296**, 197 (2002).

[130] K. V. Kumar, S. Ramaswamy, and M. Rao, *Active elastic dimers: Self-propulsion and current reversal on a featureless track*, Physical Review E **77**, 020102 (2008).

[131] D. Dan, M. C. Mahato, and A. M. Jayannavar, *Motion in a rocked ratchet with spatially periodic friction*, Physica A **296**, 375 (2001);
Multiple current reversals in forced inhomogeneous ratchets, Physical Review E **63**, 056307 (2001).

[132] R. Krishnan, D. Dan, and A. M. Jayannavar, *Noise-induced currents and reliability of transport in frictional ratchets*, Physica A **354**, 171 (2005).

[133] W. L. Reenbohn, S. Saikia, R. Roy, and M. C. Mahato, *Motional dispersions and ratchet effect in inertial systems*, Pramana Journal of Physics, **71**, 297 (2008).

[134] S. Gonçalves, V. M. Kenkre, and A. R. Bishop, *Nonlinear friction of a damped dimer sliding on a periodic substrate*, Physical Review B **70**, 195415 (2004).

[135] S. Gonçalves, C. Fusco, A. R. Bishop, and V. M. Kenkre, *Bistability and hysteresis in the sliding friction of a dimer*, Physical Review B **72**, 195418 (2005).

[136] M. Tiwari, S. Gonçalves, and V. M. Kenkre, *Generalization of a nonlinear friction relation for a dimer sliding on a periodic substrate*, Eur. Phys. J. B **62**, 459 (2008).

[137] B. Nordén, Y. Zolotaryuk, P. L. Christiansen, and A. V. Zolotaryuk, *Ratchet due to broken friction symmetry*, Physical Review E **65**, 011110 (2001).

[138] A. Mogilner, M. Mangel, and R. J. Baskin, *Motion of molecular motor ratcheted by internal fluctuations and protein friction*, Physics Letters A **237**, 297 (1998).

[139] L. Marrucci, D. Paparo, and M. Kreuzer, *Fluctuating-friction molecular motors*, Journal of Physics: Condensed Matter **13** 10371 (2001).

[140] H. C. Fogedby, R. Metzler, and A. Svane, *Exact solution of a linear molecular motor model driven by two-step fluctuations and subject to protein friction*, Physical Review E **70**, 021905 (2004).